Broadband Electric Field Sensing and Its Application to Material Characterisation and Nuclear Quadrupole Resonance

Shrijit Mukherjee

Submitted for the degree of Doctor of Philosophy

University of Sussex

September 2011

Declaration

I hereby declare that this thesis has not been submitted, in this form or another, in this or any other university, for a degree.

Signature

Shrijit Mukherjee

UNIVERSITY OF SUSSEX

Broadband Electric Field Sensing and Its Application to Material Characterisation and Nuclear Quadrupole Resonance

Shrijit Mukherjee, Doctor of Philosophy

SUMMARY

The aim of this project is to address the challenges associated with extending the radio frequency capability of Electric Potential Sensors to greater than 10 MHz. This has culminated in a single broadband sensor, with a frequency range of 200 Hz to greater than 200 MHz.

The use of Electric Potential Sensors for the measurement of electric field with minimal perturbation has already been demonstrated at Sussex. These high impedance sensors have been successfully employed in measuring signals with frequencies in the range 1 mHz to 2 MHz. Many different versions of these sensors have been produced to cater for specific measurement requirements in a wide variety of experimental situations. From the point of view of this project, the relevant prior work is the acquisition of a 2 MHz electric field nuclear magnetic resonance signal, and the non-destructive testing of composite materials at audio frequency.

Two very distinct electric field measurement scenarios are described which illustrate the diverse capabilities of the broadband sensor. Firstly, an electric field readout system for nuclear quadrupole resonance is demonstrated for the first time, with a sodium chlorate sample at a frequency of 30 MHz. Nuclear quadrupole resonance is an important technique with applications in the detection of explosives and narcotics. Unlike nuclear magnetic resonance a large magnet is not required, opening up the possibility of portable equipment. The electric field readout system is shown to be simpler than the conventional magnetic readout and may therefore contribute to the development of portable devices. Secondly, a broadband, high spatial resolution microscope system for materials characterisation with four different imaging modes is described. This includes; the surface topography of a conducting sample; the dielectric constant variation in glass/epoxy composite; the conductivity variation in a carbon fibre composite; and the electrode pixels inside a solid state CMOS fingerprint sensor.

Acknowledgements

It is with great pleasure, satisfaction and some apprehension that I have come to this part. Firstly, I would like to convey my sincere gratitude to my supervisors, Prof. Robert Prance and Dr. Helen Prance, for their patient guidance, profound technical expertise, constant enthusiasm and unconditional support during the entire course of the project. Without them, this task would have been insurmountable. I am truly grateful to them and do hope to continue to receive their inspiring association in future.

I thank Martin Nock, our electronic technician, a master of all trades, jack of none, for his genuine help, advice, funny and intelligent conversations on numerous occasions. I also thank him for his close guidance during the early days of my project. Our mechanical technician Dave Smith, a man with flawless hands with machines, helped me on several occasions by producing professionally made mechanical aspects of my experiments. I thank him a lot for this. I must also thank Dr. Ahmet Aydin for his advice, help, support and friendly behaviour.

I should go back to the very start when I met Sam, who graduated last year, and Phil. Both of them have been great friends and supportive company during all this time and I must thank them for that. I must also thank Phil for spending time together during the latter part of my project and also for his general advice and friendship which I hope will remain in future. I would like to thank Tash, Philip/Maurice and Mohsen for their friendship and company for the odd pint on Friday afternoons. I also thank Jacob for his help, general advice and friendship.

I would like to remember my late grandparents who I am sure, would be very proud. I cannot thank enough my Jethu, my parents, my younger brother Manjeet, my uncle and aunt and their son, beloved Sanjeet, for their sincere love, sacrifices and constant support through the thick and thin. I dedicate this thesis to all of them. I also thank rest of my family.

Finally, I must thank my cousin, Protim, his wife and little Ankon, in Poole who have had me over many times and fed me sumptuously. I must thank Mamoud and Baba for being so considerate. I must thank Arnab, Souvik, Sunny, Anirban, Bimal, Monalisa, Nilanjan, Megan, Gaurav, Camay, Nish, Ravi, Shreya, Nick, Susannah, Siska, Lionel, Balaji, Karolina, TK, Akbar, Bilal, Nagachetan, Tanay and Aditya for good times and support.

TABLE OF CONTENTS

List of Publications

S Mukherjee, P Watson, R J Prance, "Microscopic resolution broadband dielectric spectroscopy," *Journal of Physics: Conference Series*, vol. 310, no. 1, p.012003, 2011.

S Mukherjee, P Watson, R J Prance, "Non-contact measurement of local conductivity variations in carbon fibre based composite materials," *Journal of Physics: Conference Series*, vol. 307, no. 1, p. 012034, 2011.

S Mukherjee, R J Prance, H Prance,“ Non-contact imaging of dielectric properties and Nuclear Quadruple Resonance signal acquisition”, *IOP Early career research in Electrostatics & Dielectric conference*, London, England,15th Dec 2009.

List of Tables

List of figures:

Chapter 1

Introduction and Background

1.1 Background of Electric Potential Sensor (EPS)

The Electric Potential Sensor (EPS) technology was invented at University of Sussex [**1**]. It can be used for the passive measurement of ambient electric field with minimal perturbation. This is achieved by the intrinsic properties of the measurement device which incorporates extremely high input impedance. This property helps these sensors to measure electric field with minimal loading effect. In simple terms, an EPS can be understood as an AC voltage amplifier with added features which enables it to pickup very weakly coupled AC signals, making it a highly sensitive device able to sense small variations in the signal resulting from changing electric field. An EPS couples to the source capacitively, drawing no real current at all, working entirely on displacement current. Likewise, they can also be termed as displacement current sensors. The circuitry of a typical sensor includes a DC bias current path to allow for stable operation. The capacitive coupling can be strong or weak, depending on the application, and together with the resistive DC path to ground, forms a pole, setting a lower value for the frequency response. As such, these sensors can be designed to operate down to very low AC signal frequencies, of the order of a few millihertz. The upper limit of the frequency response is largely a function of the device bandwidth, sensor gain and input source to sensor coupling. The input capacitance, another critical parameter for the sensor, determines the lowest coupling through which a sensor can reliably work. Naturally, a lower value of this is ideal and can be achieved by considering this at the design stage. This parameter is also important in setting the spatial resolution of the sensor, allowing it to measure electric field changes in highly localised areas aiding a heightened sensitivity of the measurement. A low input voltage noise is also important which allows these sensors to measure weak levels of the local

electric field. Clearly, specific circuit designs allow one to configure the sensor for the intended application and for the measurement task. Figure 1.1 sums this up pictorially with a simplified block diagram.

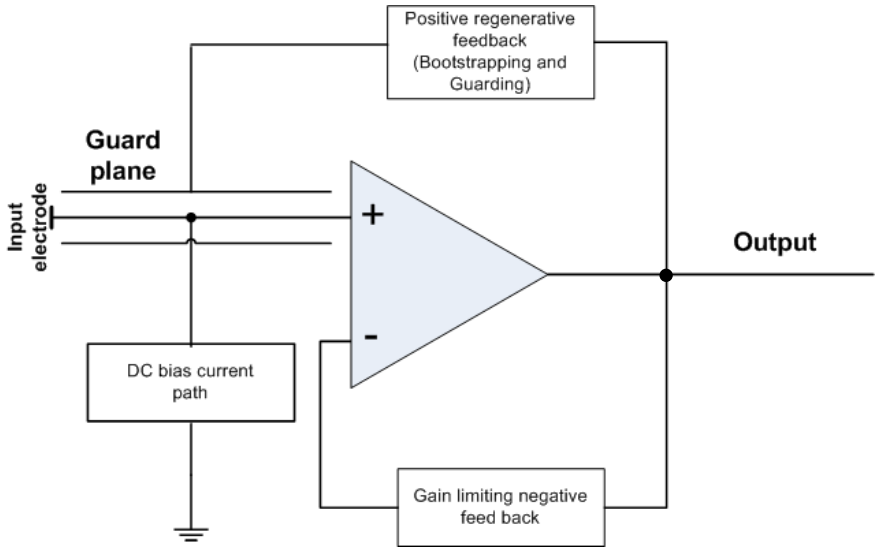

Figure 1.1: A simplified block diagram of an EPS

The EP sensor technology is widely applicable. The discussion to follow mainly attempts to summarise some of these applications and are supported by the relevant literature. This discussion is by no mean comprehensive, but nevertheless, gives a sense of appreciation of the extensive usefulness of the technology and subsequently narrows down to the areas that has been explored in this thesis.

Electrophysiology: The EPS have been used for contact and remote sensing of human body in electrically shielded as well as unshielded environments [**2**] [**3**] [**4**] [**5**], by measuring physiological signals generated due to the bio-electrical activity of different body parts such as heart, muscles, eyes and brain. Human body electrical activities are of interest for various reasons. The EPS provides a completely non-conventional, purely capacitive (no resistive contact) means to carry out these measurements. The ability to do so makes this attractive for alternative clinical practices and innovative medical devices. The ability to measure signals generated by muscles and brain activities makes it a potential candidate for human- computer/machine interfacing applications.

Security and safety: Since these sensors can detect changes in local electric field, an interesting application of detecting through wall movement, in which the signal is generated by the movement of a human body acting as a dielectric, causing disturbance in the local electric field, has been reported by Beardsmore-Rust et al [**6**].The advantage of this application is that the sensors can be installed behind the wall and hence can be operated in hidden mode. However, the limitation is that the wall must be non-conducting, in which case, the signal of interest will be shorted to ground.

Electrostatics: In electrostatics, the ability to estimate and image static charge on insulators is of interest, especially in the study of tribo-charging effects and also imaging human finger prints due to the charge left by a finger on an insulating material. The EPS has been used to do this with various spatial resolutions [**7**] [**8**] [**9**] in a non-contact measurement mode. This application requires the sensor to be sensitive at extremely low frequencies and with very low input capacitance. In practice, the EPS is used as a probe head of a scanning system which measures local electric potential at a range of spatial locations over a defined sample area at known steps in a raster scan manner, thereby collecting the desired data set. The low frequency response allows the set up to measure the static charge density due to the relative motion between the sensor and the fixed surface containing the static charge. This is important because the EPS does not have any DC response. The low input capacitance allows the use of a micron scale sense electrode to obtain high spatial resolution for the imaging of the charge distribution. This non-contact estimation of the surface charge on dielectric materials especially when left by human contact (tribo-charging) using the EPS is an entirely new method and is of interest in forensic applications. Because of the non-contact nature of the technique, the same sample can be subsequently subjected to the traditional methods allowing for Deoxyribonucleic Acid (DNA) analyses [**10**]. This particular application demonstrates the quasi DC measurement capability of the sensing technology.

Material characterisation: In addition to the above, the EP sensors have also been used for material testing and characterisation. A tuned sensor in the audio frequency range was used by Clippingdale et al. to measure dielectric

properties with high spatial resolution of 1 μm [**11**]. Application in finding buried defects in carbon composite materials using these sensors has been experimentally done by Gebriel et al [**12**] [**13**] and through theoretical simulations by Stiffell et al [**14**]. Gebriel et al also uses an array of sensors with spatial resolution of 1mm, although the sensors used were broadband in the audio frequency range [**15**]. Measurement of propagation delay of signals in saline using the EPS was also reported by Gebriel et al [**16**].

Circuit imaging: The EPS has been used to image signals in Very Large Scale Integration (VLSI) circuits. The high input impedance and AC operation capabilities of the sensor allows it to operate completely non-invasively without drawing any real current and hence maintaining the electrical integrity of the sample. This measurement can be performed with a range of spatial resolutions depending on the physical size and type of the sample circuit. A high resolution scan with a tuned audio frequency sensor at 100 Hz, was performed by Prance et al [**17**] whereas imaging of fast pulses up to 10 MHz in digital circuits was reported by Gebrial et al [**18**].

Magnetic resonance: Among other applications, Nuclear Magnetic Resonance (NMR) signal acquisition using electric field read out at 2 MHz was performed successfully [**19**] [**20**]. This is a completely new method of performing NMR where it replaced the traditional method of signal acquisition by detecting the magnetic component of the signal using an inductively coupled pickup coil, by a capacitively coupled sensor to detect the electric component. This has the advantage of reduced crosstalk between the electrode and the coil, when compared to the traditional approach.

In material characterisation using EPS, all previously reported work suggests either, high spatial resolution with a tuned, single frequency sensor, or a broadband, audio to low radio frequency sensor with relatively coarse spatial resolutions. In this thesis, however, a single, broadband sensor, in the region of 10 KHz to 100 MHz, has been discussed which also demonstrates relatively much higher spatial resolution, of the order of 5 μm. This sensor has been employed in the measurement of local dielectric properties of a non-conductive composite material over a broad range of frequencies featuring high spatial

resolution [**21**]. The technique was extended to measure variation of local electrical conductivity of a lossy, poorly conductive, carbon composite based material over a broad frequency range and with high spatial resolution [**22**].

1.2 Background of Nuclear Quadrupole Resonance (NQR)

The theory of Nuclear Qadrupole Resonance (NQR) has been discussed in detail elsewhere in the thesis. NQR is a radio frequency (RF) technique, like NMR which employs an external magnet to establish a static magnetic field to align the magnetic moments in the participating ensemble of nuclei. Under this influence a burst of RF energy is applied which instantaneously alters the direction of the vector sum of the bulk magnetic moments of the nuclei, otherwise known as the magnetization vector. As soon as the burst is over, relaxation process takes place, which results in a precessional motion of the bulk magnetization about the direction set by the external field, constituting the free induction decay (FID) signal. This phenomenon was initially reported by Purcell et al [**23**] and Bloch et al [**24**].

An external magnetic field is not a requirement for NQR experiments which is why it is also sometimes known as zero-field NMR. This makes the technique an attractive one in which the portability is greatly enhanced. It is discussed elsewhere that NQR occurs for nuclei with spin quantum number, $I>1/2$, or quadrupolar nuclei which contain a non-zero Electric Field Gradient (EFG). Thus, NQR can be used to detect quadrupolar nuclei, found in a large number of elements in the periodic table including the likes of ^{14}N, prevalent in many explosives and narcotics. This makes NQR a favoured technique for the detection of such contraband material remotely, out in the field [**25**] [**26**]. Various pulse sequences have been studied and reported to enhance the signal to noise ratio and to reduce the false alarm rate in applications detecting narcotics and explosives such as Heroin and Trinitrotoluene (TNT) [**27**] [**28**] [**29**] [**30**]. Among other methods to improve technique is the use of different polarizations method as reported by Rudakov et al [**31**].

Clearly, NQR is an important spectroscopic tool for differentiating chemical compounds and therefore an important subject to study. In all mentioned sources, the signal acquisition technique uses an RF coil of certain geometry to detect the signal by measuring the magnetic component of the electromagnetic (EM) relaxation signal. Little work has been done to measure the associated electric field (Maxwell's equations), except Prance et al [**19**] [**20**] which does so in the context of NMR and Gregorovic et al who use a capacitor, as opposed to a coil, to excite the sample in a pulsed NQR experiment [**32**]. Fisher et al describes a computer controlled pulsed NQR spectrometer [**33**]. As such, the subject of NQR is rather broad and there are many areas to look at including RF coil design, pulse sequence, signal processing etc., from an engineering point of view, to improve the technique and optimize it for the chemical under consideration and the surrounding environment.

In this thesis, a high impedance and high frequency version of EPS has been developed and employed to establish and measure the electric field component of the NQR signal for a sodium chlorate sample at 30 MHz in both continuous wave and pulsed experiments. It has been proposed by the early work of Prance and Aydin et al [**19**] [**20**] that with the electric field measurement, the cross coupling between the coil and the electrode of the high impedance EPS is much lower when compared to the conventional method.

1.3 Background of scanning microscopy and material characterisation techniques

There are different types of materials- metallic and non metallic, natural and synthesised etc. Unlike structural materials, functional materials respond to environmental changes such as pressure, temperature, electric and magnetic fields, optical wavelengths, pH values etc and use functions of their own to achieve intelligent actions [**34**]. Knowledge of the electrical properties, together with other important physical and chemical ones, of these new advanced composite functional materials is important, especially when they are used in

environments where they are likely to interact with electromagnetic signals of various frequencies and strengths.

The measurement of dielectric properties of material is of interest for many reasons. The nature of propagation of electromagnetic waves is greatly affected by its medium. Conductivity and permeability can be linked to stress and strain of materials helping to assess integrity. The data can provide microstructure of the material and provide precursor information on damage. Numerous techniques have been reported that characterise material for their electrical properties, each offering benefits and limitations.

An admittance method using two or three terminal admittance cell is used for both solid and liquid dielectrics. An admittance cell is an arrangement which uses two metal plate electrodes to hold the specimen in the middle and with end terminals to apply electric potential. The capacitance is measured with and without the specimen in the cell and the ratio gives the complex permittivity. The cell dimension scales down with increasing frequency and therefore this technique is favoured over frequencies from DC to 1 GHz. At higher frequency the three terminal cell is difficult to use and therefore two terminal cells are used, which are less accurate [**35**].

The resonance admittance cells or Hartshorn and Ward (H&W) technique was used in the 1930s to measure low loss and medium loss specimens in the range of 100 KHz to 100 MHz. Although sensitive impedance analysers in 1970s were later found to be more convenient and accurate for medium loss specimens. An admittance cell is resonated with an inductance coil with and without the specimen at the same frequency and the change in the Q-factor is used to compute the complex permittivity. This method can be repeated at different frequencies by using different inductance coils [**35**].

The Split-Post Dielectric Resonators (SPDR) developed by Krupka and his collaborators [**36**] is a convenient technique for measuring low or medium loss laminar dielectric specimens, such as substrates or thin films, in the frequency range 1-36 GHz. It uses a fixed geometry resonant measurement cell. A SPDR uses two identical dielectric resonators with a gap in the middle in which the specimen is placed. Once set up properly, only three parameters, thickness,

change in the resonant frequency and change in the Q-factor are required to be measured to calculate the complex permittivity. The disadvantage of this technique is that each SPDR can only work at one single frequency. However, it may be cost-effective to measure the same specimen in different SPDRs operating at different frequencies.

Dielectric Resonators (DR) are widely used in telecommunication applications as high-Q components for narrow band filters. Recent use of DRs are reported in literature [**37**] which uses a $TE_{01\delta}$ mode DR for the measurement of dielectric permittivity and loss tangent of various polymer based materials.

Time Domain Reflectometry (TDR) requires a small specimen and is a broadband cost effective technique. It is mostly used for the purposes of scientific study. As the name suggests, TDR uses a step or pulse fed down a matched transmission line terminated by the specimen and measures the reflected pulse using a sampling oscilloscope, which is then analysed for its magnitude, duration and shape to determine the nature of the impedance.

Needless to say there are other techniques, in addition to the ones mentioned here. Each method has their merits and limitations. All these techniques require the sample specimen to be placed in some kind of measurement cell. While some of these techniques can allow the dielectric to be measured over a broad range of frequencies and temperatures, they do not give much information about the material structure.

Non destructive techniques exist for fault/failure detection in various samples. Acoustography [**38**] , eddy current and SQUID based method [**39**] and electric potential change due to resistance change techniques [**40**] are used on composite materials. Eddy current techniques are more suited to metallic material and are popular in that category. Acoustic methods have been found to be better than ultrasonic methods for carbon fibre reinforced polymers (CFRP).

High resolution surface scans are possible by using the Nobel Prize winning invention, the Scanning Tunnelling Microscopy (STM) [**41**] and subsequent development of Atomic Force Microscopy (AFM) [**42**], both fall under the category of Scanning Probe Microscopy (SPM) techniques. STM works on the

principle of quantum tunnelling where electrons flow through the vacuum when a bias voltage is applied to a sharp tip, conducting electrode, positioned very close to the sample surface under examination. A crucial component of an STM is the electrode tip which sets the resolution of the scan. It is imperative to have a sharp single tip to avoid image artefacts. Atomic scale diameters, high aspect ratio, elasticity and the good electrical conductivity of Carbon Nanotubes (CNT) make them good candidates for high resolution, robust and reliable scanning probes for STM [**43**].

By comparison, AFM uses a cantilever, usually made of silicon nitride but more recently CNT for its exceptional physical properties, which is held very close to the sample surface where it can interact with the sample at atomic scales. The deflection or bending of the cantilever is proportional to the weak atomic forces such as Van der Waals force, chemical bodings and electrostatic force etc, occurring due to the atomic level interaction between the nanometer scale diameter cantilever tip and the material surface. The bending of the cantilever is measured generally by an optical mechanism in which reflection of the laser focussed on the opposite side of the cantilever tip is picked up by a photodiode. This system is extremely sensitive and accurate and is able to measure forces of the order of 10^{-12} N [**44**].

Apart from STM and AFM, there exist other SPM such as scanning noise, thermovoltage and scanning capacitance methods, each based on utilising different physical property for the feedback mechanism to maintain a fixed parameter scan at nanometre resolution [**45**] [**46**] [**47**] [**48**]. Despite giving excellent lateral and depth resolutions using these advanced SPM techniques, they can only be employed in case of conducting samples and are inconvenient to use with relatively large sample sizes exceeding a few tens of square millimetres, speed of operation being the biggest deterrent.

The EPS based technique [**21**] [**22**] described in this thesis provide very good results for composite dielectric and resistive samples which provides flexibility in both spatial resolution and the frequency of operation. A previously reported macro array of EPS has already demonstrated a reduction of time in scanning based techniques. High density micro arrays of EPS, soon to be available, may

potentially be used for these measurements which will significantly increase the scanning speed and also increase the spatial resolution, possibly to the sub-micron scales, all in a non-contact and non-destructive manner.

1.4 Thesis organisation

In this thesis, there are three major sections. Development of a high frequency and subsequently a broadband version of the EPS were carried out in the first phase of the project. Secondly, the theory of Nuclear Quadrupole Resonance (NQR) has been studied and the necessary electronics and mechanical aspects of a continuous wave and a pulsed experiment were undertaken. This was done to incorporate the sensor system in the experiment to detect the electric field component of the signal which exists with the magnetic counterpart, demonstrated elsewhere previously with these sensors [**49**]. Results are given for the NQR of Cl^{35} in $NaClO_3$ at around 30 MHz. Finally, a broadband sensor developed earlier on in the project was integrated with an XY scanner head to raster scan a number of fundamentally different samples at microscopic resolutions and to characterise them over a broad frequency range. This is to demonstrate simultaneously the broadband nature of the sensor together with high spatial resolution capabilities, something not done previously.

Chapter 2 discusses the details of the EPS and development of a broadband version of the sensor. A single sensor was developed which is operable from 10 KHz up to 200 MHz. The input capacitance of these sensors is also low enough to use them for not only over a broad range of frequencies but also with relatively high spatial resolution. This sensor is an advancement in the category of sensors previously developed with specific applications, in which they were either broadband or had micrometer scale resolution.

Chapter 3 discusses the theory of Nuclear Quadrupole Resonance (NQR) and a continuous wave NQR experiment using a high frequency version of EPS to acquire the NQR absorption signal for Sodium Chloride at 30 MHz. This is a step forward from the previous work done by A.Aydin in which he demonstrated

NMR signal acquisition using EPS at 2 MHz. Chapter 4 discusses a more commonly used but more complex pulsed NQR experiment to demonstrate electric field NQR signal acquisition.

Chapter 5 discusses a scanning system based on the broadband EPS and its first application in imaging the surface topography of a sample with interconnected conducting traces on a dielectric substrate. This comprises the details of the measurement system, method of sample excitation and results showing the efficacy of the sensor when used to image such a sample over a broad range of frequencies from 10 KHz up to 20 MHz with spatial resolution of 100 µm, using a single EPS.

This system was extended for measuring local dielectric properties of a standard FR4 PCB over a frequency range of 10 KHz to 11 MHz at 100 µm resolutions in chapter 6. The variation of local electrical conductivity in a carbon composite material over the same range and spatial resolution is also discussed in the same chapter.

Chapter 7 discusses the extended capability of the same broadband sensor in which it is used to image the interior microstructure array of metal electrode pixels of a solid state CMOS finger print IC at 5 µm resolution. The imaged pixel structure has been shown to have a good degree of agreement with the actual physical geometry provided in the manufacturer’s datasheet.

Chapter 2

Development of the broadband Electric Field Sensor

2.1 Introduction

The ability to measure alternating electric fields offers many useful applications. Electric Potential Sensor (EPS) technology was developed at Sussex [**1**] with an aim of passively measuring the ambient electric field. These sensors were designed to have extremely high input impedance that can be considered to be infinite for practical purposes. With such high input impedance, these sensors do not draw any real current from an active source and therefore operate solely on displacement current. The source in this case can be anything that can produce an alternating electric field such as a human body, CMOS chip in operation, precessing magnetic field or dielectric or resistive materials excited by an external signal generator. These sensors can therefore be used in wide range of applications where there is a possibility of measurement of the local electric field. The sensors have been characterised for input resistance of the order of 10^{17} Ω, input capacitance of the order of 10^{-16} F and an operational bandwidth of 1 mHz to > tens of MHz. With the advances in solid state technology and experience over time, these figures constantly improve. Specific designs are made for the application in question.

2.2 An ideal Electric Potential Sensor (EPS)

An ideal EPS should have the following characteristics:

-Infinite bandwidth

-Infinite dynamic range

-Infinite input resistance

-Zero input bias current

-Zero input capacitance

-Zero current and voltage noise

Clearly with the above specifications an ideal sensor will be able to measure electric field from pure dc to any frequency and of any amplitude without hitting the noise floor or saturation. Needless to say such specifications are practically impossible due to the limitations of the physical world. However, it is possible to get very close to these ideals with appropriate choice of components, careful design of the circuitry, attention to the printed circuit board design and the construction of the sensors. In particular, input impedance of hundreds of Terraohms, input capacitance of the tens of attofarads and bandwidth of 1 mHz to more than 100 MHz are within the realms of achievable parameters for these sensors at present.

2.3 Positive feedback techniques

In designing high input impedance circuits such as EPS, a number of positive feedback networks are generally employed. These techniques offer different benefits that can improve the performance of these circuits. It is important to note that these techniques must be used with caution and with sufficient control over the feedback parameters. If the loop gain exceeds unity it can lead to sustained oscillations which will saturate the sensors, compromising their performance. Appendix A discusses the effect of positive feedback on the sensor transfer function in more detail and establishes the fact if feedback gain becomes the exact reciprocal of the forward gain and if there is no phase shift, the output becomes independent of the input signal which is the case of self sustained oscillation [**50**]. This section discusses these standard techniques used in the design of the broadband sensor.

2.3.1 Bootstrapping

In the design of high input impedance circuits, often positive feedback is used to increase the effective input resistance of the amplifier. Controlled positive feedback, where some or all voltage, depending on the gain of the circuit, is fed back to the non-inverting input of the op-amp can significantly increase the input resistance of the circuit. This technique is called bootstrapping [**51**] [**52**].

Figure 2.1 (a) shows a non-inverting amplifier circuit. The capacitor C1 is the coupling capacitor which the EPS uses to couple to the source whatever the type. The resistor R2 provides the dc bias path that allows the required input bias current to flow. In this configuration the input resistance of the circuit is set by the actual value of R2. It is possible to obtain very high value discrete resistors of the order of $>10^{13}\,\Omega$. But this resistor is in parallel with the common mode input resistance of the op-amp which can effectively lower the value if the latter is less. So, if the input resistance of the op-amp is $10^{12}\,\Omega$, this value will be dominated by the lower value in parallel ($10^{13}\,\Omega \,||10^{12}\,\Omega \approx 10^{12}\,\Omega$)

Figure2.1 (b) shows R2 is connected to the output through the capacitor C2. If the voltage V_{R2} is made very close to V_{in} such that V_{R2} - $V_{in} \approx 0$, almost no current will flow through R2, making its effective value higher by several orders of magnitude. It is important to note that the two voltages have to be in phase in order to make the process effective. With an increased input resistance we can improve the low frequency performance of the amplifier. The lower corner frequency of the frequency response is dictated by the input resistance and the coupling capacitance ($f_C = \frac{1}{2\pi R_2 C_1}$). With an increased value of R2 the corner frequency can be pushed to a lower value, increasing the bandwidth at the lower end of the frequency response.

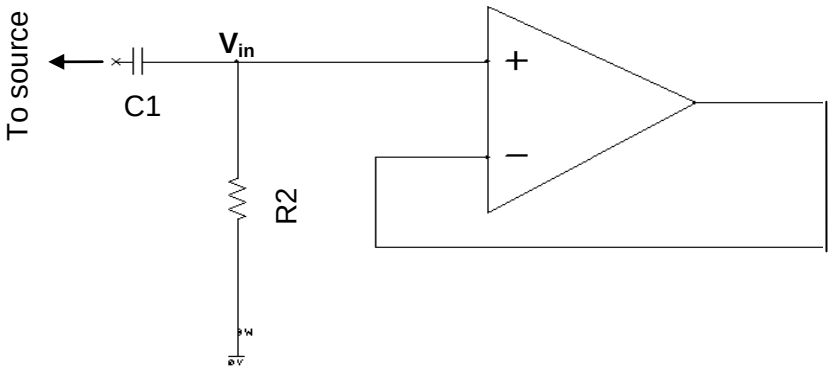

(a)

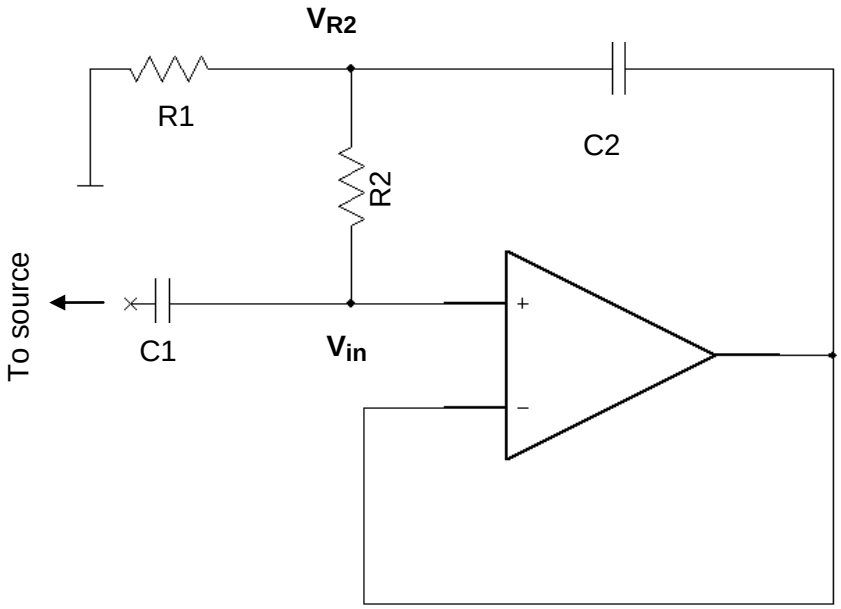

(b)

Figure 2.1: High impedance circuit (a) without bootstrapping (b) With bootstrapping.

2.3.2 Guarding

In addition to the common mode input resistance, there exists a common mode input capacitance in a standard op-amp. This input capacitance can limit the performance of a capacitively coupled system such as a standard EPS. As mentioned previously, an EPS couples with the source capacitively and this capacitance can be very small depending on the application. This value is higher in contact mode than it is in remote mode. Figure 2.2 shows a typical situation showing the capacitive voltage divider scenario that arises with EPS. C_c is the coupling capacitance and C_{in} is the input capacitance of the non-inverting input of the op-amp. The voltage across C_{in} is the voltage coupled to the EPS. It can be easily seen that this forms a standard voltage divider formula the input voltage V_{in} can be expressed as follows:

$$V_{in} = \frac{X_{in}}{X_{in} + X_c} V_s \qquad (2.1)$$

Where

$$X_c = \frac{1}{2\pi f C_c} \qquad (2.2a) \qquad \text{and} \qquad X_{in} = \frac{1}{2\pi f C_{in}} \qquad (2.2b)$$

Substituting these values in the previous equations, we get the following

$$V_{in} = \frac{C_c}{C_{in} + C_c} V_s \qquad (2.3)$$

It is clear from the equation 2.3 that for a given coupling condition, if C_{in} can be reduced then more voltage can be coupled to the EPS resulting in a higher

output. If the value of C_{in} is higher, it will significantly attenuate the voltage which will result in a very poor signal-to-noise ratio. Thus, it is necessary to be able to reduce this value where possible.

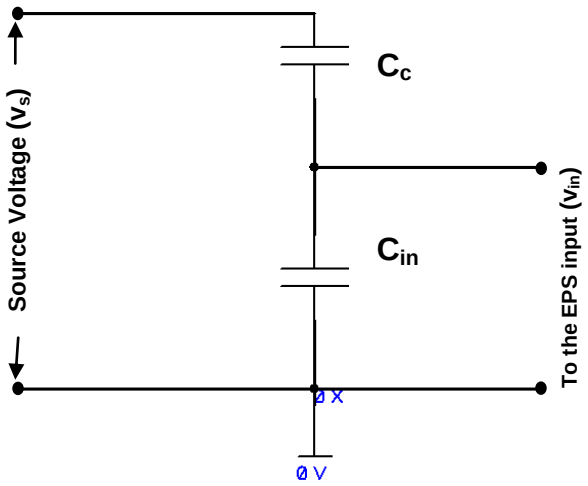

Figure 2.2: A capacitive voltage divider at the EPS input.

Guarding is a useful technique employed in high impedance circuits like EPS, which can reduce the input capacitance and stray capacitance, improves the common mode rejection and eliminate the leakage currents [**53**]. Generally, a conducting ring is put around the non-inverting input of the op-amp which is connected to a low impedance point on the circuit such as its output or the tap of the gain divider, to maintain the same potential or nearly same potential as the non-inverting input itself, eliminating any leakage current between the input and the ground. Figure 2.3 shows pictorially, different ways of putting the guard ring around the high impedance input. Clearly, different configurations feed different amounts of voltage and are useful in specific situations. Figure 2.3 (a) and (b) are essentially the same except, they feed less and more voltage back to the conducting ring, respectively. Figure 2.3 (c), an example of driven

guarding, incorporates an op-amp driven network but essentially all three use a low impedance feedback path to provide the guard voltage.

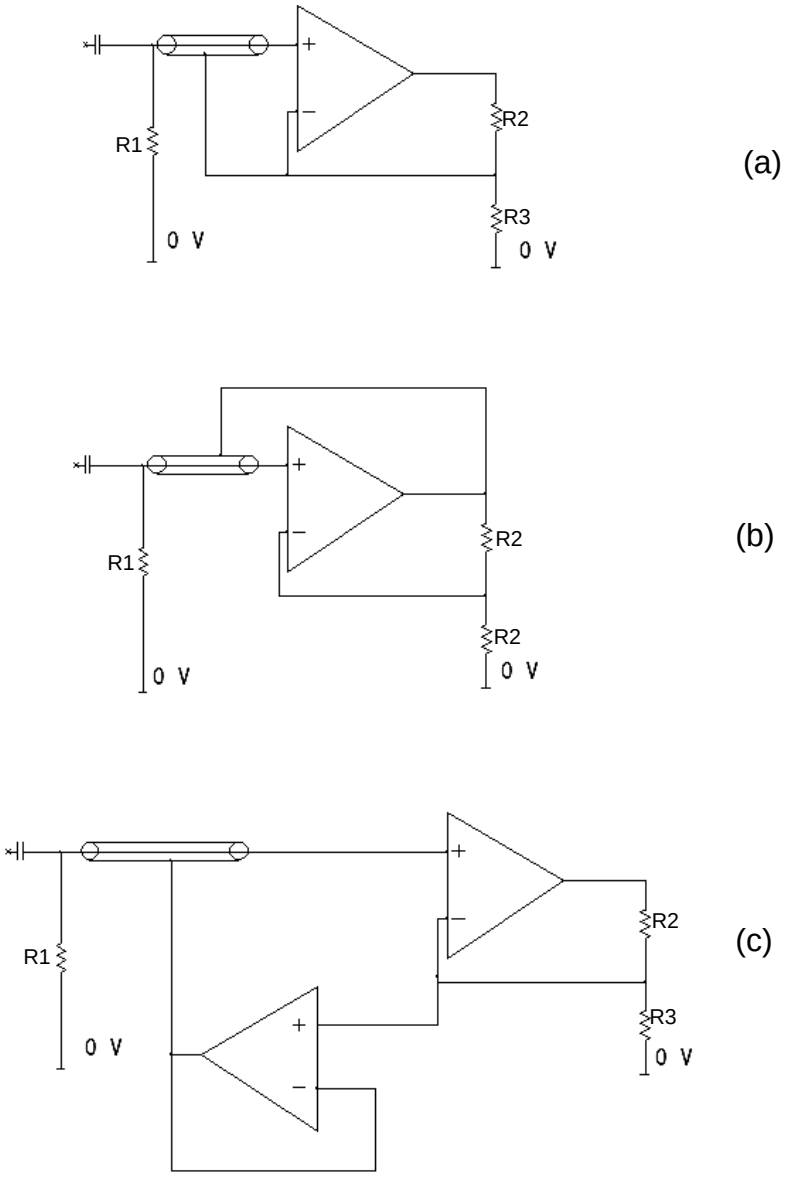

Figure 2.3: Different guarding configurations (a) guard ring connected to the gain divider tap (b) guard ring connected to the output of a gain x2 configuration (c) driven guard.

2.4 The broadband EPS

As a first step towards solving the problem of measuring ac signals of more than 10 MHz, it is required to have an EPS with a bandwidth that includes the measurement frequency. In order to build such an EPS, it is required to have an electrometer grade transistor which should have a very high value of intrinsic input resistance and a bandwidth that includes the frequency region where the measurement is intended to be performed.

Field Effect Transistors (FETs) are the devices of choice for high input impedance applications. Operational amplifiers with FET input stages are commercially available offering a number of advantages and prove suitable for such designs. These include high common mode resistance, low input capacitance, low voltage noise and high gain bandwidth product.

It was found that OPA656 is one such op-amp with a FET input stage, manufactured by Texas Instrument that has a unity gain bandwidth of 500 MHz and input common mode resistance and capacitance of $10^{12}\Omega$ and 2.8 pF respectively. This op-amp is unity gain stable and has a low input voltage noise of 7 nV/$\sqrt{\text{Hz}}$. It also takes a very low input bias current of 2 pA [**54**]. Such specifications suggest a good electrometer grade front end.

The design was initiated by simulating the circuit in the Electronics Workbench (EWB) which is a SPICE based circuit simulator. EWB provides a large library of electronic device parts with changeable parameters and allows changing the external component values [**55**]. Although this is a good starting point to give a fair idea of how the circuit will behave approximately, it does not guarantee exactly the same performance as the actual circuit which is constructed on a printed circuit board (PCB). It has been seen that these simulations give a good indication to certain parameters of the design that include the dc offset, gain and the effect of the coupling capacitance on the gain. However, it does not account for noise performance, effects of PCB stray elements, power supply rejection etc which result in less accurate indication of parameters such as usable bandwidth and phase response and the limitation in performance caused by electromagnetic interference. The actual practices involved in PCB design

are described later in this section. This, nevertheless, is a useful step in the design procedure with some reservations and therefore has been incorporated in the initial phases of design.

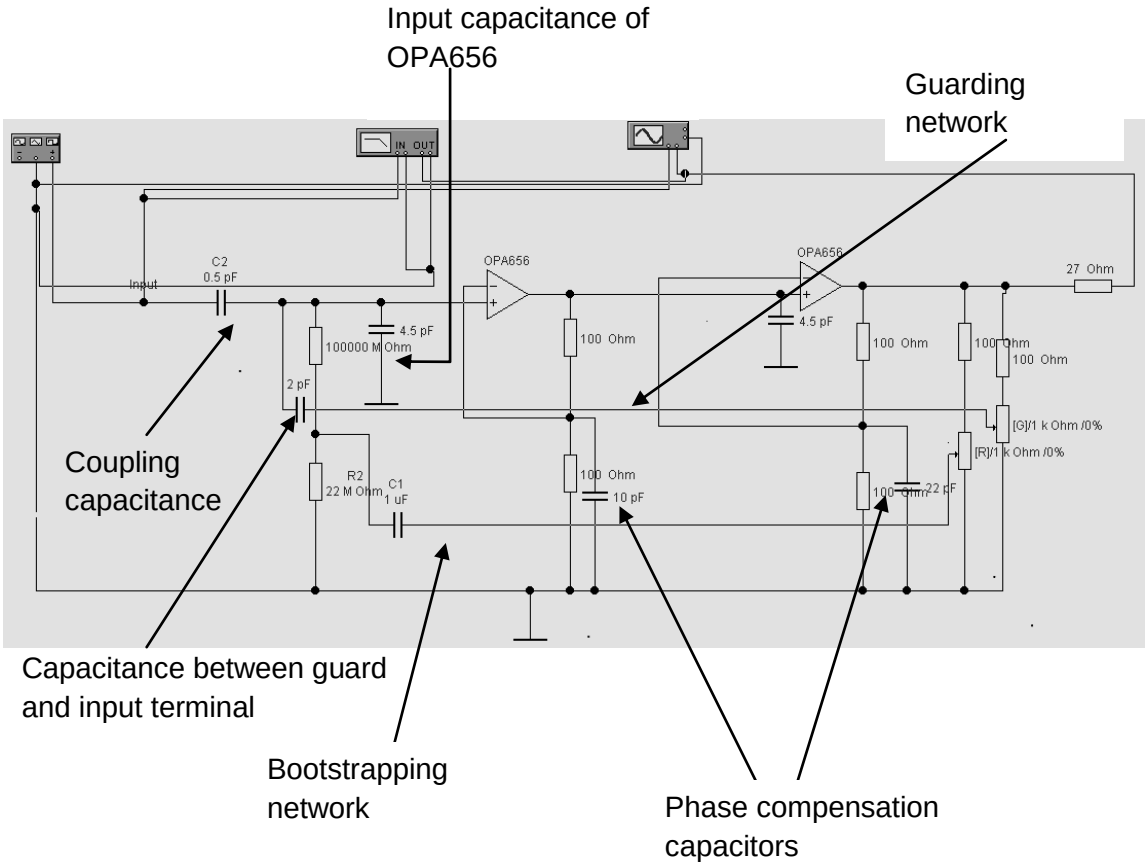

Figure 2.4: EPS circuit diagram showing various controls.

Figure 2.4 shows a circuit design that was employed in one of the first versions of the sensor development. Various important sections, relevant to the present discussion are shown with arrows. A coupling capacitance of 500 fF has been used for weak coupling to the source. This circuit uses bootstrapping and guarding networks and also compensation capacitors. These sections have different effects in the overall circuit behaviour and the following discussion will show how these individual networks influence the sensor performance independent of each other. Effects of bootstrapping and guarding are discussed in the following sections, where each of these parameters has been varied with the others being completely removed. The effect of adding compensation capacitance has been discussed for the same amount of applied guarding

voltage. Obviously, in practice the overall performance is determined by the combined effects of these network parameters which result in an overall improvement in bandwidth and therefore are factors for optimization.

The circuit used for simulating the EPS in figure 2.4 is representative of the general circuitry being used for the category of sensors with high frequency operation. It is therefore important to explain the schematic.

The OPA 656 datasheet gives a unity gain bandwidth of 500 MHz and a gain bandwidth product of 230 MHz. This falls in the category of fast op-amps where the conventional gain bandwidth product does not predict the closed loop bandwidth for a given gain for low gain configurations. However, for high gain configuration such as x10 or more, this is no longer the case. According to the datasheet, this happens because the phase margin is less than 90^{o} for lower gain. The OPA 656 is designed to give maximally flat frequency response of 200 MHz for a gain of +2 [**54**] and this gave us a good starting point to design a sensor to have at least 200 MHz. It is to be noted that this bandwidth is for small signals so if the sensor outputs more than 200 mV, the bandwidth will be dictated by large signal bandwidth which is generally much lower than the small signal bandwidth.

In order to design an ac coupled sensor, it is important to add sufficient gain to the system to detect small signals, especially when the sensor to source coupling is small. In order to do this and still maintain a good broadband performance, the second stage of the same op-amp has been added, making the total gain +4. Obviously, the choice of resistors is important because it directly affects the noise performance of the sensor. The higher the value of the resistor, the higher is the noise voltage and therefore the values are chosen so that the parallel combination of the gain setting resistor is approximately 200Ω or less.

As discussed later, bootstrapping is included in the circuit to improve the low frequency performance. The bootstrapping signal is ac coupled by a high value capacitor C1 of 1 µF to the bottom of the 100 GΩ resistor which is connected to the non inverting input the op-amp. The resistor R2, between the 100 GΩ and ground, has a much lower value. This is kept in order to provide a discharge

path for the capacitor and together with C1 forms a fairly long time constant. In absence of a discharge path, the voltage across C1 will never change and the sensor will eventually saturate. The value of R2 is somewhat flexible and sometimes can be replaced by PCB leakage.

The 2 pF capacitor is there to simulate the stray capacitance between the guard ring and the non inverting input. The compensation capacitors are placed in parallel with the forward gain setting resistor as shown. The 27 Ω resistor is placed at the output of the sensor in order to isolate the output of the sensor and external capacitive load. Without the isolation resistor the external capacitance associated with the load can form a pole together with the output resistance of the sensor which can seriously degrade the performance. The value of isolation resistor is somewhat flexible and usually between 10-100 Ω as recommend by the datasheet.

2.4.1 Effect of Bootstrapping only

In order to show the importance of certain networks in the circuit of the EPS, independent control has been incorporated and their direct effects on the circuit performance discussed**.** Figure 2.5 shows the effect of bootstrapping on the frequency response. Bootstrapping voltage is applied through a resistor divider network from the output to the bottom of the high ohmic bias resistor connected to the non-inverting input, as illustrated in figure 2.4. The potentiometer provides control for applying different amounts of bootstrapping voltages. Figure 2.5 (a) shows the lower end of the gain and phase response of the EPS when no bootstrapping voltage has been applied. The effective input resistance to the ground and the coupling capacitance of 500 fF forms the -3dB corner frequency of the lower end ($f_{-3dB} = \frac{1}{2\pi R_{in} C_c}$). For a C_c= 500fF and lower cut-off frequency f_{-3dB}= 22 Hz, the effective input resistance R_{in} is found to be 14.5 GΩ. After applying the bootstrapping voltage, as shown in figure 2.5(b), the corner

frequency has been pushed to 0.315 Hz, making the effective value of input resistance 1 TΩ, which is significantly larger.

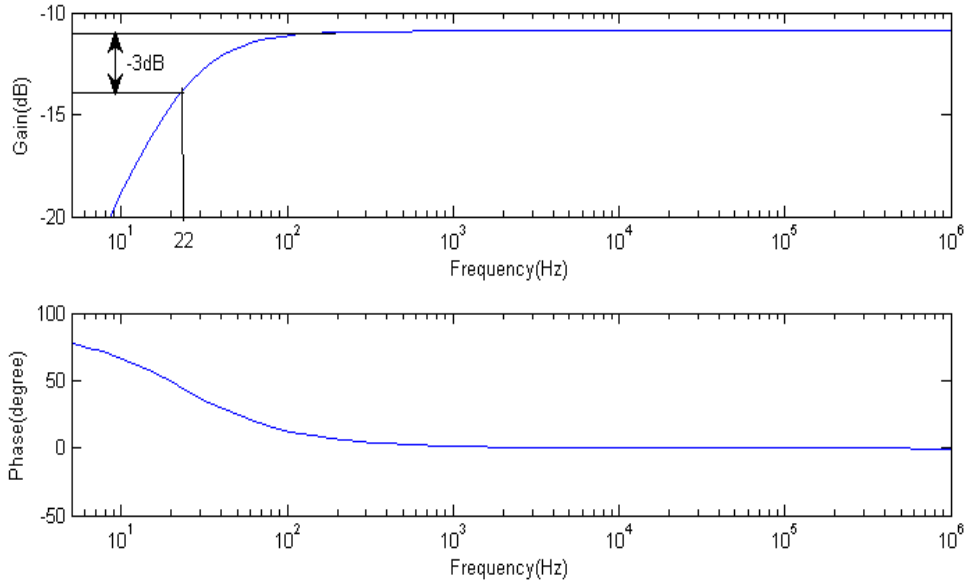

(a)

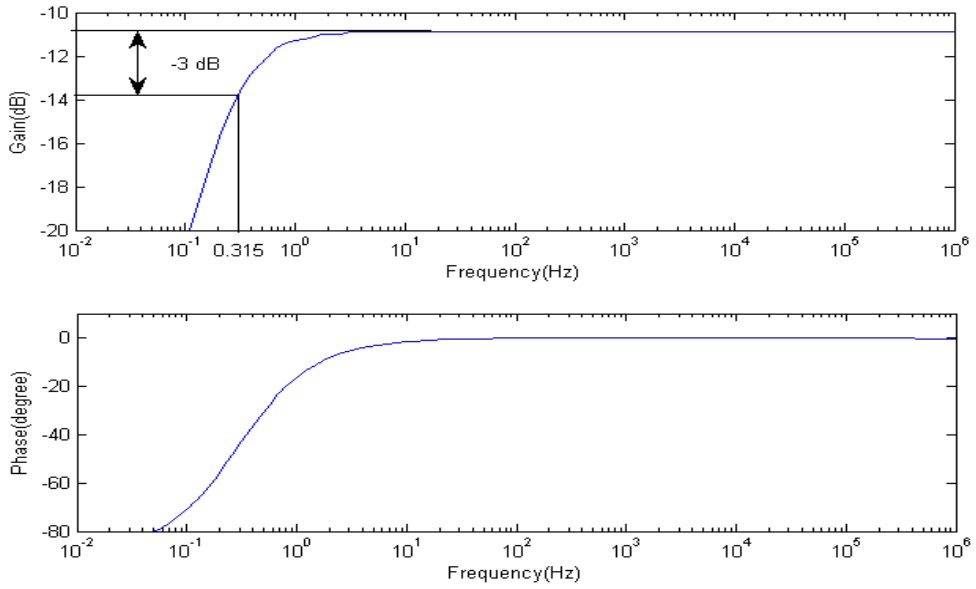

(b)

Figure 2.5: Effect of bootstrapping on frequency response produced by the simulation (a) No bootstrapping (b) with bootstrapping voltage applied.

2.4.2 Effect of Guarding only

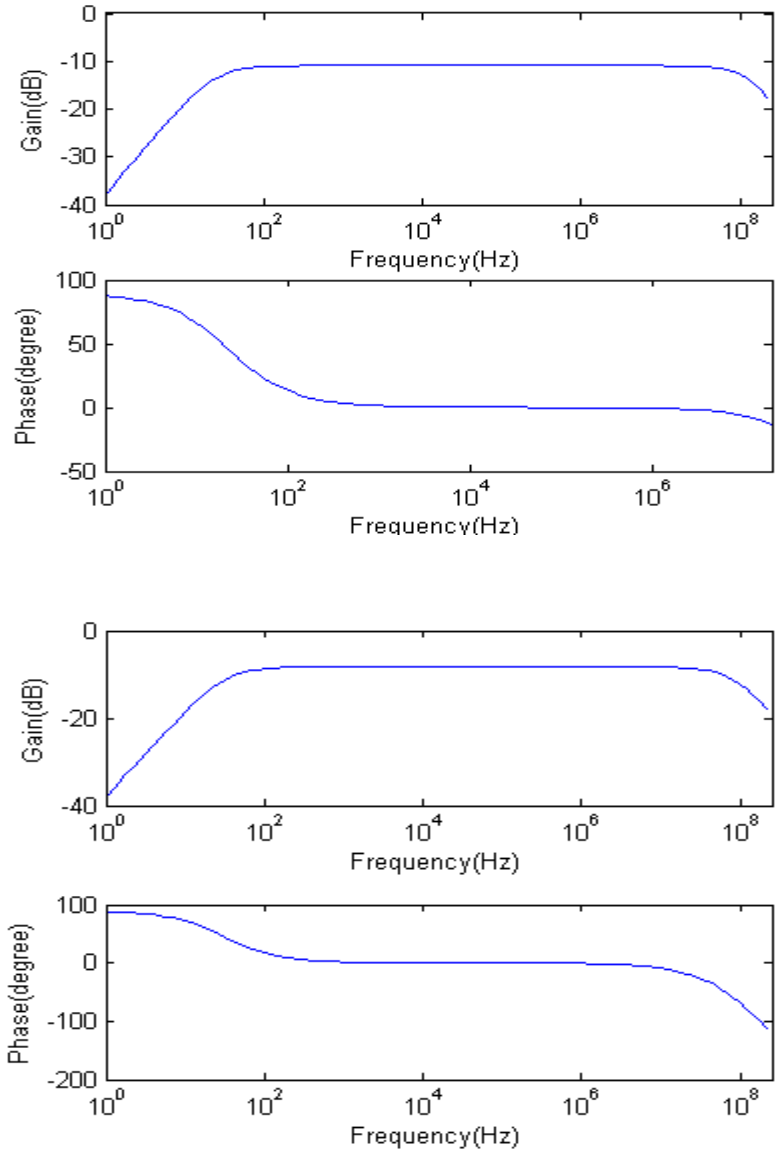

(a)

(b)

Figure 2.6: Effect of different amount of guarding on the frequency and phase response of EPS (a) 0 % (b) 25%.

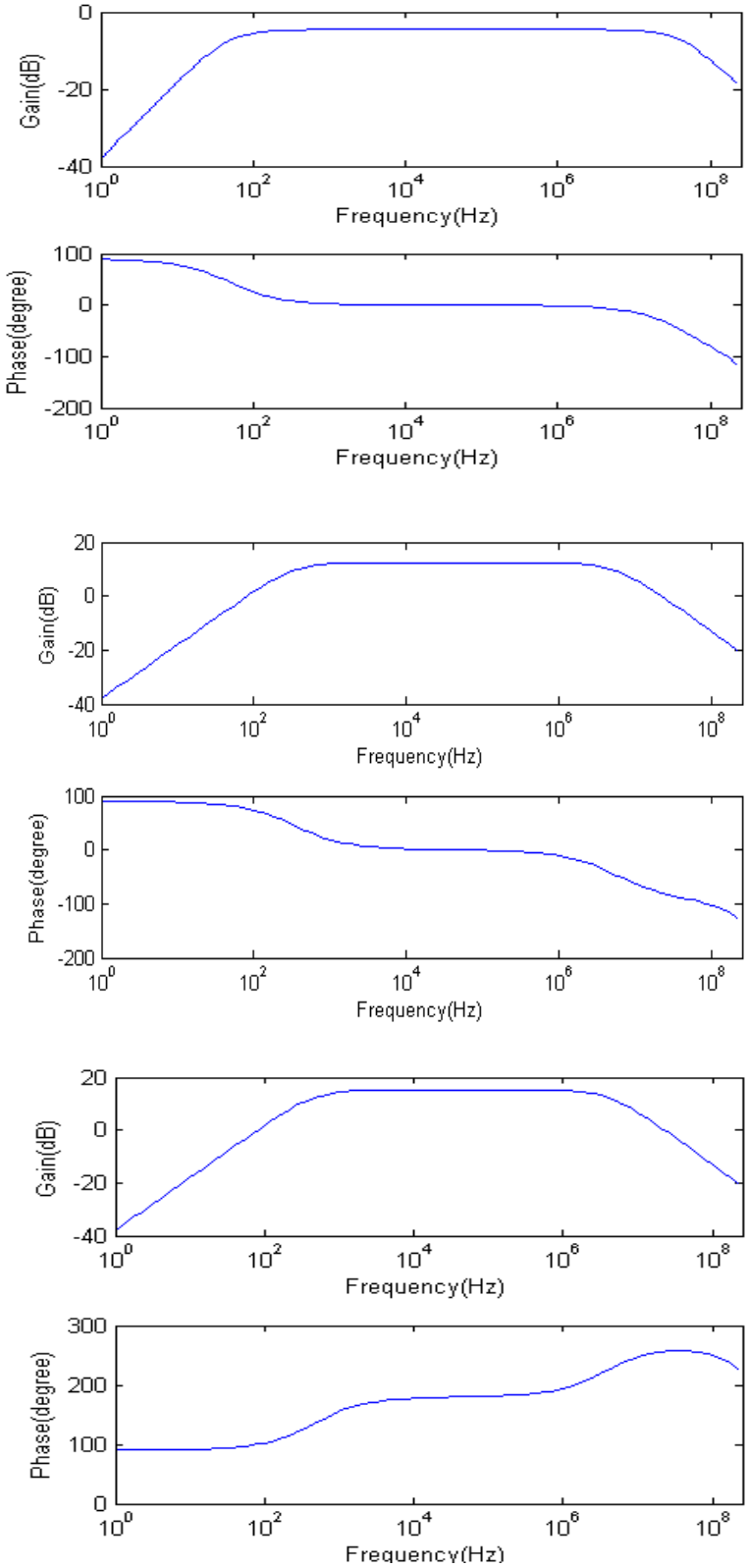

Figure 2.7: Effect of different amount of guarding on the frequency and phase response of EPS (a) 50% (b) 90% (c) 100%.

Guarding is provided by feeding a fraction of the output voltage back to conducting ring around the non-inverting input. The conducting ring in this case, is provided by a conducting PCB trace around the non-inverting input of the op-amp. The control has been provided to adjust the level of feedback voltage through a potentiometer, as illustrated in figure 2.4.

The voltage has been increased from minimum to maximum wiper settings of the potentiometer providing different percentages of the full scale. Figure 2.6 shows the corresponding effects on the gain and phase response. As expected, increasing feedback voltage resulted in increase in the overall closed loop gain and corresponding reduction in the bandwidth. In order to be effective the feedback signal must be in phase with the input signal leading to a 0^o phase shift at all frequencies in the pass band. As discussed in appendix A, positive feedback can lead to sustained oscillation if the feedback loop gain becomes reciprocal of the sensor gain, provided there is no phase shift, which must be avoided under all circumstances. The control provided must be used to steer away from this situation. In practice, too much feedback can lead to peaking in the frequency response which is also avoidable but with caution, this may be turned to advantage if particularly high gain is required over a certain range of frequencies.

Figure 2.6 (a) shows the frequency response when the potentiometer control was set at 0 position, corresponding to minimum feedback voltage. This is almost similar to figure 2.5 (a), which is the situation where there is almost no applied bootstrapping or guarding voltages. A gain of -11dB in the pass band and the top end roll-off of ~125 MHz can be observed. When the guarding voltage is increased to 25% of the full-scale setting (figure 2.6 (b)), the pass band gain increases to -8bB and this comes at the cost of reduction in the bandwidth, which in this case is limited to 82 MHz. A 50% setting (figure 2.7 (a)) corresponds to a -5 dB pass band gain and a bandwidth of 46 MHz and according to figure 2.7 (b) (90% of full scale setting) offers 12.5dB of pass band gain with a high frequency roll off at around 5.5 MHz. It is important to note here that with this significant improvement in pass band gain, the bandwidth is

reduced by almost an order of magnitude. The corresponding phase response plots shows that with higher guard setting (90%) the phase shift tends to depart 0^o from 120 KHz, as opposed to 1 MHz for 50% setting. This increased phase shift in the pass band frequencies is indicative of a reduction in the phase margin, which is a classic case of introducing increased positive feedback. Any further increase in the positive feedback will bring the circuit close to instability and must be avoided under all circumstances. Figure 2.7 (c) shows the frequency response for full guard setting and it is clear that an increased pass band gain (15 dB) is achieved at the cost of zero phase margin (pass band phase shift of 180^o), which is indicative of a peaked frequency response and may lead to sensor saturation.

2.4.3 Effect of compensation capacitance

Figure 2.8 (a) shows a simple non-inverting op-amp configuration. The output voltage can be expressed as $V_o = \left(\frac{R1+R2}{R1}\right) V_{in}$. For this circuit the frequency response is dictated solely by the standard gain-bandwidth product and is independent of the frequency of the input signal V_{in}. If a capacitor C1 is added in parallel to the resistor R1, as shown in Figure 2.7(b), this adds an additional pole to the transfer function of the circuit, determined by the time constant R1.C1. The output voltage V_o, in this case is $V_o = \left(\frac{Z1+R2}{Z1}\right) V_{in}$, where Z1 is the complex impedance resulting from the parallel combination of R1 and reactance of C1. The capacitor C1 provides a low impedance path for high frequency signals. The pole generated by the adding this capacitor combined with the gain-bandwidth product of the op-amp, a modified frequency performance is obtained.

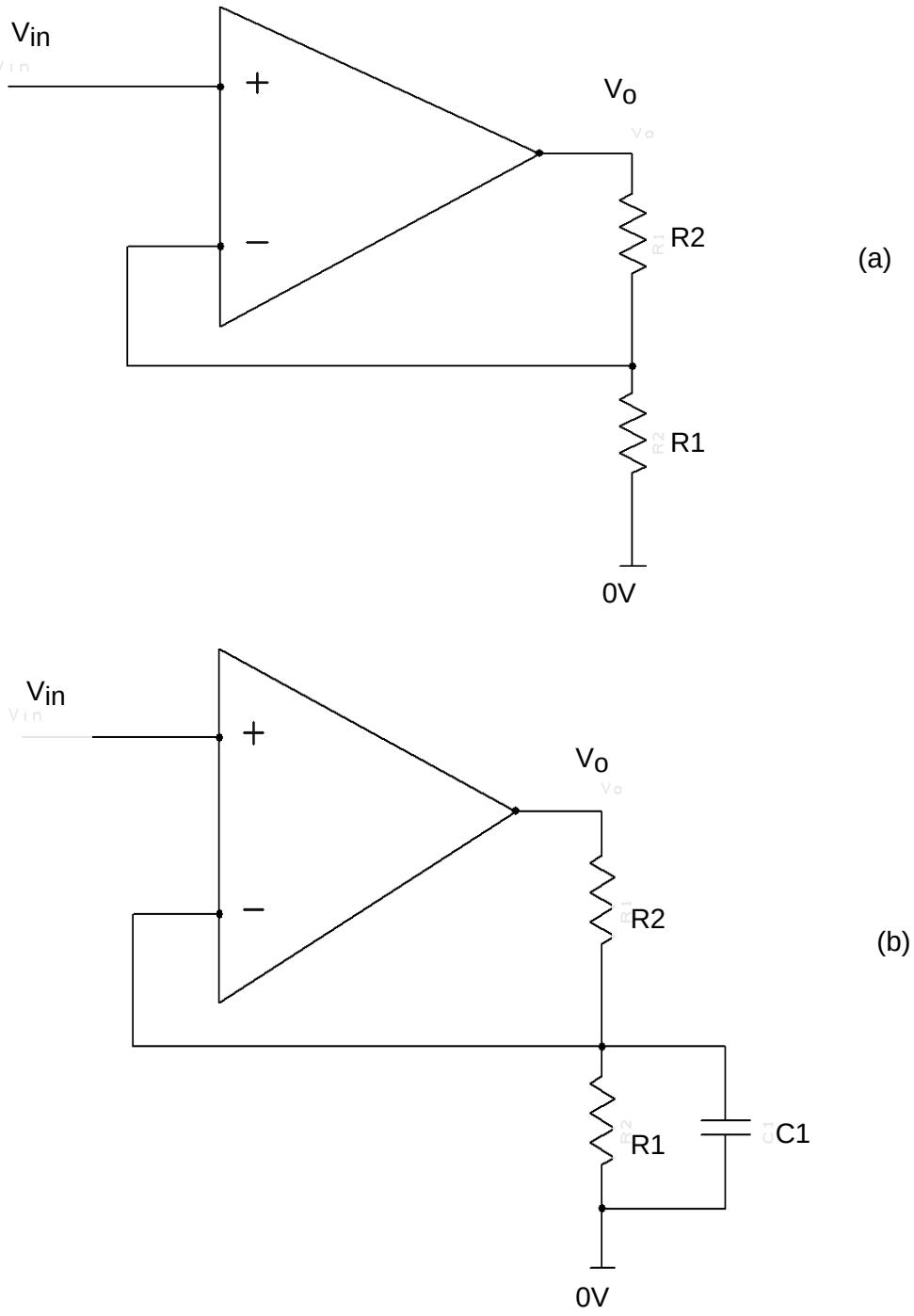

Figure 2.8: Non inverting Op-amp configuration (a) without (b) with compensation capacitor.

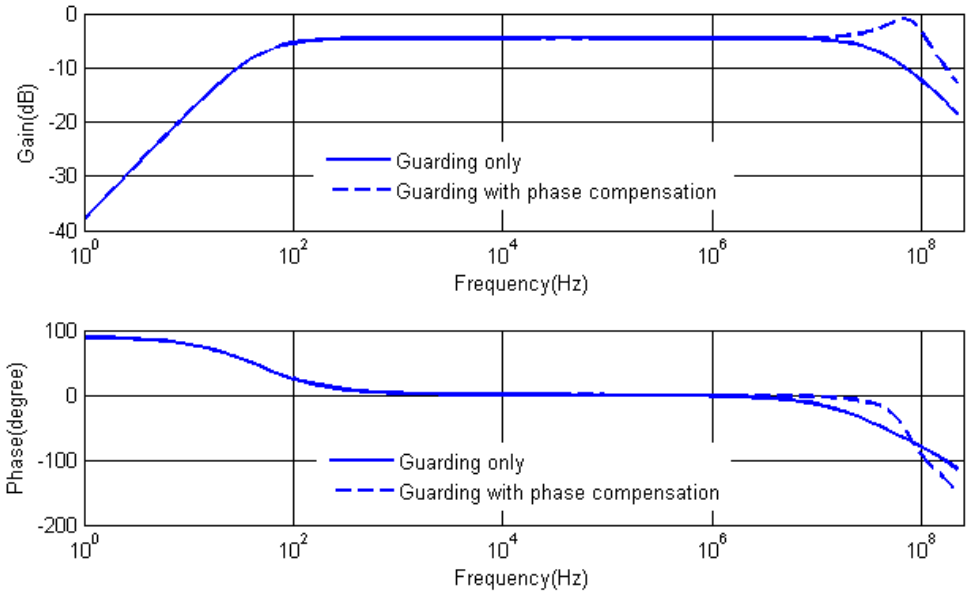

(a)

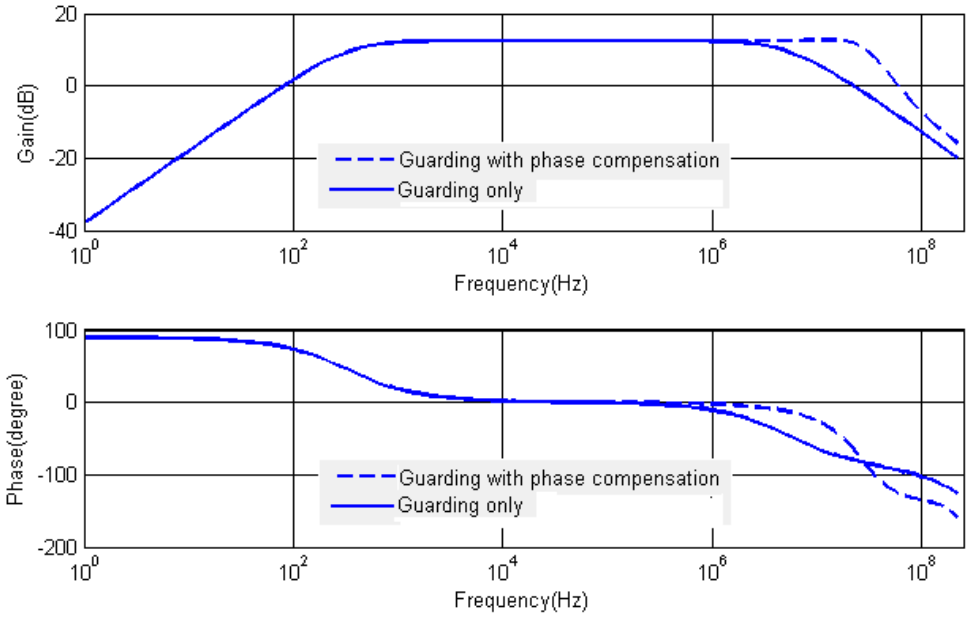

(b)

Figure 2.9: Effect of adding compensation capacitors along with applied guarding on the frequency and phase response of EPS (a) 50 % guarding applied (b) 90% guarding applied.

In practice the value of these capacitors are between 10-30pF and they are placed as shown in Figure 2.4. Figure 2.9 demonstrates the effect on the phase and frequency performance with the addition of these capacitors. The two responses in Figure 2.9 (a) and (b) correspond to two different guard settings of 50% and 90% respectively. The -3dB frequency in figure 2.9(a) in the solid trace is approximately 46 MHz and the same in the broken trace is around 130 MHz, which is almost a three times improvement. Improvement can also be noted in the corresponding phase response where the output is in phase over an extended range of frequency. The phase shift is below 45^o up to 37 MHz before the capacitors are added and after ~64 MHz, giving almost a twofold increase. At a higher guard setting of 90%, as shown in figure 2.9 (b), the -3 dB frequency with and without the capacitors are ~25 MHz and 5.5 MHz respectively. An improved phase response can also be seen in this case where it is less than 45^o up to ~5 MHz without the capacitors and ~15 MHz with them.

2.5 The characterisation of broadband EPS

2.5.1 PCB consideration

In section 2.4, the simulation of the circuit provides results consistent with the expected performance and therefore is a useful tool to begin the design of the high impedance, broadband sensor. It is to be noted that these simulations do not incorporate the PCB issues and considers the components used to be ideal, unless losses and stray values are deliberately added.

As discussed earlier in this chapter, the OPA 656 was chosen as the front end of the sensor. This section will discuss the construction of these sensors and the testing procedures for the purpose of characterisation. The actual performance of these sensors will also be discussed with the necessary results.

In order to build circuits with high speed op-amps such as OPA656, it is extremely important to pay attention to the PCB parasitics since their effects can severely degrade the actual performance limiting their usefulness for

practical applications. The datasheet for the OPA656 [**54**] provides useful information which, together with general RF circuit design issues are important to consider during the PCB design phase of the development.

In order to build the circuit with the intended characteristic performance, allowances were made during the circuit schematic and PCB design in Easy PC, a CAD circuit design package [**56**]. Standard FR4 double sided copper clad circuit boards were used to construct the sensors. Effort was made to use the underside of the board as an unbroken ground plane and all components to be populated on the top side. The PCB traces were kept as short as possible to reduce the inductance associated with them. High and low frequency bypass capacitors were placed close to the active device relatively thick traces were used for the power supply tracks. All the unused space on the board was grounded. All passive components were surface mount to eliminate any chances of undesired inductance that may be associated with leaded components.

The high impedance non-inverting section of the sensor was enclosed in a metal enclosure to isolate the sensitive area. The entire sensor electronics was soldered inside a grounded tinplated bright mild steel box [**57**] to reduce electromagnetic interference. Feed through ceramic capacitors were used at the power supply to minimise leakage of RF and electromagnetic interference.

The values of resistors in the negative feedback gain setting network are kept very low ~100 Ω for gain of +2, as recommended by the datasheet to minimise resistor noise and parasitic capacitance. The op-amps are directly placed on the circuit without any socket to eliminate chances of additional inductance which can cause troublesome parasitics and inhibit smooth operation. Series resistors in the range of 10-50 Ω were placed at the output of the sensor to isolate the feedback network from the load, especially if the load is capacitive, which often is the case. This can help reduce the peaking in the frequency response and increase the phase margin [**54**].

As discussed in section 2.4, positive feedback with controllable parameters is included in the circuit. In order to control the feedback signal in bootstrapping and guarding networks, cermet potentiometers [**58**] are used which are useful

because they are multi turn, giving precise control over the amount of signal required to be fed back, without saturating the sensor. Once the optimum level is determined experimentally for a sensor, the sensor does not require any further setting over the entire range of frequency it is designed for.

2.5.2 Testing procedure

The EPS is an ac coupled system. The sensor is coupled to the source capacitively and in most applications this coupling is small. It is therefore important to test these sensors with coupling capacitors which are very well defined, low loss and low leakage. The level of signal coupled to the sensor greatly influences its performances over the range of frequencies they are designed for. Moreover, these values are also important to estimate the effective input capacitance of the sensors.

In order to test these sensors, very precise values of capacitors were constructed in house. These capacitors were constructed by a colleague, Mr. Philip Watson. Very low loss, low dielectric constant and low dissipation factor dielectric duriods [**59**] were used in guarded coaxial casings with BNC input and SMA output connectors. A number of low capacitance values from 1.2 pF down to ~20 fF were available in this form factor.

An early test can be done to see linear operation of the sensor in which a known ac signal is coupled to the sensor through the known value of coupling capacitor and the output is observed on a broadband digital scope. Once a satisfactory output is seen on the scope, for a range of bootstrap and guard settings and over the bandwidth of the sensor, a frequency response is obtained using a spectrum analyzer.

2.5.3 Frequency response

The frequency response measurements at high frequencies were performed using a Rhode and Schwartz FSEA 30 spectrum analyzer [**60**] with a bandwidth of >3 KHz to 3.5 GHz. This spectrum analyzer has its own tracking generator output, which was capacitively coupled to the sensor under test and the frequency was swept from 10 KHz to 500 MHz. The value of the coupling capacitors were changed to observe the sensor performance for various coupling strengths. Clearly the lower the value of the coupling capacitor, the weaker the signal will be coupled and if it is small enough compared to the effective input capacitance of the sensor, the level of signal coupled to the sensor input will be strongly attenuated below a certain value, it will be comparable to the noise floor of the sensor, in which case no meaningful measurement would be possible.

In the course of developing versions of EPS that can work at frequencies in excess of tens of MHz, a number of milestones were achieved. This section will discuss the performance of three main circuits that were developed. As discussed in section 2.4, the sensor circuitry uses two stages to utilise the maximum bandwidth of the active part and add gain to the overall circuit. Where this has been common to all versions of the sensors, there are some major distinguishing aspects in the circuitry which provide improvements in the overall performance. The following are the major differences:

Version1: Uses two OPA 656 stages with bootstrapping and guarding network (Figure 2.10 (a))

Version2: Uses OPA 656 as the front end and OPA 847 as the second gain stage and which is DC coupled to the first stage and only uses guarding network (Figure 2.10 (b))

Version 3: Uses OPA 656 as the front end and OPA 847 as the second gain stage which is AC coupled and uses bootstrapping and guarding networks (Figure 2.10 (c))

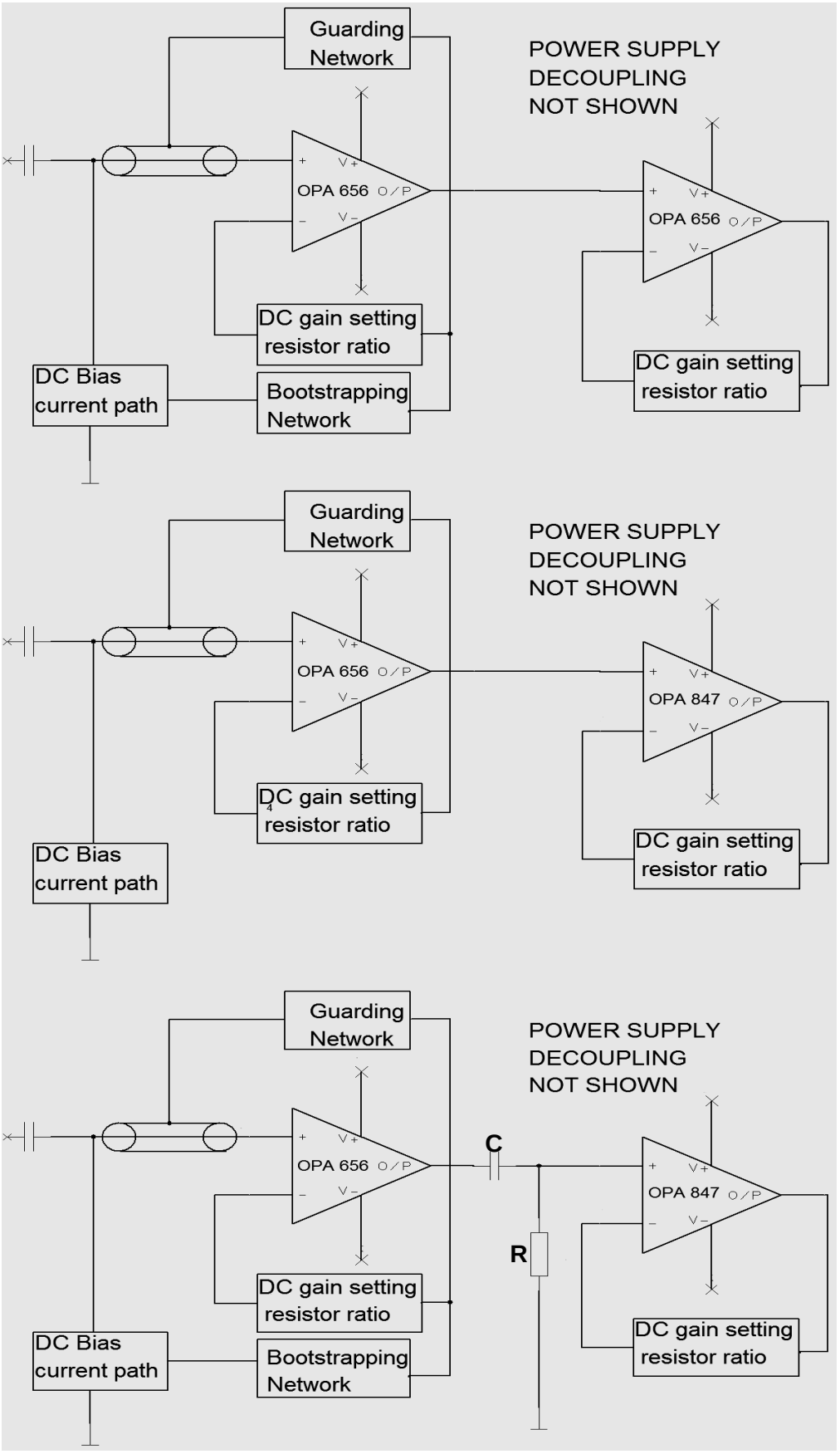

Figure 2.10: EPS circuits (a) version 1(b) version 2 (c) version 3.

Obviously, these versions were developed over the entire course of the project as and when it was felt that the existing performance could be enhanced and suitable components were found.

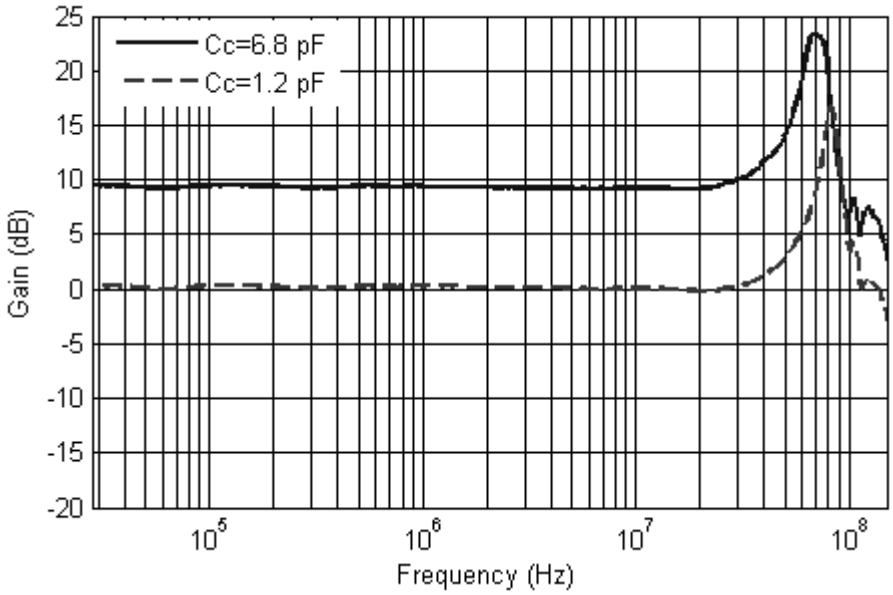

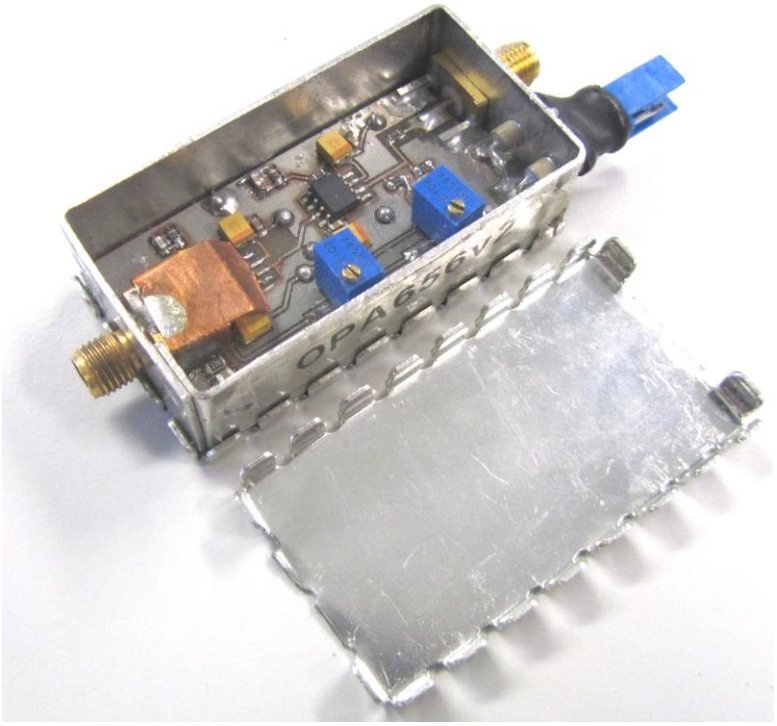

Figure 2.11: (a) Frequency response of an early version OPA 656 two stage sensor. (b) Image of an OPA 656 based EPS

Figure 2.10 (a) shows that this version uses two stages of OPA656 op-amps. Each stage was configured for noise gain of +2 because it was found that at this gain the OPA 656 can provide small signal bandwidth of 200 MHz, with a 0.1 dB flatness bandwidth of 30 MHz. Figure 2.11(a) shows the frequency response obtained for the version 1 sensor for two different coupling conditions. For coupling capacitance C_C= 6.8 pF which is a relatively stronger coupling, the sensor has flat response up to ~ 30MHz and a -3dB bandwidth at ~90 MHz. For C_C = 1.2 pF, less signal will be coupled to the sensor due to increased attenuation associated with weaker coupling, which results in a drop of overall gain. The flat bandwidth and -3 dB bandwidths however are not significantly affected. It was attempted for even weaker coupling but the noise level dominated and this version of the sensor was found to be actually useful for applications which require signal coupling of ~1 pF. Clearly this sensor is an improvement over the existing versions of the sensor in terms of high frequency performance and can be useful in a number of measurements requiring relatively stronger signal coupling. . An image of an actual OPA 656 based EPS is shown in figure 2.11 (b) which has been constructed by using surface mount techniques.

The OPA 656 has extremely high input resistance and relatively small input capacitance which makes it ideal for the sensor front end. The second stage of the sensor, however, does not need to have comparable input characteristics. As mentioned earlier, the main purpose of the second stage is to provide additional gain over the bandwidth for measuring a weaker signal. However, it should also have a noise performance nearly as good as that of OPA 656 The

OPA847 was found have a much superior frequency performance with a unity gain bandwidth of 3.9 GHz. However, according to its datasheet, the minimum gain for stable operation is +12, at which the working bandwidth is 600 MHz which is much wider than the bandwidth of OPA656 with +2 gains. Again the gain bandwidth product theory doesn’t predict this bandwidth for the specified gain and the reasons are same as that for OPA 656 discussed earlier in this chapter. This proved to be a suitable second stage for adding gain to the

sensor. It was also found that the input voltage noise of OPA847 is $0.85\ \mathrm{nV}\sqrt{\mathrm{Hz}}$ [**61**], which is even lower than that of the OPA656.

In an attempt to reduce the complexity of the circuit, some modification was done in the version 2 of the sensor. Bootstrapping, which is used to improve the low frequency performance of the sensors, was removed. This makes the lower end of the sensor frequency response to roll off at a higher frequency, but that can be an advantage if the design goal is to achieve only higher frequency performance. This results in a faster settling time because the sensor is desensitized at relatively lower frequencies. Figure 2.12 shows the frequency response of this sensor with different source to sensor coupling all the way down to 29 fF. Evidently the operable bandwidth of this version of the sensor is between ~70 KHz to ~200 MHz making it useful for higher frequency measurements requiring faster settling time.

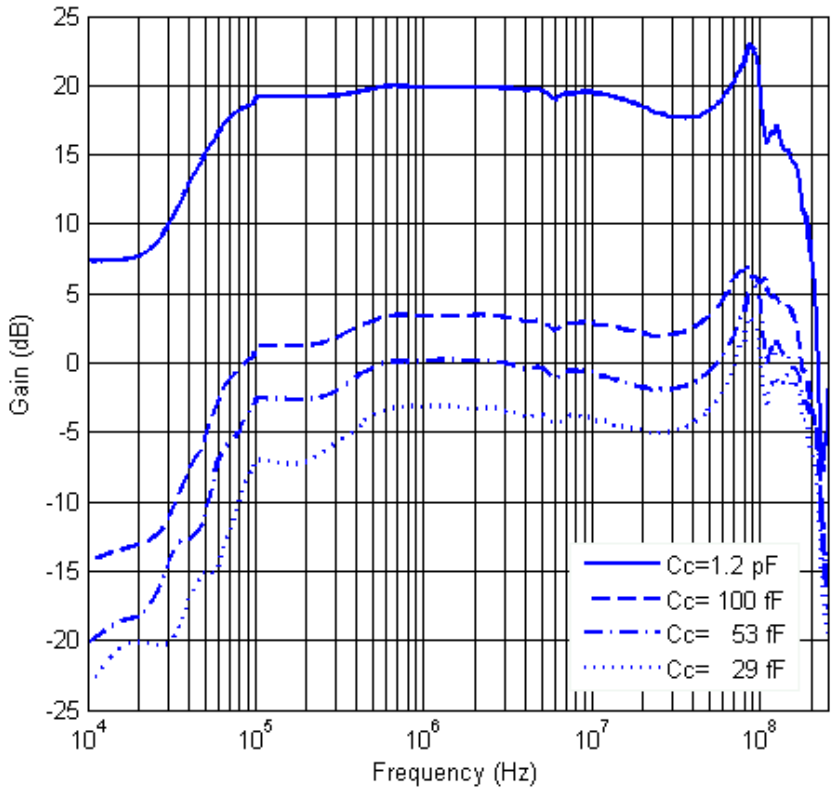

Figure 2.12: Frequency response of a version OPA 656 based senor with an OPA 847 as second stage optimised for high frequency applications with early low frequency roll off.

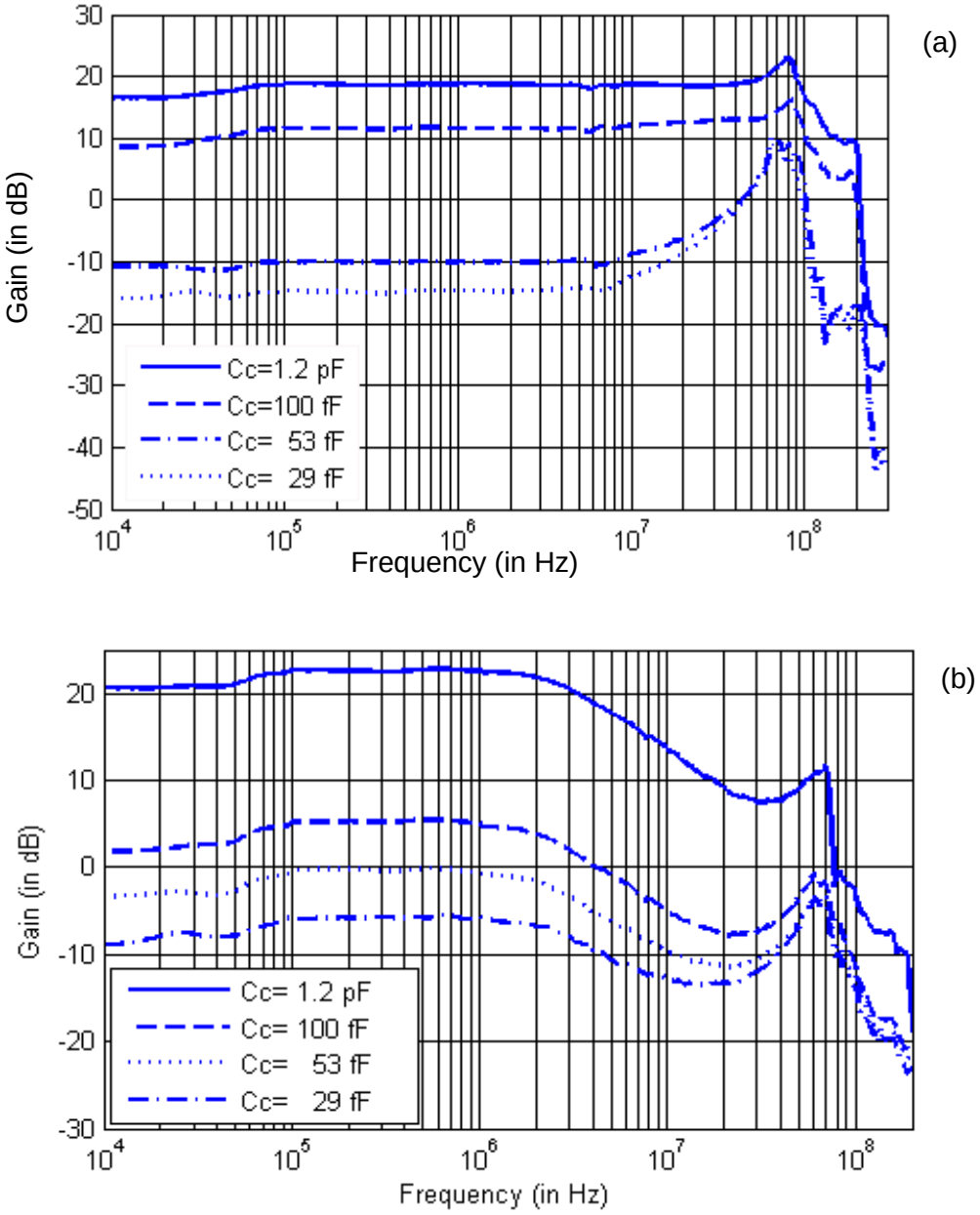

Figure 2.13: Frequency response of a later version OPA 656 based senor with a OPA 847 as second stage (a) with relatively less bootstrapping/ guarding (b) optimised for high spatial resolution

Finally, with an aim to have a single broadband sensor, version 3 was developed. In this version, bootstrapping was reintroduced in the circuit and an OPA 847 second stage was ac coupled with capacitor C as shown in Fig 2.10 (c). The resistor R forms DC path for OPA 847 and together with C,

forms a high pass filter with corner frequency below the lower -3 dB frequency of the sensor. With due consideration to the PCB layout, a new sensor was constructed with an aim to achieve not only a wider frequency performance, but also a lower input capacitance. With such characteristics, a sensor would be useful for broadband applications requiring higher spatial resolution such as surface microscopy, discussed later on in this thesis.

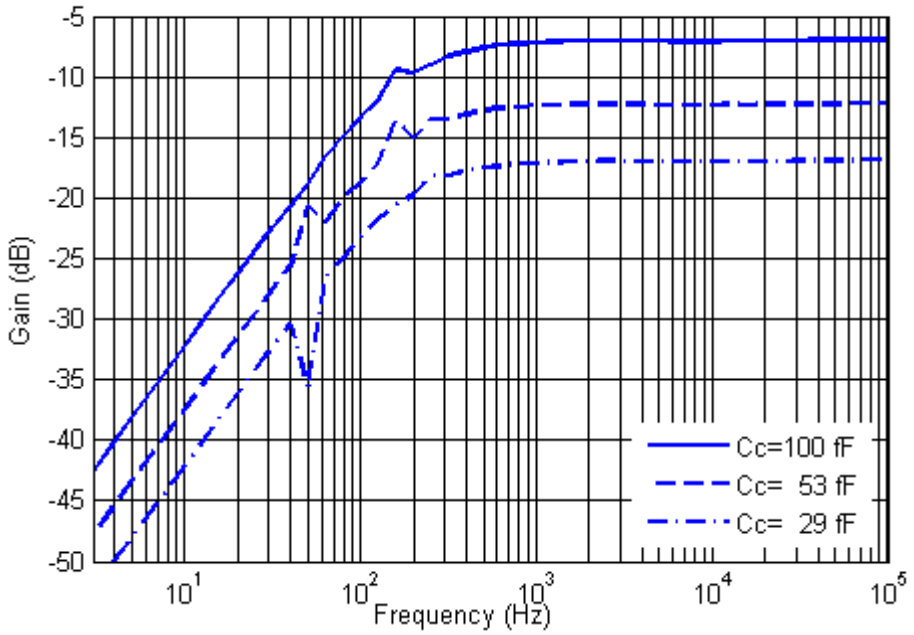

Figure 2.14: Lower end of frequency response of version 3 sensor.

Figure 2.13 (a) shows the frequency response obtained for the version 3 of the sensor with different coupling capacitances. Clearly, this sensor produces measurable output down to tens of femtofarad coupling which suggests it has a relatively smaller input capacitance compared to the version 1. The high frequency -3 dB roll off is approximately 100 MHz with a usable bandwidth of ~200 MHz for measurable signals. Fig 2.13 (b) shows a frequency response of the same sensor optimised for high spatial resolution applications, with increased bootstrapping and guarding feedback. These applications are described in chapter five, six and seven, by adjusting the feedback networks.

The Rhode and Schwartz FSEA 30 spectrum analyzer used for characterising the sensors has a bandwidth of 10 KHz to 3 GHz. This makes it unsuitable for characterising circuits with a frequency response outside it's bandwidth. Since the version 3 sensor was designed to operate at relatively low frequencies as well, another instrument was used to obtain the lower end of its frequency response. Figure 2.14 shows the frequency response of the sensor from 1 Hz to 100 KHz for different coupling conditions from 100 fF to 29 fF. Evidently, the sensor can work all the way down to 100 Hz. This result together with the higher frequency counterpart shown in Fig 2.13, the version 3 EPS can be made to work over frequencies from 200 Hz to 200 MHz, making it a single broadband electric field sensor.

2.5.4 The EPS input impedance

The final version of the sensor has been characterised more comprehensively for various parameters other than the frequency response. Figure 2.15 shows an equivalent circuit of a standard EPS showing the effective equivalent resistor Rin and capacitors Cin. These are important parameters for a given EPS and this section presents a mathematical analysis to establish their relationships with known and measurable quantities.

The lower end of the frequency response of a standard ac coupled EPS is dictated by the input resistance Rin and the coupling capacitance Cc and is given by $f_{-3dB} = \frac{1}{2\pi \cdot Rin \cdot Cc}$ which makes Rin as given in equation. 2.4

$$Rin = \frac{1}{2\pi \cdot f_{-3dB} \cdot Cc} \tag{2.4}$$

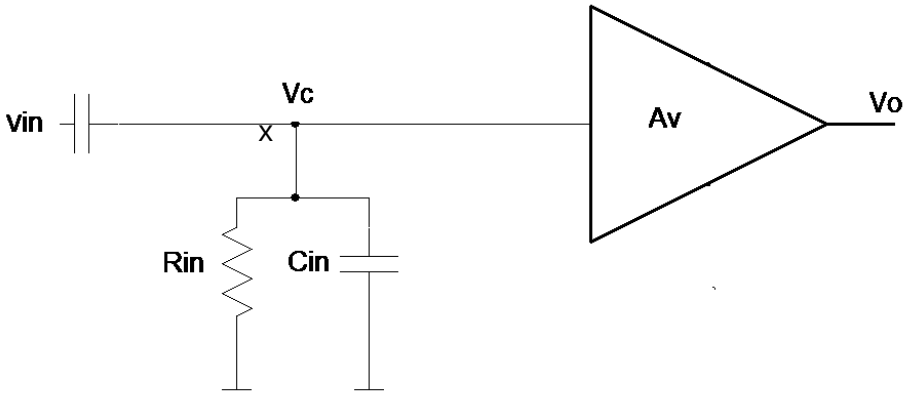

Figure 2.15: Equivalent circuit of a standard EPS

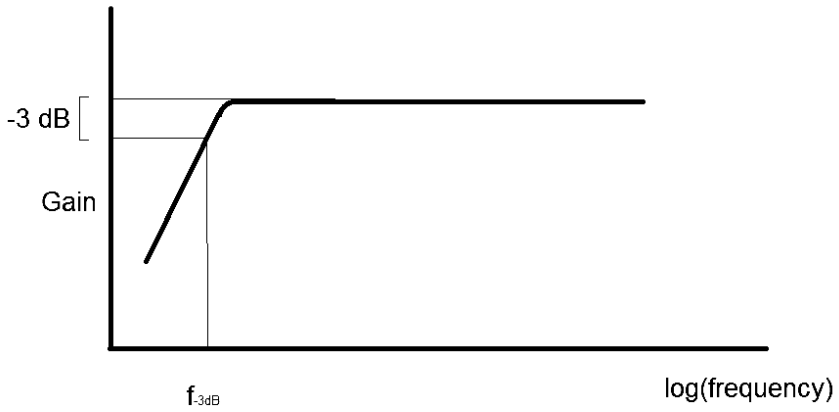

Figure 2.16: A frequency response showing the lower cut-off

The input impedance Zin of the sensor is a parallel combination of the input resistance Rin and reactance Xin of the input capacitance Cin and can be expressed by equation 2.5.

$$\mathrm{Zin}=\frac{\mathrm{Rin}\cdot\mathrm{Xin}}{\mathrm{Rin}+\mathrm{Xin}} \tag{2.5}$$

Where

$$\mathrm{Xin}=\frac{1}{2\pi\cdot\mathrm{f}\cdot\mathrm{Cin}} \tag{2.6}$$

This makes Zin as given in equation 2.7

$$\mathrm{Zin}=\frac{\mathrm{Rin}}{2\pi\cdot\mathrm{f}\cdot\mathrm{Cin}\cdot\mathrm{Rin}+1} \tag{2.7}$$

Dividing A.8 by Rin gives

$$\mathrm{Zin}=\frac{1}{2\pi\cdot\mathrm{f}\cdot\mathrm{Cin}+\left(\frac{1}{\mathrm{Rin}}\right)} \tag{2.8}$$

Since for practical purposes Rin is too big, 1/Rin tends to be negligible and can therefore be dropped from 2.8 giving equation 2.9 which is much simpler.

$$\mathrm{Zin}=\frac{1}{2\pi\cdot\mathrm{f}\cdot\mathrm{Cin}} \tag{2.9}$$

Equation 2.9 shows that the effective input impedance is very much dominated by the value of input capacitance Cin and therefore the input of the EPS effectively forms a capacitive voltage divider. The node voltage Vc can be expressed by equation 2.10

$$Vc = \frac{Xin}{Xin+Xc} Vin \tag{2.10}$$

Where Xc is the reactance of the coupling capacitor Cc and related to it similar to 2.6. The reactance terms in Equation 2.6 can be replaced by their actual values in terms of their respective capacitances which gives equation 2.11.

$$Vc = \frac{Cc}{Cin+Cc} Vin \tag{2.11}$$

However, since the sensor has a gain Av,

$$Vo = Av \cdot Vc \tag{2.12}$$

Using 2.12 in 2.11,

$$Cin = \left(\frac{Av \cdot Vin}{Vo} - 1 \right) Cc \tag{2.13}$$

From figure 2.14, we get the low frequency roll off (f_{-3dB}) corresponding to the coupling capacitor (C_c). This information can be used to calculate the input resistance of this sensor by using equation 2.4, which is found to be 15 GΩ. From equation 2.13, we calculate Cin of the sensor as 0.5 pF for a 100 fF coupling capacitance.

2.5.5 Noise spectral density

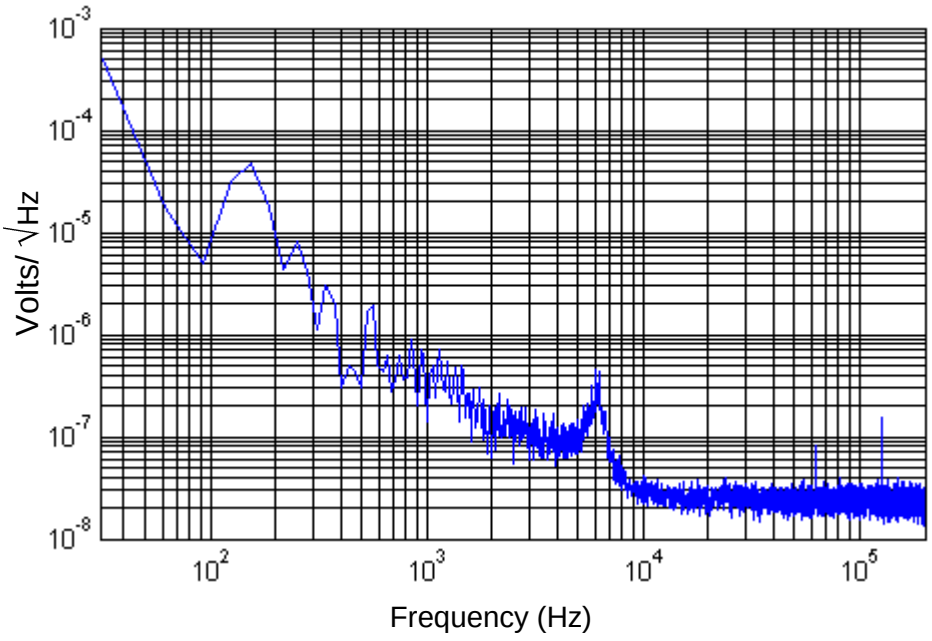

(a)

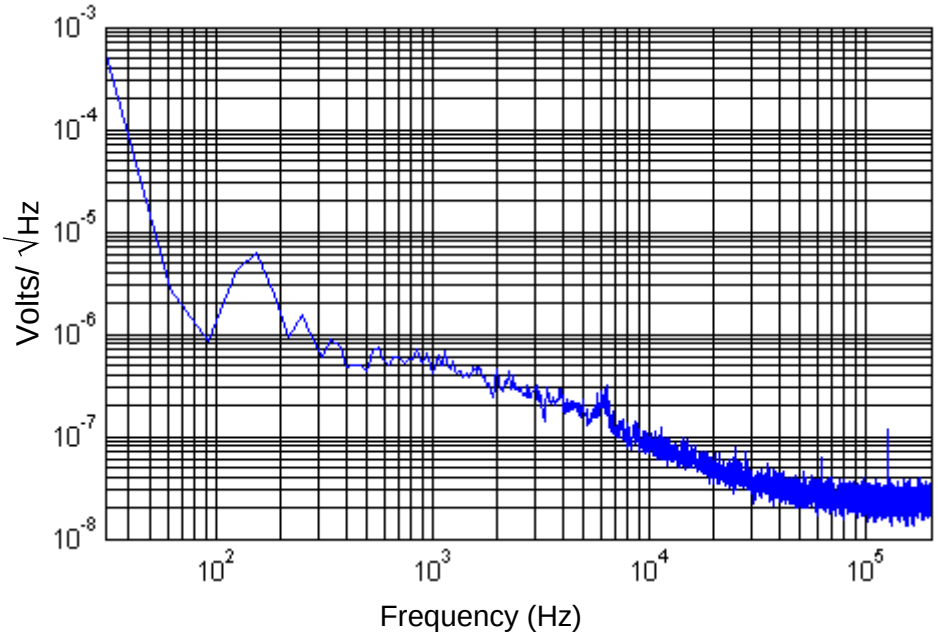

(b)

Figure 2.17: (a) Open circuit (b) Short circuit noise spectral density

The op-amps used to construct EPS offer very good current and voltage noise performances. However, when they are configured as weakly coupled ac electric field sensors, it is important to learn their noise performance.

It was not possible to characterise the final version of broadband EPS (version 3) for noise performance over its entire bandwidth using a single spectrum analyser because of its bandwidth being very broadband. A low frequency PULSE multi frequency analyzer [**62**] , configured to measure noise spectral density was used for characterising the sensor noise performance up to 200 KHz, the maximum operable frequency for the equipment. Figure 2.17 (a) and (b) show the open circuit and short circuit noise plots for the version 3 of the sensor between 30 Hz to 200 KHz. To obtain the open circuit noise characteristic the input of the sensor was left floating and for short circuit, the input was connected to the ground. As can be seen the average open circuit noise for frequency >10 KHz is 23.9 nV/√Hz and the average short circuit is 28.4 nV/√Hz, both referred to the input of the sensor.

In order to get an idea of the noise performance at higher frequencies, which the low frequency equipment cannot perform, we apply the following experimental approach [**49**] [**63**].

$$\frac{\text{Volt}}{\sqrt{\text{Hz}}} = \frac{V_{out}}{2\sqrt{2}\times A_v \times CF \times \sqrt{\Delta f \times NEB}} \qquad (2.14)$$

The above equation gives a measure for estimating thermal noise. The sensor was connected to a wideband oscilloscope (bandwidth >200 MHz) with the input open circuited, thermal noise was observed which has a uniform power distribution with respect to the frequency and can be termed as white noise. The amplitude of the white noise gives the value for V_{out} in equation (2.14).

A_v is the gain of the circuit, CF is the crest factor which is defined by the ratio of peak-to-peak to RMS value of a waveform and for thermal noise it is taken to be approximately 4 [**63**]. The Δf is the -3dB bandwidth of the sensor, NEB is the noise equivalent bandwidth which ratio of noise bandwidth to 3 dB bandwidth.

Its value depends on the roll off behaviour of the circuit and if the roll off is more than 3rd order, its value tends to unity [**63**].

For our final version of sensor, we used a 200 MHz scope to observe peak to peak value of sensor output V_{out} = 50 mV, A_v =24, CF= 4, Δf=110 MHz and NEB =1.15 and the value we got was 16.4 nV/$\sqrt{}$Hz, referred to the input of the sensor which is close to the figures obtained by the low frequency equipment used to characterise the sensor for noise up to 200 KHz, giving a degree of certainty for the correctness of this value.

Chapter 3

Nuclear Quadrupole Resonance

3.1 Introduction

Nuclear Quadrupole Resonance (NQR) is a magnetic resonance phenomenon seen in molecules due to the interaction of the charge distribution between the atomic nucleus and the surrounding electron cloud [**64**] [**26**] [**27**]. In order to understand the processes involved in quadrupole resonance, consider figure 3.1 [**65**].

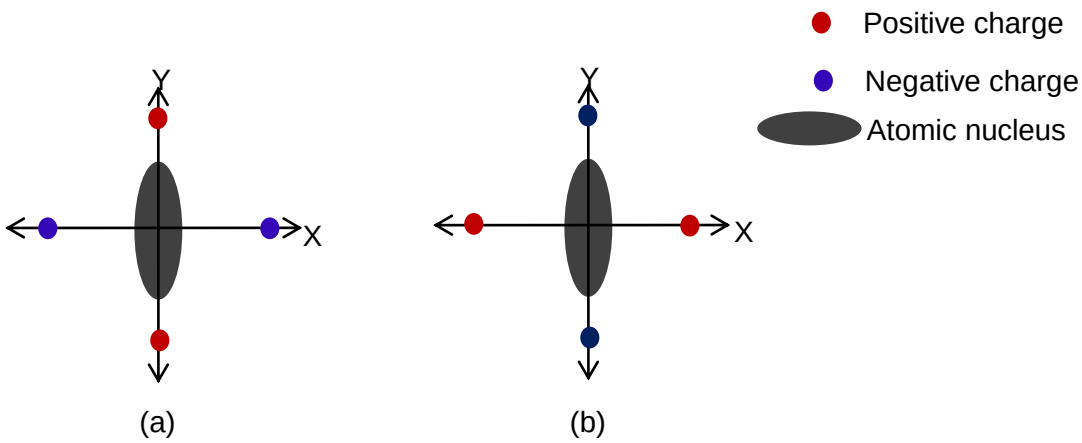

Figure 3.1: A non-spherical nucleus in the vicinity of two pairs of equal and opposite charges. (a) Nucleus tip closer to positive charges (b) Nucleus tip closer to negative charges.

It is simple to conclude that the orientation shown in figure 3.1(b) is more stable than 3.1(a), because the tip of the positively charged nucleus is closer to the

negative charges along the X-axis, resulting in a lower energy state. If the atomic nucleus was perfectly spherical, this orientation would not have mattered.

A non-symmetric or non-spherical time averaged charge distribution of the atomic nucleus is indicative of having spin quantum number $I > ½$. It will be discussed in the subsequent sections in this chapter, that due to this same reason nuclei with spin quantum number of greater than ½ also possess an electric quadrupole moment which interacts with electric field, provided by the surrounding electron cloud. Due to the presence of the electric field gradient, different quadrupolar energy levels are formed. When an external RF energy at a certain frequency is applied, transitions between these energy levels take place. Due to the presence of magnetic moments in the nucleus, the orientation of the nucleus is changed and it becomes aligned with the magnetic component of the applied electromagnetic energy [**27**]. The nuclear quadrupole resonance signal is released when the nucleus reorients itself in the equilibrium position.

The subject of this chapter is to discuss, in more detail, principles of NQR, or in general, magnetic resonance, the experimental set up and the use of EPS to acquire the signal by measuring the electric field component of the signal, as opposed to the conventional technique of measuring the magnetic component using a pickup coil.

A number of textbooks [**65**] [**66**] treat the subjects of magnetic resonance and quadrupolar interactions with relevant equations and quantum mechanical descriptions and have been consulted to present some of the concepts essential to understand the subject matter in the following sections.

3.2 Electromagnetic interactions

The nucleus of an atom can be visualised as a small lumpy magnet with a magnetic moment and a positive charge distribution. The charge distribution of the nucleus can be symmetrical like a perfect sphere or non-symmetric, like an ellipsoid. The lumpy charge distribution of the nucleus can be expressed as a superposition of electric multipoles:

$$C(r) = C^{(0)}(r) + C^{(1)}(r) + C^{(2)}(r) + C^{(3)}(r) + \ldots. \quad (3.1)$$

In equation (3.1), $C^{(0)}(r)$ represents a spherical charge distribution, $C^{(1)}(r)$ represents dipolar charge distribution, $C^{(2)}(r)$ represents quadrupolar charge distribution and so on. This situation is pictorially shown in figure 3.2 [**66**].

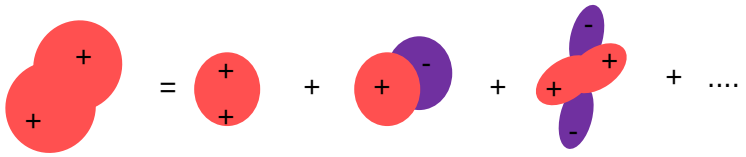

Figure 3. 2: Decomposition of nuclear charge distribution into electric multipole components.

The magnitude of the $C^{(0)}$ term is the total electric charge, the magnitude of the $C^{(1)}$ term is the electric dipole moment of the nucleus and the magnitude of the $C^{(2)}$ term is the electric quadrupole moment, and so on.

If this nucleus is placed in an electric potential distribution V(r), the nucleus will adapt an equilibrium position by orienting itself at the minimum of the electric potential as shown in figure 3.3.

The electric potential distribution may also be represented by superposition according to equation (3.2).

$$V(r) = V^{(0)}(r) + V^{(1)}(r) + V^{(2)}(r) + V^{(3)}(r) + \ldots. \quad (3.2)$$

$V^{(0)}$ represents the electric potential at the centre of the nucleus, $V^{(1)}$ represents the gradient of the electric potential at the centre of the nucleus and $V^{(2)}$ represents gradient of the gradient and so on. The energy associated due to the interaction between the nucleus and the electric potential distribution can also be expressed in the similar manner, as the sum of various charge multipoles and different aspects of the potential as shown in equation (3.3).

$$E(r)= \int C^{(0)}(r)V^{(0)}(r)\,dr + \int C^{(1)}(r)V^{(1)}(r)\,dr + \int C^{(2)}(r)V^{(2)}(r)\,dr +... \qquad (3.3)$$

The first term represents the electrostatic force between the nucleus and the electrons so this gives important information about the atomic and molecular structures. The second term represents the interaction between the nuclear electric dipole moment and gradient of the electric potential which is the electric field. Since the electric field inside an atom is extremely high, this term is expected to be very large. However, it has been proved by nuclear physicists that within experimental error, there is no nuclear electric dipole moment which means this term vanishes. In fact, all electric terms, which are the odd terms in equation (3.3), vanish.

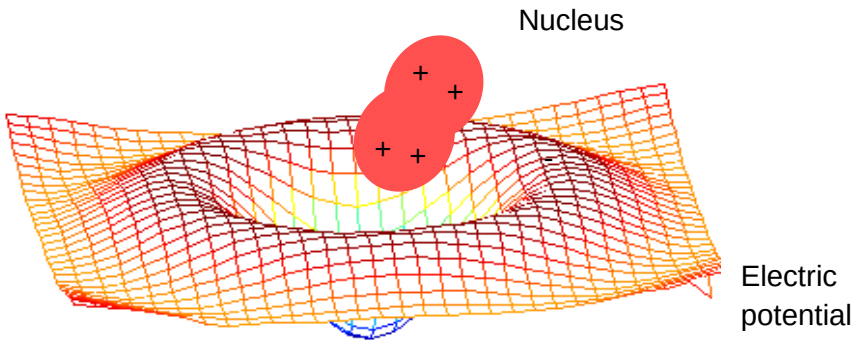

Figure 3. 3: Interaction of the nucleus with the electric potential distribution.

In addition to this, there is another interesting symmetry property linking the shape of the nucleus to the value of the nuclear spin, given by equation (3.4).

$$C^{(n)}=0 \text{ for } n > 2I \tag{3.4}$$

This suggests that equation (3.1) does not go on forever but cuts off at $2I$. Hence, if we consider $I = ½$, for spin-1/2 systems such as Hydrogen, there is only one term $C^{(0)}$, making the nuclear charge distribution completely spherical. This also follows that for such an atom, there is only one energy term due to the interaction of the nuclear charge and electric potential energy and the electric energy in the system is completely independent of the orientation or the internal structure of the atom, shown in the previous section in figure 3.1.

For higher spin nuclei with $I > 1/2$, the charge distribution is not spherically symmetrical. The electric energy term contains the 0^{th} and 2^{nd} term. The effect of the second term is higher which is due to the interaction of the nuclear electric quadrupole moment and the *gradient of the gradient of the electric potential* or the second derivative of the electric potential. Since the gradient of the electric potential is the electric field, the second derivative of electric potential is therefore, the *electric field gradient (EFG)*.

The above discussion reveals two very important aspects for higher spin nuclei. Such nuclei have asymmetrical charge distribution and therefore have a nuclear electric quadrupole moment and due to the presence of electrons in the vicinity of the nucleus, there also exists an EFG. Therefore, there is a strong interaction between the nuclear electric quadrupole moment and the EFG.

3.3 Spin

3.3.1 Angular momentum

It is now clear that the spin associated with the nuclei is an important property. The charge distribution of the atomic nucleus is directly affected by the value of the spin associated with it. What is not so clear is the spin itself. What is this spin and how does it occur?

To explain the spin associated with an atomic nucleus, one often turns to quantum mechanics. In this case, however, the spin will be described with a less mathematically rigorous approach.

Let's begin with a more familiar concept of angular momentum of a rotating body. It is easy to perceive the association of angular momentum, a vector quantity, when a body rotates about a certain axis. The direction of angular momentum is along the axis of rotation and it points outwards or inwards depending on whether the object is rotating clockwise or counter-clockwise, respectively.

Quantum mechanics suggests that angular momentum is quantized and since the energy associated with a rotational body is proportional to the square of the total angular momentum, it is also quantized. More precisely, these assertions are applicable to microscopic particles such as atoms in a molecule or subatomic particles such as electrons and the nucleons. If we consider a molecule with two constituent atoms as an example, there will be a set of stable rotational states and the total angular momentum, L_{tot} will have one of the values given by equation (3.5).

$$L_{tot} = [J(J+1)]^{1/2}\,\hbar \tag{3.5}$$

Where, J is an integer such as 0,1,2,3 ... and $\hbar$ =h/2π =reduced Planck's constant $\cong$1.054x10^{-34} Js. Hence, the molecule will be in one of the stable rotational states with total angular momentum of zero, $\sqrt{2}$ or $\sqrt{6}$, etc. The actual rotational state will depend on its environment and history. The total angular momentum determines the speed of rotation but does not specify the direction, for which another quantum number, the azimuthal quantum number, is used. The azimuthal quantum number is represented by M_J and it takes one of the 2J+1 (M_J = -J, -J+1... J) values. M_J gives some information about the direction of rotation. At thermal equilibrium, in absence of any external energy such as applied electric or magnetic field, each of 2J+1 state have same energy and are called degenerate states. However, when an external field is applied, the degeneracy is broken, resulting in slightly different energy at each sublevel. This is called Zeeman effect.

3.3.2 Spin angular momentum

Spin is a form of angular momentum but it is intrinsic to the particle. It is not produced by its rotation. Spin is an intrinsic physical property of microscopic particles such as mass, charge and magnetism. It can just be thought to be intrinsic angular momentum that is just there within the particle. Unlike the other physical properties such as mass, charge and magnetism, which are more intuitive because they have macroscopic manifestations, spin remains a microscopic phenomenon which does not make it to the macroscopic world. The closest macroscopic analogy that can be given is of a planet rotating around the Sun and also spinning about its own axis, but in case of, say, the electron, there is no concept of its own axis and therefore it is not quite the same. Nonetheless, spin is very important and has a direct consequence on the stability of molecules and their chemical behaviour.

Like total angular momentum due to rotation, spin angular momentum is also quantized and takes the form [S(S+1)]$^{1/2}\hbar$, the symbol S has been chosen to distinguish from J which is the rotational angular momentum. Particles with spin

S have (2S+1) sublevels, which are degenerate at equilibrium i.e in the absence of external fields.

Each elementary particle has a particular value of spin quantum number S. It can be an integer value like 0, 1, 2... or half integers such as 1/2, 3/2, 5/2... etc. Particles with integer spin are called bosons and those with half integer spin are called fermions.

Therefore for particles like electrons, there are two kind of angular momentum: (i) 'conventional' angular momentum which arises due to the orbital motion of the electron around the atomic nucleus and (ii) 'Intrinsic' or spin angular momentum which arises from nothing. It needs to be accepted as a feature of the electron which is always the same, spin=1/2.

It is important to mention that angular momenta can be combined. If a system has two particles, each one being a source of angular momentum, the total angular momentum of such a system will be either the sum of the two angular momenta, or the difference of the two or any of the values in between in integer steps, just like the case with a single rotating particle discussed in section 3.3.1. Equation 3.6 shows this discussion in a mathematical form for a system comprised of two particles with angular momentums J_1 and J_2. The total angular momentum of the system is $[J_3 (J_3 +1)]^{1/2}\hbar$, where J_3 takes one of the following possible values.

$$J_3 = \begin{cases} |J_1 - J_2| \\ |J_1 - J_2| + 1 \\ . \\ . \\ . \\ |J_1 + J_2| \end{cases} \qquad (3.6)$$

3.4 Nuclear spin

3.4.1 The nucleons

It is important to mention some of the established facts which will set the stage for the discussion to follow. The fundamental particles of the universe are leptons, quarks and force particles. Any detailed discussion of these particles has been avoided except for their basic properties. There are variants of each of these fundamental particles which are of interest to the particle physicists and are specialised topics in their own right.

Leptons are light mass particles. A good example of leptons is electron, which has an electric charge e= -1.602×10^{-19}C and spin-1/2.

Quarks are relatively heavy and there are six known flavours, three with electric charge of +2e/3 and the other three with –e/3. All quarks have spin 1/2.

Force particles are responsible for mediating the interaction between other particles. The photon is an example of a force particle which is the particle manifestation of electromagnetic field. Light is known to have a stream of photons. Photons have spin-1, no charge and no mass. Other known force particles are gluons and vector bosons, representing strong and weak electromagnetic forces. Gluons are responsible for holding the nucleus and its constituent particles together and vector bosons are responsible for radioactive β-decay.

The atomic nucleus consists of neutrons and protons. A neutron is composed of three quarks, two with charge –e/3 and one with charge +2e/3, making it electrically neutral and with spin 1/2 because of the spins associated with the quarks. Two of the quarks have anti parallel spin, cancelling each other out and the third one with a spin 1/2, giving the net spin to the neutron.

A proton is also composed of three quarks, two with charge +2e/3 and one with charge –e/3, giving it a net positive charge +e. The spin of the proton is 1/2, following the same reasoning as for neutrons.

3.4.2 Nuclear spin states

An atomic nucleus is composed of neutrons and protons. Neutrons and protons both have spin and therefore an ensemble of nuclei also possess a net spin, added according to equation 3.6. The total spin of a nucleus can be zero, half integers or full integers depending on the nuclear composition i.e the number of protons and neutrons present within the nucleus. The total spin associated with a nucleus is called nuclear spin quantum number and as described earlier, it is denoted by I. For example, a nucleus with a single proton, such as ^{1}H in its nucleus, will have a nuclear spin of 1/2, the spin due to the single proton.

As discussed in section 3.3.2, in context with electron spin, there can be $2I+1$ degenerate energy sublevels, known as nuclear spin states or eigenstates. With an applied electric or magnetic field, this degeneracy is broken resulting in nuclear Zeeman splitting.

3.5 Magnetic Resonance

3.5.1 Magnetic materials

Any substance with magnetic moment μ, permanent or induced, interacts with magnetic field B in a manner to minimise the energy of interaction, E_{mag}:

$$E_{mag} = -\mu \cdot B \qquad (3.7)$$

The magnetic moment μ, as mentioned, can be permanent, which is the case with ferromagnetic materials, or induced, which means that the μ is temporary and is present due to the influence of an external magnetic field. Induced moments take some time to build up and its equilibrium value is directly proportional to a physical parameter called magnetic susceptibility, χ. The magnetic susceptibility χ determines the magnetic behaviour of the material and is negative for diamagnetic and positive for paramagnetic materials. A diamagnetic material pushes the magnetic field out of the material where as

paramagnetic pulls the magnetic field inwards. A detailed discussion on these magnetic properties and quantum mechanical reasoning for their existence is beyond the scope of this thesis and therefore excluded from this discussion.

3.5.2 Microscopic magnetic interactions

The microscopic magnetism associated with subatomic particles is instrumental in magnetic resonance. Atoms contain a nucleus and a number of electrons, each of which has spin angular momentum and magnetic moments and therefore, are sources of magnetism. The electrons circulating around the nucleus are also responsible for generating magnetic field. In diamagnetic materials, the magnetic effect due to the circulating electrons is higher than the nuclear or electron moments.

The nuclei and the electrons are permanent magnets with intrinsic magnetic moments μ which is very closely linked with the spin:

$$\hat{\mu} = \gamma \hat{S} \tag{3.8}$$

Here, the hats (^) represent quantum mechanical operators and γ is called the gyromagnetic ratio, a physical parameter with units of *rad* $sec^{-1}T^{-1}$. A positive γ indicates that the spin angular momentum is parallel to the magnetic moment and a negative value indicates the opposite.

3.5.3 Nuclear magnetization

Each nucleus can be treated as a small magnet with a non-zero magnetic moment and spin angular momentum. In a diamagnetic sample the nuclei are in isotropic distribution. The spin polarization axis is the direction in which the spin angular momentum of each nucleus points, as shown in figure 3.4. In perfect

isotropy, which exists at thermal equilibrium, the vector sum of the magnetic moments, cancel each other out leading to a zero net magnetic moment.

When a magnetic field is suddenly turned on, the moments associated with each of these nuclei tries to align them so that the total magnetic energy of interaction (equation 3.7) is at a minimum. This results in a build up of net magnetic moment in the direction of the applied field. The vector sum of the spin momenta can be either along or opposite the direction of the total magnetic moment depending on the polarity of the gyromagnetic ratio. The direction of total spin angular momentum is called the spin polarization axis.

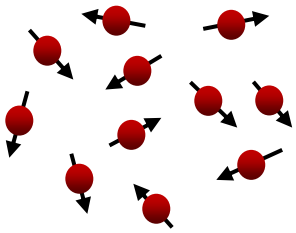

Figure 3.4: Random distribution of spin polarization.

This alignment of spin polarization in the direction of magnetic field is not instantaneous. The spin polarization rotates *around* the applied field resulting in a precessional motion shown if figure 3.5. The angular frequency ω of the precession of nuclear spin depends on the strength of the applied magnetic field B and is called the Larmor frequency given by equation 3.9.

$$\omega=\gamma B \qquad (3.9)$$

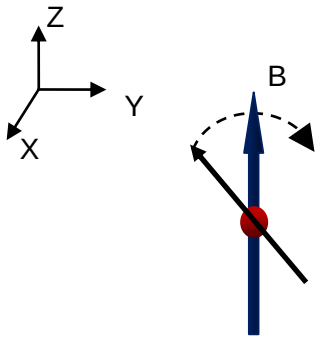

Figure 3.5: Precession of nucleus in external magnetic.

The net magnetic moment of the ensemble of nuclei give rise to macroscopic nuclear magnetism, which is basically the magnetic moment per unit volume, and can be termed as nuclear magnetization, M. This magnetization takes a finite amount of time to build up from zero when the external field is turned on. Assuming that the external field is pointing up along the z-axis, the longitudinal magnetisation M_z can be expressed by equation 3.10.

$$M_z = M_{0z} [1-\exp \{-(t-t_{on})/T1\}] \quad (3.10)$$

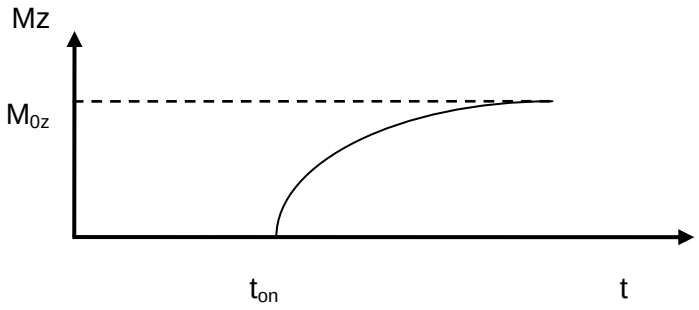

Figure 3.6: Build up of longitudinal nuclear magnetization.

In equation 3.10, t_{on} is the time when the magnetic field is turned on and T1 is called the longitudinal relaxation time constant. T1 is a characteristic time constant, specific to the sample molecules and gives the time in which the longitudinal magnetization builds up to 63 % of its maximum value.

In practice, external energy in the form of alternating electromagnetic field at Larmor frequency is applied to the system that can flip the longitudinal magnetization by 90^0 in the transverse or XY plane. Doing so shifts the net magnetization in the transverse plane and is likewise called transverse magnetization. When the alternating field is removed, the transverse magnetization continues to precess about the z axis, the direction of external magnetic field. The precession frequency is the same as the precession

frequency of individual spins, i.e. the Larmor frequency ω. The transverse components of the magnetization are expressed as

$$M_x = M_{0x} \sin(\omega t) \exp(-t/T2)$$

$$M_y = -M_{0y} \cos(\omega t) \exp(-t/T2) \qquad (3.11)$$

Figure 3.7: Decay of transverse magnetization.

In equation 3.11, T2 is another characteristic time constant specific to the sample describing the decay of the transverse magnetization and is known as the transverse relaxation time constant or spin-spin relaxation time constant. In general, T2 is many orders of magnitude shorter than T1.

3.5.4 Nuclear Magnetic Resonance (NMR)

The discussions in the preceding sections provide sufficient background for a brief introduction to NMR. This is necessary because of its prominence and ubiquity as a tool for chemical spectroscopy and medical imaging; and also due to its relevance to other forms of magnetic resonance.

NMR is concerned with detecting the decaying transverse magnetization that is picked up by an inductive coil perpendicular to the applied external static magnetic field. Assuming that the static magnetic field is along positive Z-axis, as shown in figure 3.8, the pickup coil is placed in the X-Y plane which is the transverse plane. As a general practice the sample is placed in a non-magnetic container such as borosilicate glass tube or plastic bottle and placed within the coil. When the RF electromagnetic energy of the correct frequency and power, is coupled into the sample by means of a tank circuit, of which the coil is a part, the nuclear magnetization is flipped from the longitudinal axis to the transverse plane resulting in the build up of the transverse magnetization. The decay of this magnetization, upon removal of the energy, results in a signal which is called the free induction decay (FID) signal, or the NMR signal and is picked up by the coil inductively.

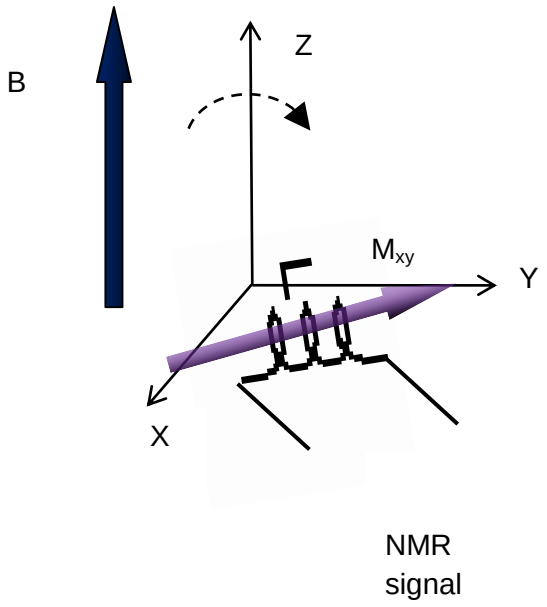

Figure 3.8: The induced NMR signal.

3.4.5 Magnetic resonance: A generic discussion

A broad approach to magnetic resonance is an interesting way of discussing the subject because of the common general principles. To start with, of course, magnetic resonance is found in systems possessing both magnetic moments and angular momentum.

If we consider a nucleus as an example with a spin I=1/2, there will be only two energy states shown in figure 3.9, with energy difference given by $\Delta E = \gamma \hbar B$. In order to detect the presence of the energy level, some form of energy spectral absorption should be observable. In order to drive the transition between the states, energy interaction is necessary and to satisfy the conservation of energy, such interaction should have angular momentum so that $\Delta E = \hbar \omega$. Clearly in order for the transition to take place, the energy gap has to be just satisfied which will lead to:

$$\Delta E = \gamma \hbar B = \hbar \omega \quad \Rightarrow \quad \omega = \gamma B$$

The above equation is the Larmor condition for resonance, an interesting result.

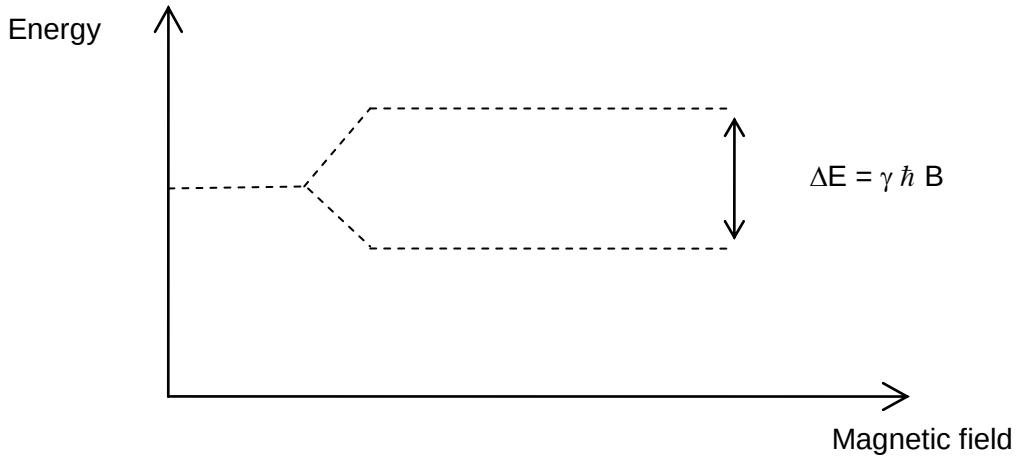

Figure 3.9 : Spin energy sublevels.

3.4.6 Nuclear Quadrupole Resonance (NQR)

The discussion so far has covered some of the fundamental concepts and principles of magnetic resonance. The underlying theory of NQR has also been briefly mentioned in the opening section. Figure 3.10 shows a non spherical nucleus in space with arbitrary orthogonal axes. The figure shows the non-spherical nucleus resulting from the compression of the spherical nucleus. The compression removes the positive charges in the two regions, marked – and transfers them to the regions, marked +. In the presence of electric field, each of the dipoles experiences equal and opposite torques, cancelling each other out and hence there is no net effect. However, in an EFG, the direction of which is shown in figure 3.10, the torque on the two dipoles are not the same and a net rotation due to the turning torque exists. This torque is proportional to the EFG and the amount by which the nucleus departs from spherical symmetry. The quadrupolar moment of the nucleus is given by

$$eQ=\int \rho(3z^2-r^2)d\tau \qquad (3.12)$$

Where ρ is the nuclear charge density, r is radius of the spherical charge distribution, τ is the volume element, -e is charge on the electron and Q is the quadrupolar moment. For spherical charge distribution this term vanishes because the average value of z^2 is equal to $r^2/3$. The Q has dimensions of r^2, i.e. cm^2.

The net turning torque, in the presence of EFG is proportional to the term $|e^2qQ|$, where q is the field gradient and is such that,- eq=dE/dz.

Since all quadrupolar nuclei also have angular momentum, the situation can be compared to the precessional model for NMR in an applied magnetic field, discussed in earlier sections where the nuclear moments precess about the direction of the applied magnetic field.

In NQR, by analogy, the nuclear quadrupole responds to the torque by precessing about the direction of maximum EFG with a frequency proportional to $|e^2qQ/h|$, where h is the Planck's constant. The important distinction between the electric case is that the frequency of precession depends on the orientation of the nucleus, where as in NMR the precessional frequency is independent of the orientations.

The nuclear precession has a nuclear angular momentum and hence a nuclear magnetic moment, producing a small magnetic field at right angles to the direction of the EFG, rotating in phase with the nuclear quadrupole at the same frequency.

The magnetic field, in phase with the nucleus, exchange energy with it and in classical terms, this is a resonance process occurring at a specific frequency, f_q (in Hz); the nuclear quadrupole resonance frequency. The resonance frequency f_q, of a quadrupolar nucleus in a given molecule directly depends on the EFG which, in turn, is very specific to the chemical structure. This makes it extremely unlikely to have the same NQR frequency for two different molecules. The chemical signature, in the form of the NQR frequency, for a quadrupolar nucleus in a particular molecule makes NQR an important tool for chemical detection and spectroscopy. More mathematically comprehensive details can be found in the text by Slichter and Smith [**65**] [**64**].

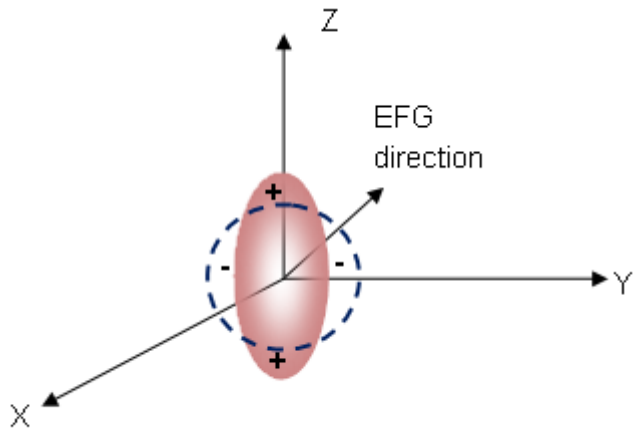

Figure 3.10: Nuclear electric quadrupolar moment.

3.6 Principle of electric field detection

We have mentioned on several occasion in this chapter the external electromagnetic energy and detection of the weak free induction decay signals. The propagation of electromagnetic waves can be explained by the set of equations proposed by Maxwell and therefore it is important to briefly mention it here. What is more important about these equations is the way they relate the electric and magnetic fields associated with such waves. The four Maxwell's equations are as follows:

$$\nabla \cdot \mathbf{E} = \rho/\varepsilon_0 \qquad (3.13a)$$

$$\nabla \cdot \mathbf{B} = 0 \qquad (3.13b)$$

$$\nabla \times \mathbf{E} = -\partial\mathbf{B}/\partial t \qquad (3.13c)$$

$$\nabla \times \mathbf{B} = \mu(J + \varepsilon\, \partial\mathbf{E}/\partial t) \qquad (3.13d)$$

Equations 3.13a and 3.13b are Gauss's law for electric charges and magnetic moments. Divergence of the electric field depends on the charge enclosed by the closed space. The divergence of magnetic field in a closed space is zero which suggests that magnetic monopoles do not exist or more precisely they exist only as dipoles with equal and opposite polarity.

Equation 3.13c suggests that the curl of an electric field produces time varying magnetic field, Faraday's law. The converse is also true, meaning a time varying magnetic field generates an electric field.

Equation 3.13d is modified Ampere's Law in which Maxwell proposed the addition of the time varying electric field.

As a qualitative discussion, the third law is of high relevance from the point of view of this thesis. This law states the co-existence of an electric field with a time varying magnetic field. The magnetic field component of a decaying

nuclear magnetization is conventionally detected using a pick up coil forming the basis of modern NMR systems. The intention of the work carried out as a part of this thesis is however, to demonstrate the direct measurement of the electric field associated with the magnetization using high impedance EPS. The electric field detection of an NQR signal of Sodium Chlorate at around 30 MHz is presented in this thesis. This work is inspired by previous work in which the electric field detection of NMR signal for Glycerine at 2 MHz was successfully demonstrated [**49**] [**19**]. Chapter two already discussed the principles of operation of EPS and the development as a part of work in this thesis.

3.7 The continuous wave (CW) experiment

3.7.1 The CW experiment: Inductive pickup

Figure 3.11 shows the complete block diagram of the experimental setup for a continuous wave NQR experiment. The aim of this experiment is to observe weak RF energy absorption by the sample when energy is coupled to the sample. The conventional way of conducting a CW experiment incorporates a tank circuit, which is essentially an inductor and capacitor combination. The sample is placed in the tank circuit which forms part of the marginal oscillator (MO). Generally, an MO is characterised by a high sensitivity to the RF energy losses and has the advantage that the operating frequency automatically follows the resonator frequency [**67**].The tank circuit frequency is swept in the region of the NQR frequency of the sample. This is achieved by incorporating a variable capacitor mechanism and in the present system achieved by using a varactor diode. The characteristic energy absorption by the sample at the NQR frequency, which is also the chemical signature of the sample, is detected by the MO. The output of the MO is generally an RF signal which is peak-detected, demodulated, amplified and subsequently filtered. The resulting audio frequency signal so obtained is displayed by means of a digital oscilloscope [**67**] [**68**]. Since the MO detects the change in the Q of the coil in the tank circuit, due to the absorption, this situation refers to an inductive pickup experiment.

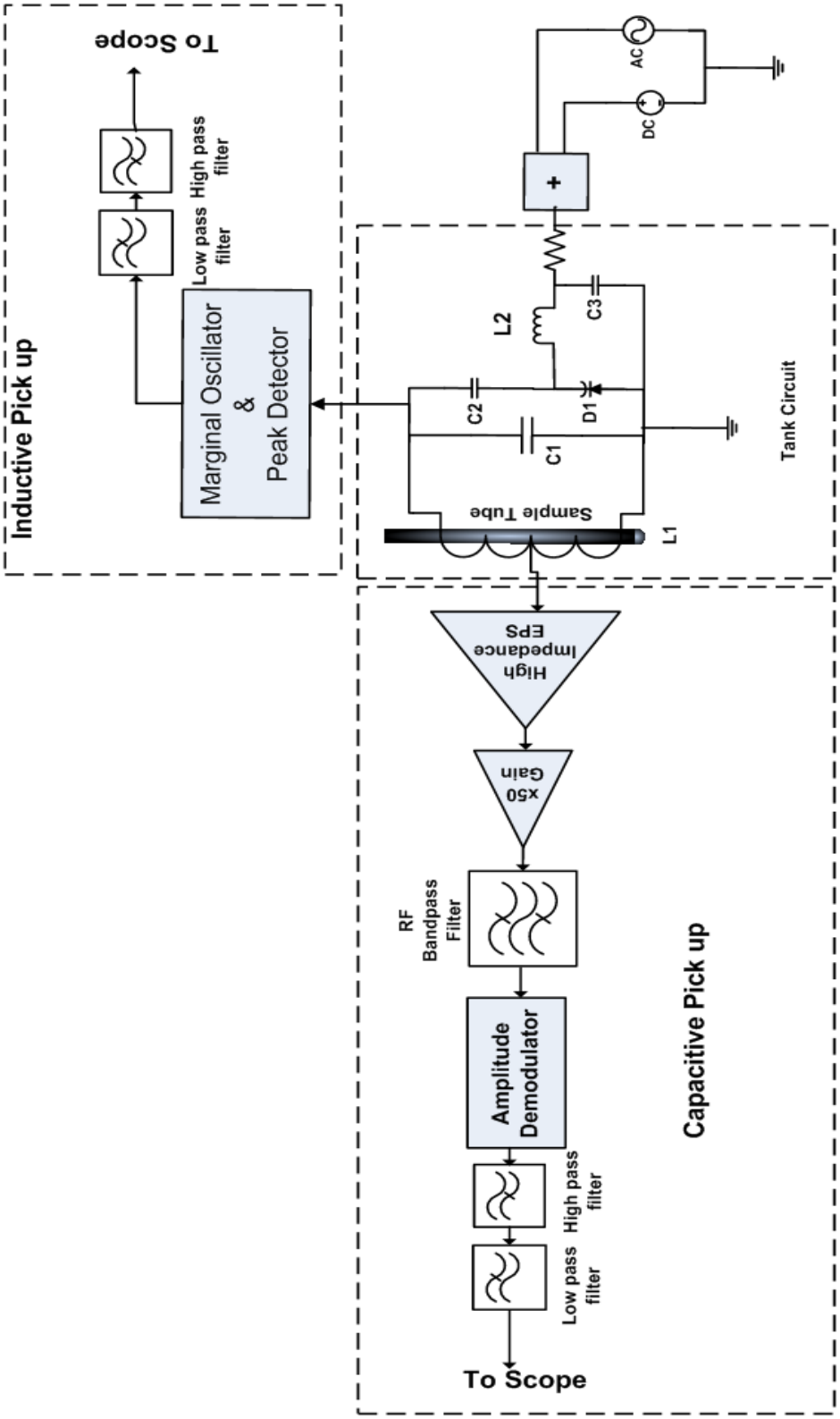

Figure 3.11: Block diagram of the continuous wave NQR experiment.

3.7.2 The sodium chlorate sample

Sodium chlorate ($NaClO_3$) has an NQR frequency of around 29.94 MHz. This obviously depends on external factors such as temperature, humidity and pressure and can form an interesting area of study [**69**]. For our experiments however, these parameters were assumed to be standard room temperature and standard atmospheric pressure.

$NaClO_3$ has a crystalline structure made up of Na^+ and ClO_3^- ions. The ClO_3^- ions form pyramids with chlorine atom at the apex. The Cl atom is covalently bonded with the oxygen atoms (ClO_3^-), while the bond between the metal ion, Na^+ is ionic. The EFG at the Cl site is mainly due to the charge distribution in the chlorate ions (ClO_3^-) and depends only slightly on the electrostatic interaction between the chlorate ion and the metal ions. The principal z-axis of the EFG lies along the threefold axis of the ClO_3^- pyramid [**69**].

The sample for this experiment was procured from Sigma Aldrich [**70**]. The sample purity is 99.0 % and it is an American Chemical Society (ACS) reagent which confirms its high chemical quality and suitability for laboratory usage [**71**]. It is in the form of a white crystalline powder and in use, it is kept in a 12 mm glass test tube sealed with solid wax to prevent ingress of moisture. In figure 3.11, the relevant section is labelled and the following sections discuss the details of some of the important functional blocks of the experiment.

3.7.3 The tank circuit

The tank circuit is basically a parallel combination of inductor L and capacitor C such that the resonance frequency is given by equation 3.14.

$$f = \frac{1}{2\pi\sqrt{LC}} \tag{3.14}$$

The inductor was made by using a four turn 19 Standard Wire Gauge (SWG) enamelled wire giving a total inductance of approximately 315 nH. This is represented by L1 in figure 3.11. The capacitor C1 and C2 are silver mica capacitors of values 82 pF and 22 pF, respectively. A variable capacitance or varactor diode BB809, D1 was also used in series with C2. The property of a varactor diode is that the junction capacitance is a function of the reverse voltage. The BB 809 is rated for a maximum continuous reverse voltage of 30 V. The diode junction capacitance varies between 4 pF to 39 pF corresponding to 28 V and 1 V, respectively [**72**].

Looking at the tank circuit section of figure 3.11, the diode capacitance D1 is in series with C2 and both of them are in parallel with C1. The series combination, Cs of D1 and C2 is given by equation (3.15).

$$Cs = \frac{D1.C2}{D1+C2} \tag{3.15}$$

The total capacitance contributing to the resonant frequency, C_{tot} of the tank circuit is of course the parallel combination of Cs and C2 which is given by equation (3.16).

$$C_{tot} = C1 + Cs$$

$$\text{Or} \qquad C_{tot} = C1 + \frac{D1.C2}{D1+C2} \tag{3.16}$$

The tank circuit is placed inside a custom made aluminium box. This provides an electromagnetic shield which serves in two ways. The shield contains the electromagnetic energy at the tuned frequency inside and stops it from

radiating. It also keeps electromagnetic radiation from other sources outside and in this way it reduces interference**.**

3.7.4 The marginal oscillator

Regenerative or marginal oscillators are often used in continuous wave magnetic resonance experiments. There are many reported in literature [**67**] [**73**] [**74**]. Generally FETs are used because of their high input impedance. Bipolar Junction Transistors (BJTs) were used in the early days but they used to load the resonating tank circuit because of their relatively low input impedance. Both Offen [**73**] and Soticon [**67**] use FET stages in their designs. A FET differential amplifier stage is used by Soticon [**67**] with additional circuitry for amplitude demodulation and a frequency meter. The input of the differential amplifier is fed to the tank circuit. In principle, the MO stage is very sensitive to the changes in the Q of the tank circuit. The Q of the tank circuit is reduced at the characteristic frequency where the sample absorbs the RF energy coupled through the inductor and this is picked up by the MO. This output is amplitude demodulated to an audio frequency signal and some gain is added by means of an audio frequency amplifier.

A commercially available NMR experiment kit by Leybold Didactic [**75**] was used as the MO stage for the CW experiment. The kit also provides a low frequency output. In the actual experiment the tank circuit is connected to the MO input. The DC voltage is adjusted to change the diode capacitance D1 which changes the tank circuit frequency. An AC voltage is added to the DC level which sweeps the voltage across the variable capacitance diode and hence the resonant frequency. At the NQR frequency the sample absorbs small amount of RF energy and a dip in the Q results at the frequency of interest.

3.8 The CW experiment using electric field sensing

3.8.1 The CW experiment: Capacitive pickup

The main functional blocks of the experiment, depicted in figure 3.11 are discussed in the previous sections. The ultra high impedance EPS is discussed in great detail in chapter two. As seen in figure 3.11, there are both inductive and capacitive pickup arrangements incorporated in the experiment. Obviously, the names of such pick up arrangements follow from the way the signal is being picked up.

The inductive pickup is done by detecting the signal by means of the tank circuit coil. This is the simplest way of doing such an experiment. The results obtained in this manner can be used to confirm the acquisition of the NQR signal when further complexity will be added to demonstrate capacitive pickup, discussed below.

In order to perform NQR by capacitive pickup we use the high impedance EPS and this is where we demonstrate the signal acquisition in a non-conventional way. This approach has been performed by A.Aydin et.al [**49**] [**19**] [**20**] for NMR of glycerine at 2 MHz. Gregorovic et al [**32**] reports a pulsed NQR experiment of sodium chlorate, although they use a capacitor to excite the signal. The pulsed NQR experiment is described later in the thesis.

As seen in the capacitive pickup section of the experiment, labelled in figure 3.11, the EPS is capacitively coupled to the sample in the tank circuit coil. It is important to describe the manner in which this has been achieved.

An electrode was constructed using UT-34 semi rigid coaxial cable. The outer and inner diameters of the cable are approximately 0.86 mm and 0.2 mm, respectively. The dielectric material is PTFE and the conductors are copper. The cable has a characteristic impedance of 50 Ω and has a capacitance of 95.1 pF/meter [**76**]. Approximately 40 mm of the cable was cut and one end of it was mounted on a standard male SMA connector. This length corresponds to approximately 3.8 pF. The other end of the cable was cut in such a way that the

inner conductor protrudes so that it can be used to sense the signal to be measured.

The electrode is inserted through a hole made on the side of the aluminium box containing the tank circuit and the sample, on to the wall of the glass tube containing the sample. This situation is roughly depicted in figure 3.14. A rectangular piece of gold foil can be seen on the wall of the glass tube containing the sample. This is used in order to increase the capacitance between the electrode and the sample which increases the amount of signal coupled to the EPS. Caution must be exercised when deciding the dimension of the gold foil because the capacitance increases with the area. The EPS can run into saturation if the signal is coupled to the sensor too strongly. Clearly this is something that the experimenter has to be aware of and depends on other parameters such as the gain in the EPS circuitry.

The electrode is connected to the high impedance EPS. The output of the EPS is an RF signal which is filtered through a high Q, RF band pass filter tuned at approximately the same frequency as the tank circuit. This signal is subsequently demodulated using the SA 602 based amplitude demodulator, described in the next section. The resulting audio frequency signal is filtered before displaying on a digital oscilloscope.

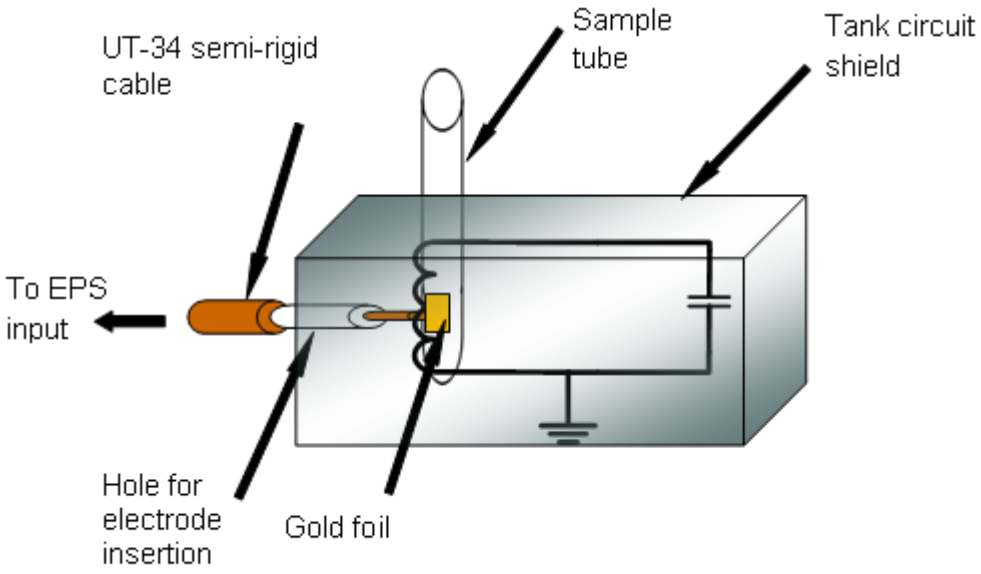

Figure 3.12: EPS coupling arrangement

3.8.2 Amplitude demodulator

A double balance mixer, SA 602 [**77**] was used to build an amplitude demodulator. The SA 602 is a Very High Frequency (VHF) monolithic double balanced mixer with input amplifier, on board oscillator and voltage amplifier. As shown in figure 3.12, one of the inputs is grounded and other input is used to feed the RF input which comes from the high impedance EPS. The same RF input is fed to one of the oscillator pins. This arrangement is similar to a typical homodyne mixer and the outputs of the mixer, which are also the outputs of SA 602, are fed to an audio frequency amplifier, which in this case has been designed with an OP 27 in differential mode. This unit was designed to be operated by a battery powered rack module. To do this a number of voltage regulators were used to regulate the battery voltage of ± 24 V down to different DC voltage rails. The following were the DC requirements by the different parts:

SA 602	:+6 V
OP 27	: ± 15 V
EPS	: ± 5 V

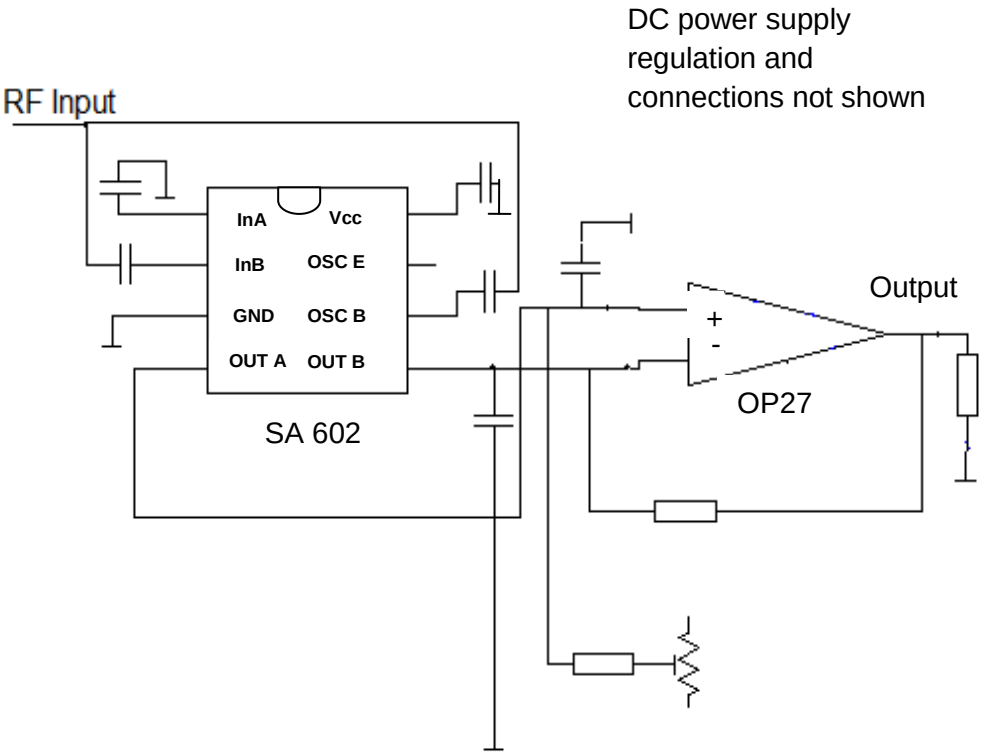

Figure 3.13 Amplitude demodulator using SA 602

This module was tested for minimum detectable signal. In order to test this circuit a Rhode & Schwartz SMB 100A signal generator was used as the RF source with a frequency range of 9 KHz to 3.2 GHz and internal modulation facilities [**78**]. It is also GPIB controllable which makes it remotely configurable. A test setup was built with the settings given in table 3.1.

Internal modulation scheme	Amplitude Modulation (AM)
AM source	Internal
AM depth	100%
LFGenFreq[1]	1 KHz
LFGenShape[2]	Square
RF	ON

Table 3.1: Signal generator setting for testing the amplitude demodulator

This setting produces an amplitude modulated RF carrier which is internally modulated by a 1 KHz square wave. This modulated RF signal was fed to the input of the SA 602 based amplitude demodulator module in order for it to output the low frequency square wave. A LabVIEW Virtual Instrument (VI) was built to sweep the RF carrier from 1 MHz to 1 GHz for different levels of RF carrier. The aim was to check whether the SA 602 based amplitude demodulator module can detect the low frequency signal for progressively decreasing levels of RF carrier. The result obtained by this system is shown in figure 3.14. It is clear from this result that the module can be used to demodulate for carriers up to 200 MHz after which it produces a resonance followed by a limitation of bandwidth beyond 500 MHz. The resonance may be eliminated by using a matching circuit at those frequencies if needed be but since the frequency for which it is intended to be used is around 30 MHz, this is not required. It is also clear that the signal can be detected with an RF level

[1] LFGenFreq =Low Frequency Generator Frequency
[2] LFGenShape= Low Frequency Generator Shape

down to – 50 dBm on a 50 Ω system which corresponds to a voltage level of 0.71 mV or 10 nanowatts. Obviously this is a rough estimate but nevertheless, it makes it clear that this is suitable for the purpose it is designed for.

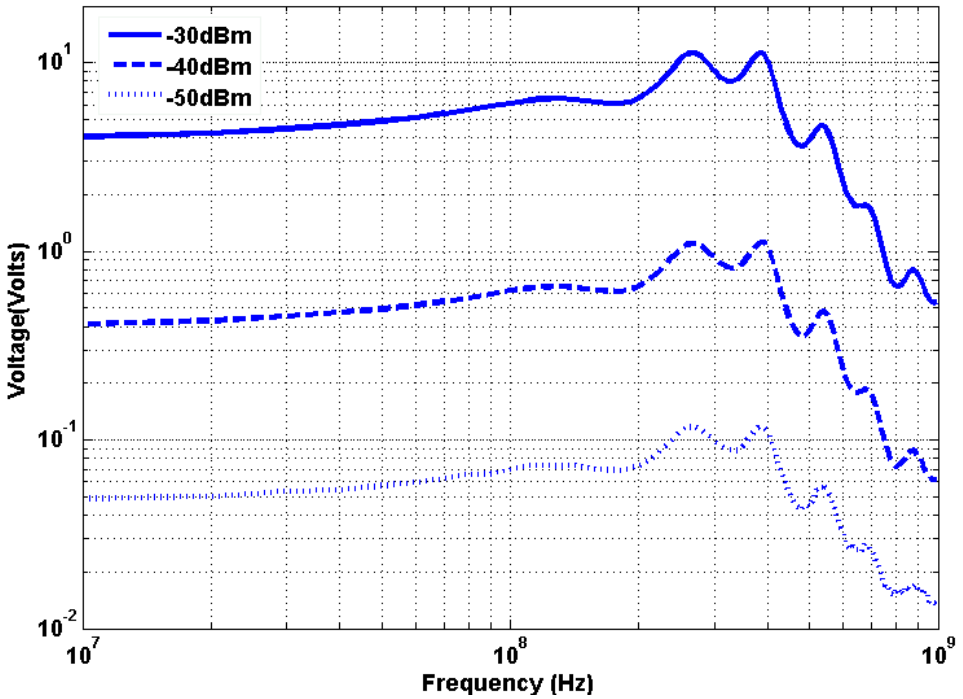

Figure 3.14 : SA 602 based amplitude demodulator test

3.9 Results

Having discussed the two approaches for acquiring the signal, this section shows the results obtained for a sodium chlorate sample at approximately 29.94 MHz. In order to observe weak RF energy absorption due to NQR it is extremely important that the sample be excited by the exactly the right frequency. Therefore the resonant frequency of the tank circuit is a critical parameter and required to be controlled with precision. The variable capacitance diode incorporated in the tank circuit design plays an important role. To obtain the signals shown in figure 3.14, the DC voltage applied across the diode was 8.65 V which corresponds to a diode capacitance of 14 pF.

From equation 3.16, C_{tot} = 90.8 pF. Since the inductance of the coil was 311.5 nH, this sets the resonant frequency of the tank circuit at 29.92 MHz.

The two signals so obtained are essentially identical, demonstrating a simultaneous acquisition by both inductive and capacitive methods. The small sinusoidal AC voltage was added to the DC voltage to sweep the region of the NQR frequency in order for the signal to be detectable. The sinusoidal traces shown in figure 3.15 show this AC sweep added to the varactor bias voltage. The sinusoidal sweeping bias voltage of the varactor diode results in a small sweep in the resonant frequency of the tank circuit and this is a critical region in which to expect the observation of the NQR absorption.

Figure 3.15 is the data obtained by using the acquisition feature of the Tektronix oscilloscope and represent 25000 samples. The data is averaged 16 times to reduce noise. The varactor diode capacitance is varying between 14.8 pF and 14 pF corresponding to the peak and trough of the sinusoidal bias signal resulting in the tank circuit frequency sweep in the interval of 29.918 MHz to 29.975 MHz. Clearly, this interval incorporates the expected frequency at which NQR of Sodium Chlorate can be observed. Two NQR absorptions per cycle can be seen, one during the positive sweep and the other during the negative.

The NQR signal shows a characteristic RF energy absorption. In the experiment, this RF is demodulated and subsequently high pass and low pass

filtered. The effect of this high pass filtering produces a differentiated signal which is what we see in the results in figure 3.15. A zoomed in section of one of the absorption features is shown in figure 3.15 (c).A rough estimate of the line width of an NQR signal can be roughly done with the data at hand. The frequency difference between the peak and troughs of the sinusoidal trace is 57 KHz (29.918 MHz -29.975 MHz). Assuming this to be linearly spaced along X-axis of the plot yields an approximate line width of the NQR blip shown in figure 3.15 (c) to be 1.38 KHz.

In order to ensure that the signal was actually due to the NQR resonance, the sample tube was pulled out of the coil which resulted in the signal disappearing. The signal reappeared when the sample was replaced.

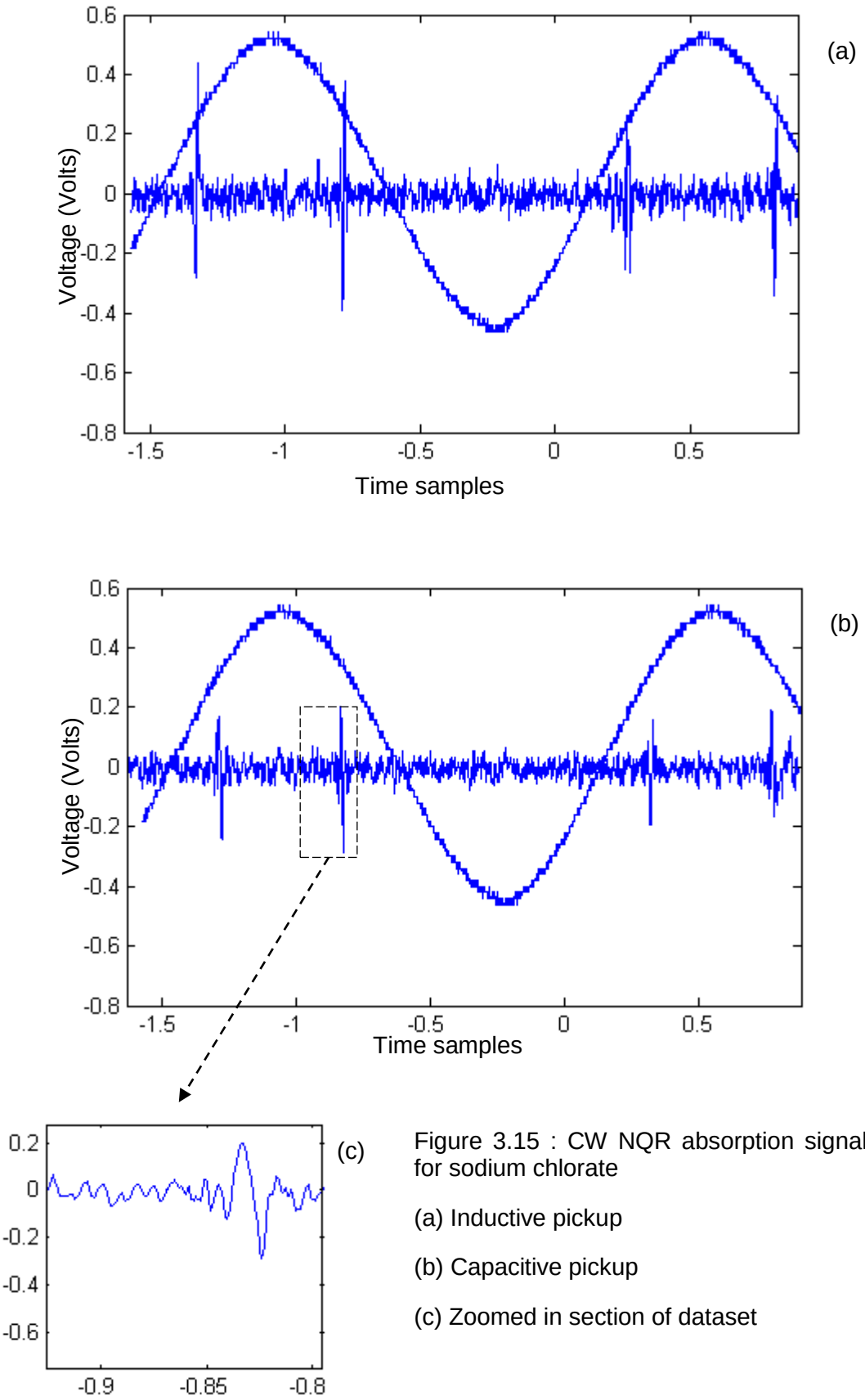

Figure 3.15 : CW NQR absorption signal for sodium chlorate

(a) Inductive pickup

(b) Capacitive pickup

(c) Zoomed in section of dataset

Chapter 4

Pulsed Nuclear Quadrupole Resonance

4.1 Introduction

Modern day magnetic resonance experiments are based on a pulse technique. Unlike the continuous wave experiment where the excitation frequency is varied in the region of the resonant frequency to observe the characteristic absorption of the signal, in the pulsed technique the frequency for exciting the sample is kept constant and instead of continuously perturbing the sample, RF bursts are used which are confined in time. As discussed in chapter 1, highly sophisticated pulse sequences have been studied and tried on a range of different samples, both in laboratory settings and in the field, which have resulted in improvement in signal to noise ratio and reduction in false alarms.

In this chapter, we describe a pulsed experiment for a sodium chlorate sample at around 30 MHz. Major parts, electronic hardware and software, required to set up the experiment, were designed and built as a part of this project and they form the subject of discussion in this chapter. Having demonstrated in chapter three, the continuous wave experiment for the acquisition of the Cl^{35} NQR signal in $NaClO_3$ by inductive as well as capacitive pick up, this chapter is about achieving the same goals for a pulsed method with more stress given in confirming the electric field component of the signal through relevant experimental trials.

4.2 The pulsed NQR experiment

Figure 4.1 shows the entire experimental setup of the pulsed NQR experiment. It incorporates means to conduct the experiment conventionally as well as by using the high impedance EPS. This diagram will be referred to as and when necessary during the later part of this section while discussing the constituent blocks.

The conventional method uses a coil to pick up the magnetic component of the signal, whereas using the high impedance EPS, we demonstrate the electric field acquisition of the signal. Having demonstrated the same in the continuous wave experiment in chapter three, we describe the pulsed NQR experiment in this chapter.

In the pulsed experiment, we flip the magnetization vector to the transverse plane by applying a pulse of RF energy at the correct frequency and observe the signal resulting from the precession of the magnetization about the spin polarization axis or the direction of maximum EFG. The block diagram shows the necessary parts of the experiment that we have used to achieve this. We will describe the key elements of the experiment in the following sections of the chapter followed by the results obtained. It is important to mention briefly at this stage, that we used LabVIEW and a National Instrument USB-5133, 100 MSample/sec, 2-channel digitizer [**79**] to acquire the signal.

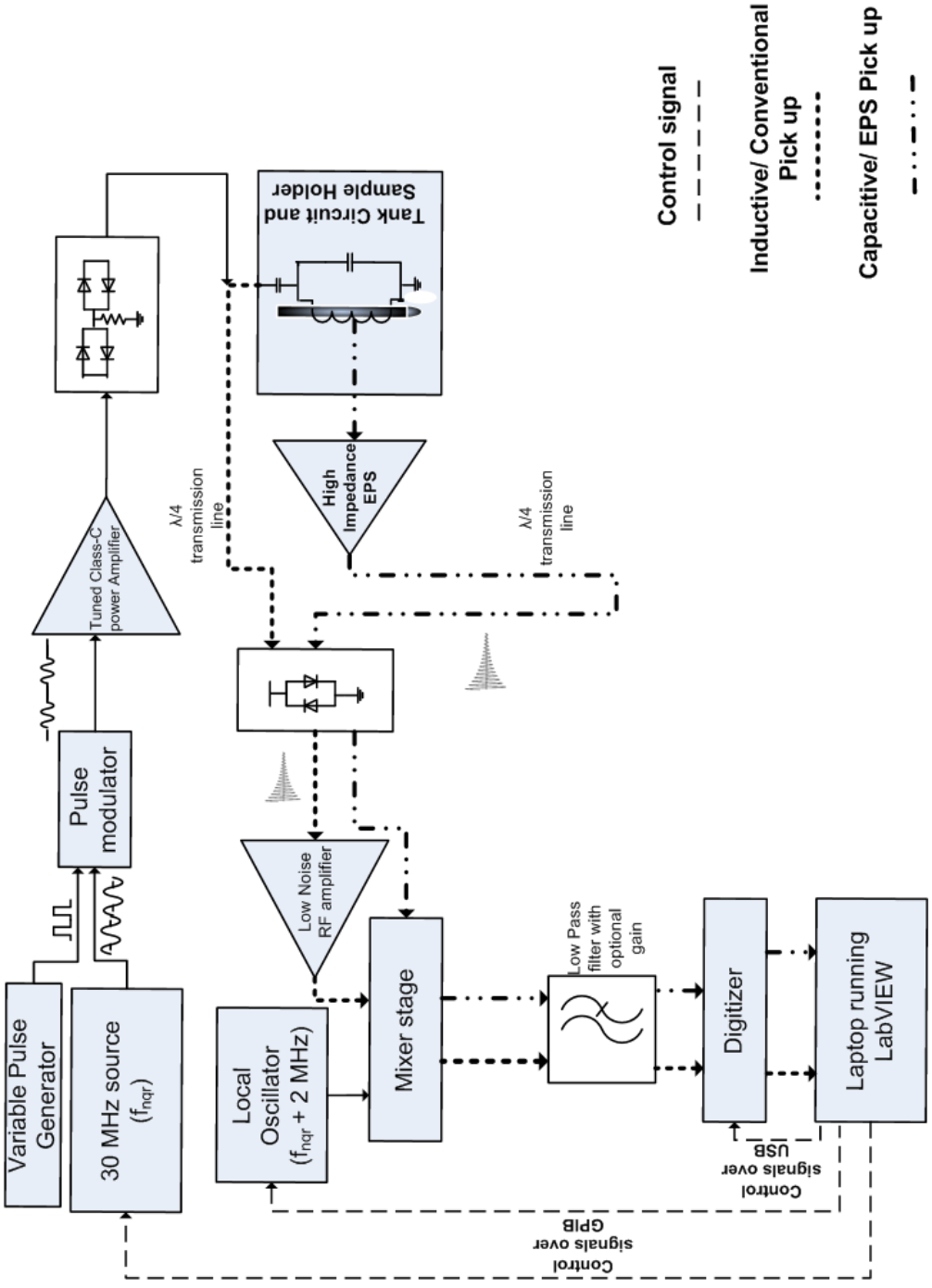

Figure 4.1: Block diagram of the pulsed NQR experiment

NQR is a very sensitive technique and can be observed only if all the parameters required to give rise to the resonance are correct. This includes the right frequency, power level, temperature, pressure and humidity. In our experiment, we assumed the environmental factors to be standard, i.e. room temperature and standard atmospheric pressure. The sample was put in a glass test tube which was properly sealed with wax in order to protect the sample from attracting humidity which $NaClO_3$ does due to its hygroscopic nature.

The LabVIEW Virtual Instrument (VI) that we developed incorporated controls for varying the power level and the frequency of the signal by remotely controlling the signal generators and data acquisition system which allowed the data to be saved with unique file names in the designated folder on a Windows laptop.

4.2.1 The gated RF system

The generation of pulses of the correct number, widths and repetition is crucial to the transmitter section of a pulsed NQR system. The pulses gate the RF carrier that in turn, after amplification, excites the sample placed in the tank circuit. It is subject to experiment as to how much power is necessary to flip the bulk magnetization by a certain degree from the spin polarization axis, for it to precess back to the equilibrium position releasing the detectable signal at the receiver end. Therefore provision for having a selection of pulse widths and repetition rate was incorporated in the design to allow the experimenter to decide the optimum combination during the actual experiment.

The schematic diagram for the pulse gate circuit is shown in figure 4.2. This circuit is a modified version of the pulse gate circuit in the Kirsch and Newman paper [**80**]. The merit of this circuit is that it uses easy to obtain 555 timers [**81**] and standard digital logic gate ICs [**82**] [**83**] and is therefore easy to implement. While there are other ways to implement pulse generation circuits using microcontrollers and FPGAs with computer interface, allowing generation of

complicated pulse sequences, they can amount to individual projects on their own right.

In this case however, we are interested in building all necessary parts of a relatively involved project and choose the simplest implementation which meets the requirement of the experiment. The circuit operation is as follows: The IC1 to IC6 represent six 555 timers. IC1 is configured in astable multivibrator mode which generates square wave pulses and is representative of the repetition rate. The falling edge of the repetition pulses generated by IC1 trigger IC2, configured as a monostable multivibrator. The falling edge of the pulses from IC2 triggers IC3 and IC4 simultaneously giving two separate square pulses. IC3 triggers IC5 which is a monostable timer. IC4 and IC5 outputs are combined using a 2-input OR gate giving two pulses with variable pulse width, gap width and repetition rates. The pair of pulses are the transmit pulses which are going to be used to gate the CW RF. The control for varying the pulse widths is achieved by the timing resistor in each 555 timer block where we used a rotary wafer switch with ten positions, each with a fixed resistor value, giving ten different time constants. In figure 4.2, these resistors are shown in square boxes. As can be seen, this circuit can produce up to two pulses, although IC4 can be turned off to make it produce only one pulse. Provision was also made to generate some auxiliary pulses, named Q and inverted Q pulse in case we need them during the experiment. The Q pulse was produced by using monostable IC6 being triggered by the pair of transmit pulses. Inverted Q was simply generated by a logic inverter. Table 4.1 shows all the pulses that this circuit can produce.

Repetition rate (IC1 output)	Width of pulse 1 (IC5 output)	Width of the gap between pulse 1 and pulse 2 (IC 3 output)	Width of pulse 2 (IC4 output)
10 ms	1 μs	1 ms	OFF
14 ms	2 μs	5 ms	
22 ms	4 μs	9.5 ms	
30 ms	8.5 μs	20 ms	5 μs
40 ms	10.5 μs	30 ms	9 μs
55 ms	16 μs	42 ms	11 μs
60 ms	24 μs	54 ms	16 μs
75 ms	36 μs	65 ms	24 μs
105 ms	42 μs	80 ms	36 μs
130 ms	52 μs	95 ms	42 μs

Table 4.2 : Different pulses that the pulse gate generator can produce

In order to generate gated RF pulses it was necessary to have a pulse modulator. To implement this system we used a commercially available signal generator. The R & S SMB 100A has internal amplitude, frequency and phase modulation option with choice of internal as well as external source [**78**]. This amplitude modulation option facility was optimised for pulse modulation by selecting 100 % modulation depth and setting the source to be external so that the pulses from the pulse gate circuit could be used. This arrangement allowed the continuous output of the signal generator to be pulse modulated by the external pulse. It was ensured that the duty cycle is extremely small (maximum 50 μs pulse with minimum 10 ms repetition rate), for the reasons stated later.

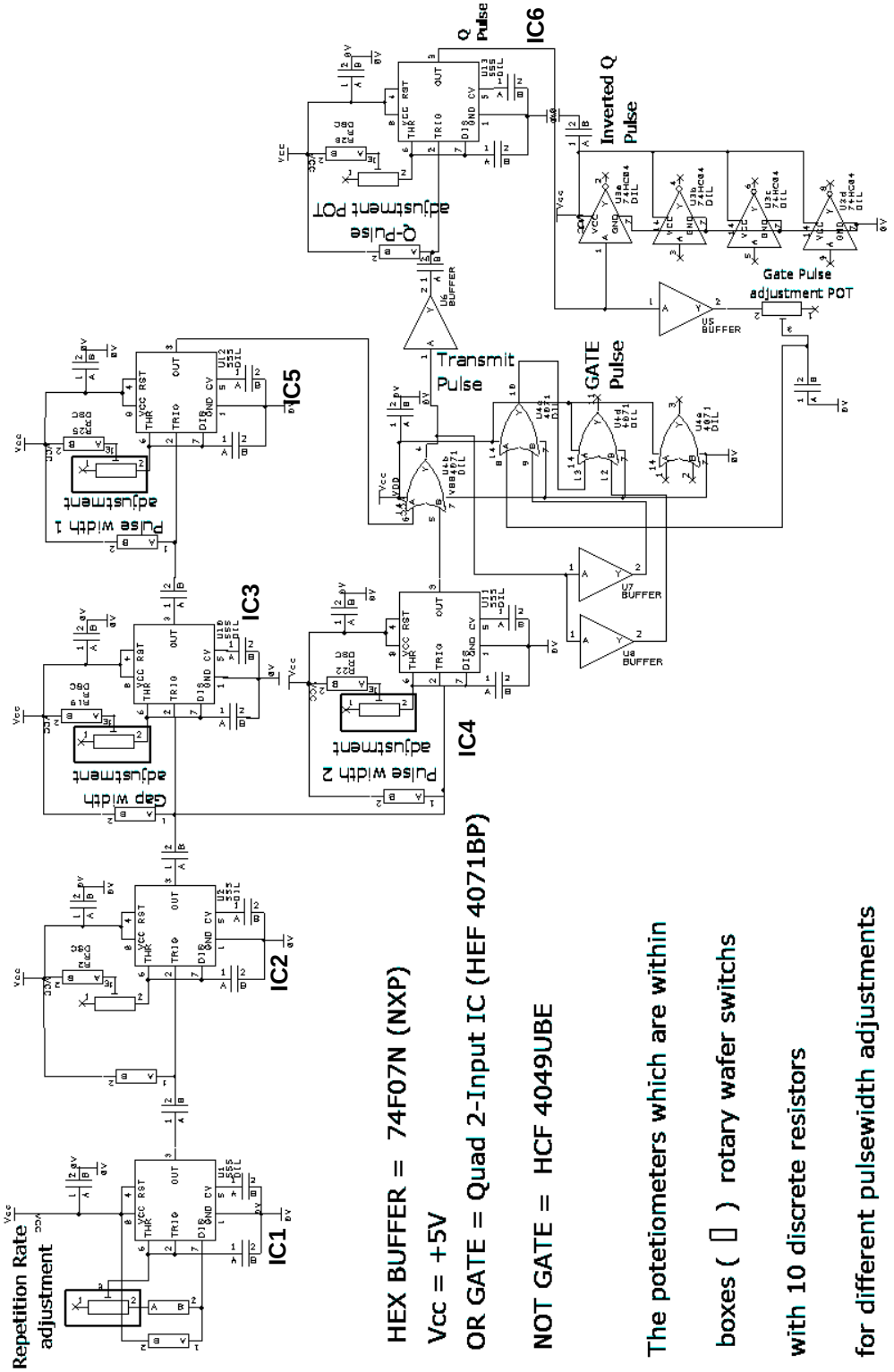

Figure 4.2 : Schematic diagram of Pulse gate circuit

4.2.2 Power amplifier

A power amplifier is necessary to increase the amplitude of the pulses before they are fed to the tank circuit which holds the sample in the test tube. The circuit diagram used to build a class-C power amplifier is shown in figure 4.3. A power MOSFET IRF 830 was used as the power device which is rated for 500 V with a low on-state resistance of 1.5 Ω [**84**]. This is a tuned circuit where the tuning is achieved by the capacitor C2 and the inductor L1. As seen in the diagram, C2 is a variable capacitor with a range of 6 pF to 200 pF. This is an air gap capacitor with high power rating and a mechanically controllable metal shaft and semicircular co-axial metal plates. The inductor is also an air gap coil constructed manually by winding SWG 19 enamelled wire which gives it a high voltage rating which is necessary because of its direct connection to the high voltage power supply and the high voltage RF output developed by the circuit.

The capacitor C1 is used to AC couple the gated RF pulse at the input of the amplifier. A bias network was employed to maintain reliable switching of the MOSFET with L2 providing a high impedance path to the RF at the input. During the pulse, the MOSFET conducts fully and the tuned circuit provides a low impedance path, drawing current from the high voltage DC power supply and so amplifying the RF pulse.

This circuit was tested with the pulse gate circuit and R & S SMB 100A signal generator and a dummy 50 Ω load. The output of the signal generator which is set to generate pulsed RF was fed to the amplifier input and the output was terminated with a high wattage, 50 Ω resistive dummy load, giving a maximum power output of 25 Watts with the highest power setting of the signal source. The power amplifier and the pulse gate generator circuits were housed in a metal box, together with the custom designed mains power supply to provide the necessary DC rails. The actual arrangement is visually shown in Appendix C.

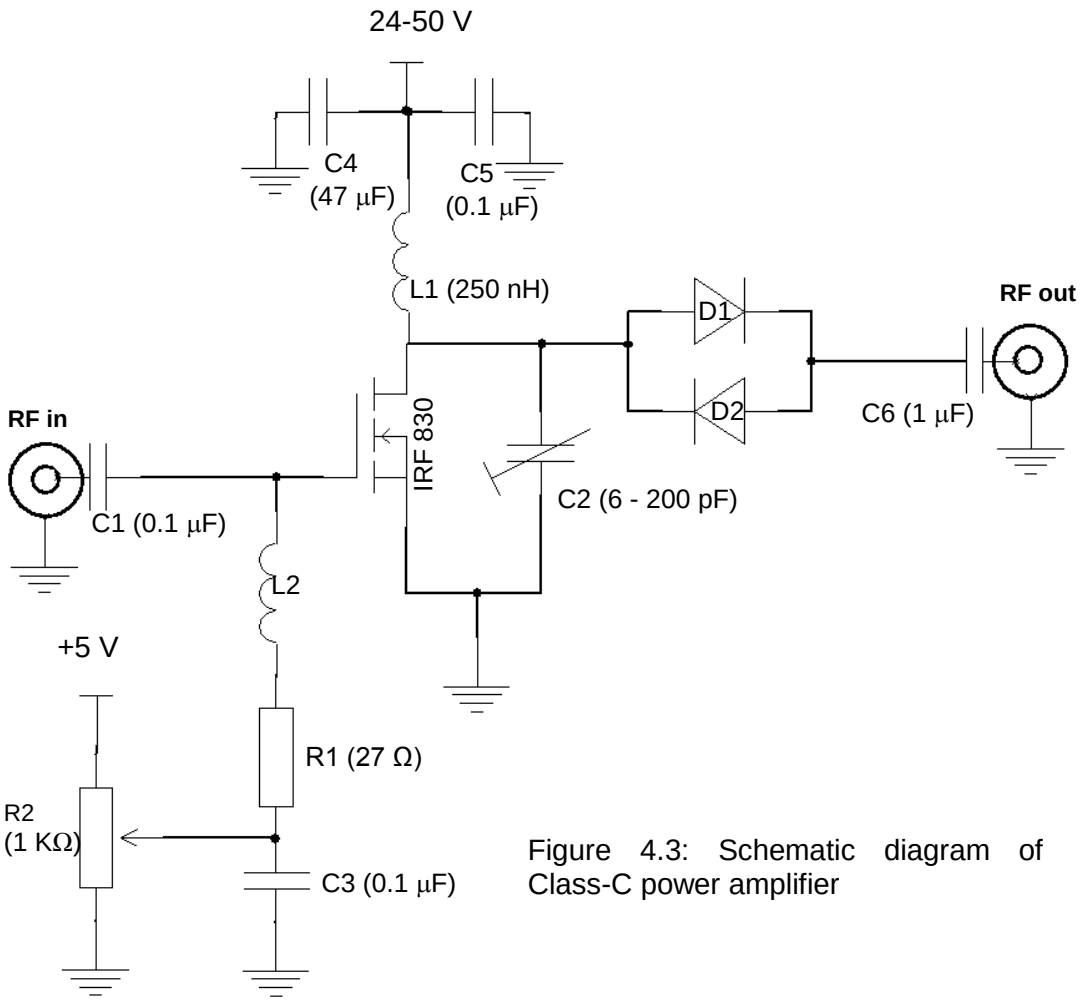

Figure 4.3: Schematic diagram of Class-C power amplifier

The crossed diode arrangement is a common method of providing RF isolation between the power amplifier output and the load which provides protection to the amplifier stage.

Crossed diode designs have effectively been used in experiments and is reported by Lowe and Tarr [**85**] which describes a pulsed NMR system at 30 MHz. The diodes D1 and D2 in figure 4.3 use the non-linear properties of the semiconductor diodes making them very high impedance for voltages less than approximately 0.6 V and highly conductive above this level. During the high power pulses they conduct heavily allowing the pulses to transmit into the next block in the signal chain shown in figure 4.1 and act as an open circuit

between the pulses, isolating the transmitter from the receiver. A high voltage, low loss silver mica capacitor, C6 was used to act as a DC blocking capacitor.

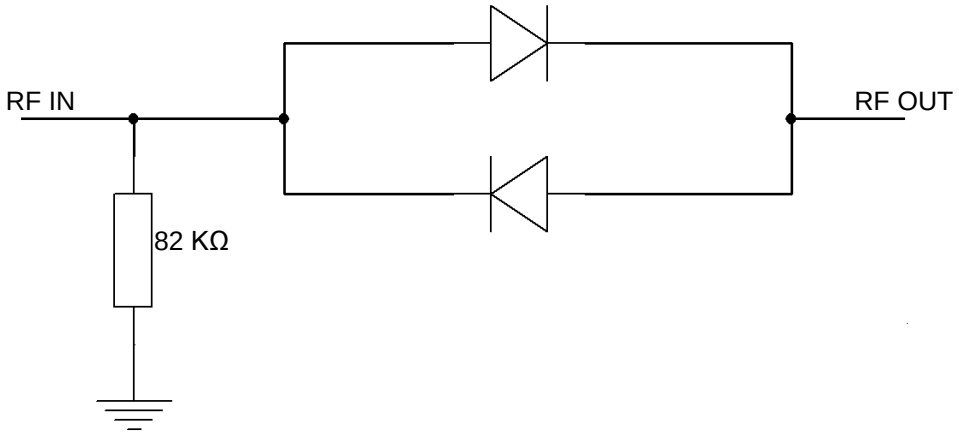

Figure 4.4: Crossed diode extender

In addition to this, another crossed diode arrangement was used at the output of the power amplifier. The arrangement is shown in figure 4.4. Griffin [**86**] documents this circuit in his low frequency NMR experiment and Aydin used this in his DPhil thesis work [**49**]. Basically, this arrangement provides additional protection to the system. It provides a low impedance path to the RF pulses during the transmission between the output of the power amplifier to the tank circuit. Between the pulses, the noise of the power amplifier being below the turn on voltage of the diodes, make them open circuit isolating the transmitter.

4.2.3 The tank circuit

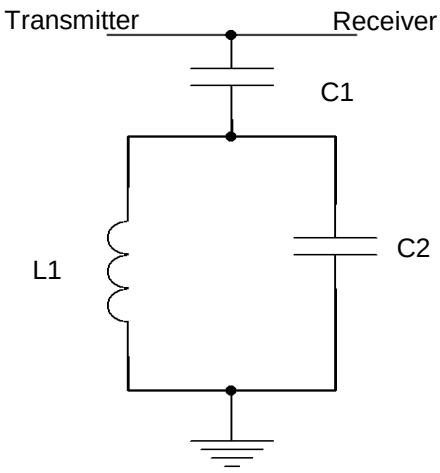

Figure 4.5: Tank circuit for pulsed experiment

The tank circuit used for this experiment is shown in figure 4.5. The inductor L1, built by winding SWG 19 enamelled wire with a value of approximately 340 nH and the capacitor C2, an 82 pF low loss silver mica capacitor rated for high voltage determine the resonant frequency of the system. The capacitor C1, also a silver mica capacitor, is used as a matching capacitor for optimal coupling of RF power into the tank circuit. The value of this capacitor is somewhat experimental and mainly a compromise between too much loading of the circuit and too little causing loss of the RF power.

The $NaClO_3$ sample is put in a glass tube of 12 mm diameter which is a tight fit into the inductor of the tank circuit. As seen from the diagram, the same port is used for both coupling the energy into the circuit as to receive it. This arrangement makes it a simple and convenient system. However, in order to reliably operate this, careful design is very important. During the transmit mode when the high power RF pulses are coupled into the circuit and the tank circuit resonates with a high Q, the receiver side should be completely isolated from

the transmitter, acting as open circuit. The next section discusses the way this is achieved. As soon as the pulse is over, the transmit end of the port becomes high impedance stopping the RF travelling back whereas the receiver end becomes low impedance. The previous section already explains how we do this.

4.2.4 The crossed diode and the quarter-wave line

The crossed diodes at the input of the receiver preamp acts as shunting path for the high power pulses so that they don't go through the amplifier causing damage. In the experiment this was implemented by putting the crossed diode pairs an inside in-line BNC socket, schematically shown in figure 4.6. This technique, together with the quarter-wave line, has been used by many in NMR/NQR experiments. The quarter wave line acts as an impedance transformer. The impedance relationship is given by equation 4.1.

$$Z_{input} = \frac{Z_0^2}{Z_{output}} \qquad (4.1)$$

Here Z_{input} is the impedance at the tank circuit end and Z_{output} is the impedance at the preamplifier end. Z_0 is the characteristic impedance of the BNC cable which is 50 Ω. During the pulses when the crossed diodes down to ground are acting as a short i.e Z_{output} =0, the input impedance , Z_{input} is infinite making the receiver side of the experiment act as an open circuit, isolating it from the transmitter side.

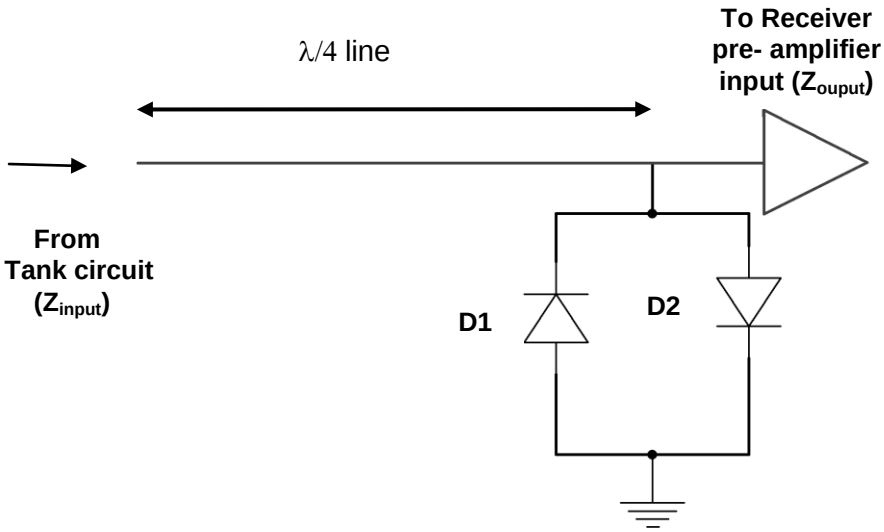

Figure 4.6 : Quarter wave line and crossed diode at receiver front end

4.2.5 The superhetrodyne receiver system

In this experiment, we have employed a standard superhetrodyne receiver system in both conventional as well as EPS acquisition. In the conventional setup the signal is acquired by the pickup coil of the tank circuit and to acquire the electric field component, the high impedance EPS, discussed in chapter 2 is used which is capacitively coupled to the sample in a manner described in section 3.8.

In order to implement the superhetrodyne system, a local oscillator is required in addition to the main source of frequency which is provided by the R&S SMB 100A. The local oscillator frequency is provided by another signal generator, a

Thurlby Thander Instruments (TTI) TGR 1040 1 GHz synthesised signal generator [**87**]. Both these sources have GPIB ports which allows them to be simultaneously accessed remotely using LabVIEW. LabVIEW drivers were required to establish this remote connection. The detail of the LabVIEW VI is important and will be discussed further down to avoid digression.

The signal received from the tank circuit was mixed with the CW signal from TGR 1040 by using a commercial double balanced mixer [**88**]. The difference frequency between the drive frequency and the local oscillator was maintained at a fixed value of 1 MHz. The output of the mixer which gives both sum and difference of the mixing signal frequencies was low pass filtered to get rid of the sum frequency so that the only signal to be measured was the 1 MHz difference frequency. This makes the acquisition easily achievable. This relatively low frequency signal was fed to one channel of the USB-5133 digitizer to send the data digitally over USB to the laptop running the LabVIEW VI.

4.2.6 The data acquisition system

Having set the experiment, it was necessary to reliably collect data and save it for future retrieval. The NQR signal for $NaClO_3$, as like for any other molecule, is very specific and is subject the right width of pulse and the power level of the pulse that is being used to perturb the sample. To ensure that the signal obtained at the characteristic drive frequency is actually the signal of interest, we integrated the mechanism of repeating the experiment at a range of drive frequencies in the vicinity of the resonance, at different power levels and also with and without the sample in the tank circuit. In order to implement the variation of frequency and power parameters, we included options to manually as well as automatically change these parameters in the LabVIEW VI. This was possible because the sources used in the experiment had GPIB interfaces and also a GPIB to USB converter cable was available which made it convenient to establish connection between the equipment and the computer. A LabVIEW VI was developed which allowed the user to remotely change the parameters of the signal generator.

The local oscillator frequency was maintained at a fixed offset of 1 MHz so that when the drive frequency was varied the local oscillator frequency followed it with a 1 MHz offset. This allowed us to use the superhetrodyne reception at all frequencies that we conducted the experiments at.

As the signal became available, whether NQR or not, it was averaged 100 times to reduce the noise. The averaged signal was saved in a designated folder on the computer with a unique filename.

4.3 Results and discussion

It should be clear from the discussion until now that most electronics for this experiment was designed as a part of the project. After setting up the experiment with all the necessary electronics, the LabVIEW VI was executed to acquire signals with various parameter combinations to establish that the correct NQR signal had been detected. Considering there are a number of unknown parameters, the most logical way to initiate the experiment was to follow the literature available for $NaClO_3$ NQR at around 29.94 MHz. The literature discusses the variation of the NQR frequency with external factors such as temperature, humidity and pressure [**69**] [**68**], however this was not controlled in this experiment. These external factors were assumed to be constant. In this experiment only a single pulse was used to gate the high power RF to excite the sample.

We start the discussion of the results with figure 4.7 which shows two signals, one with an empty glass test tube and the other with a sealed glass tube containing white crystalline sodium chlorate. The signal was obtained by exciting the sample by a pulse of 29.94 MHz RF signal which is where the NQR for Cl^{35} in $NaClO_3$ is expected to be. It is very clear that there is an obvious increase in the signal which has occurred only by replacing the empty tube with a tube containing the sample.

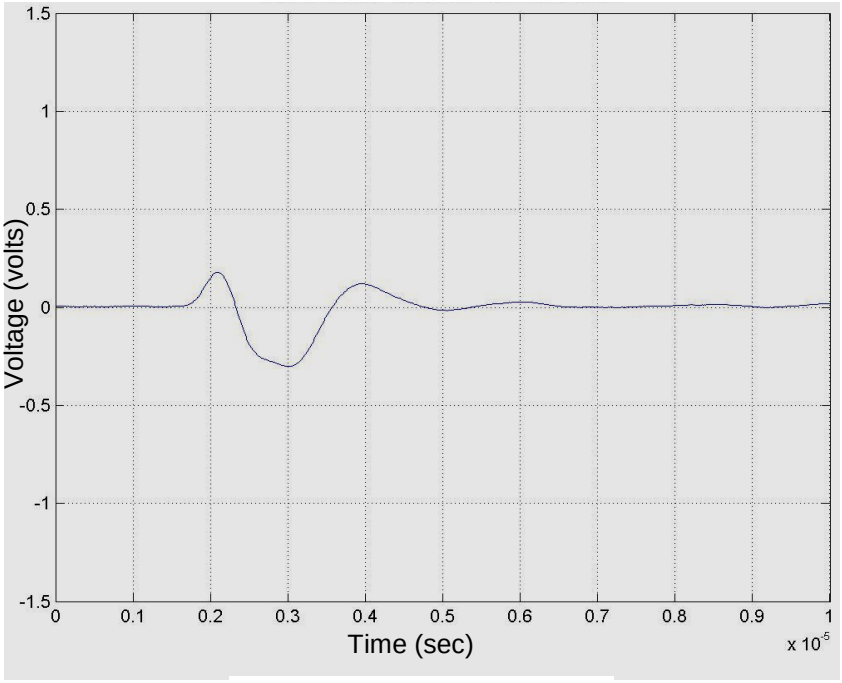

(a)

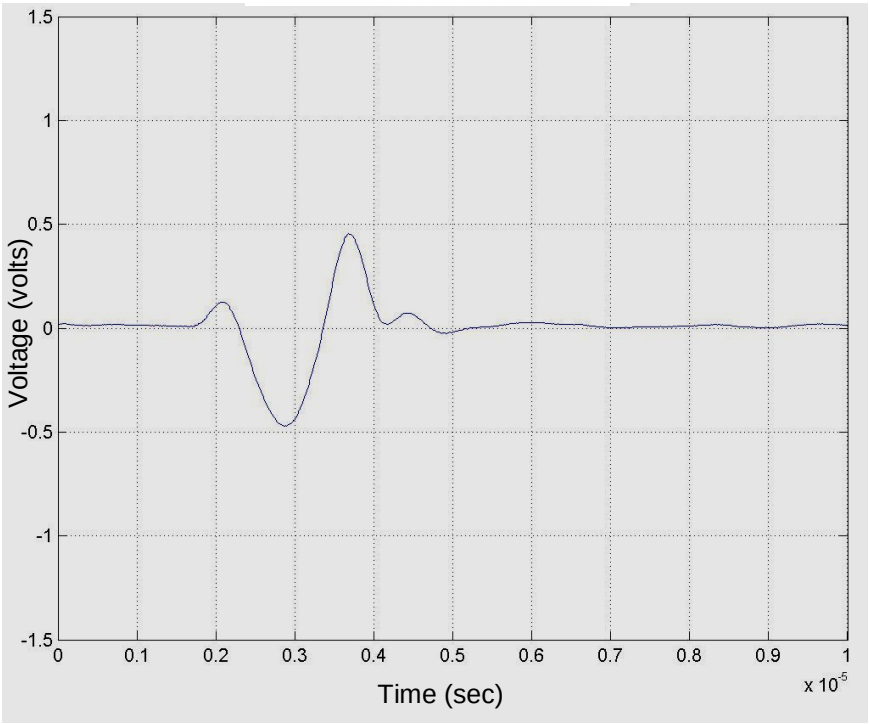

(b)

Figure 4.7: Signal obtained by detecting magnetic component with (a) an empty glass tube and (b) with a sample test tube at 29.94 MHz

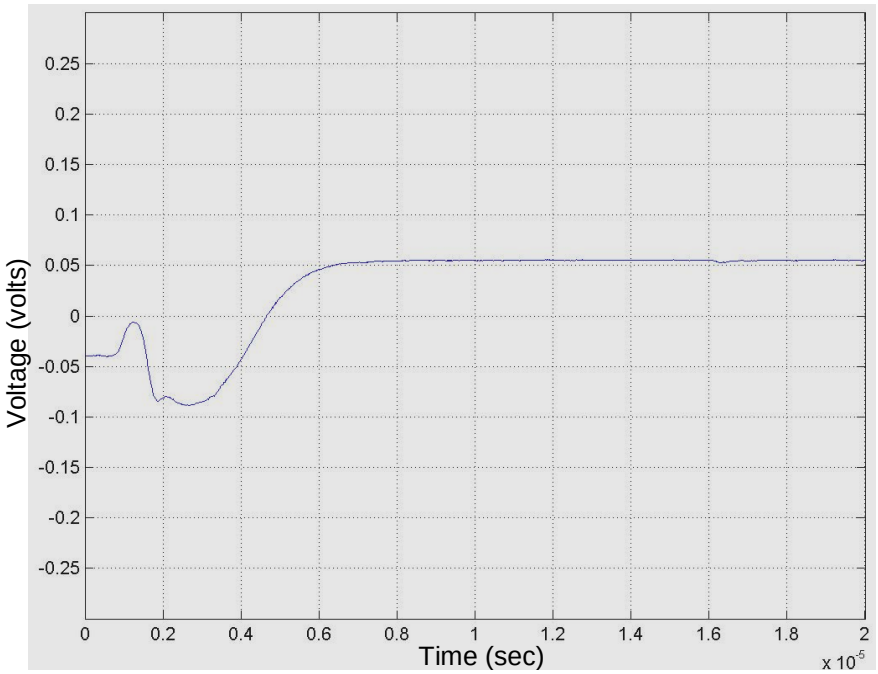

(a)

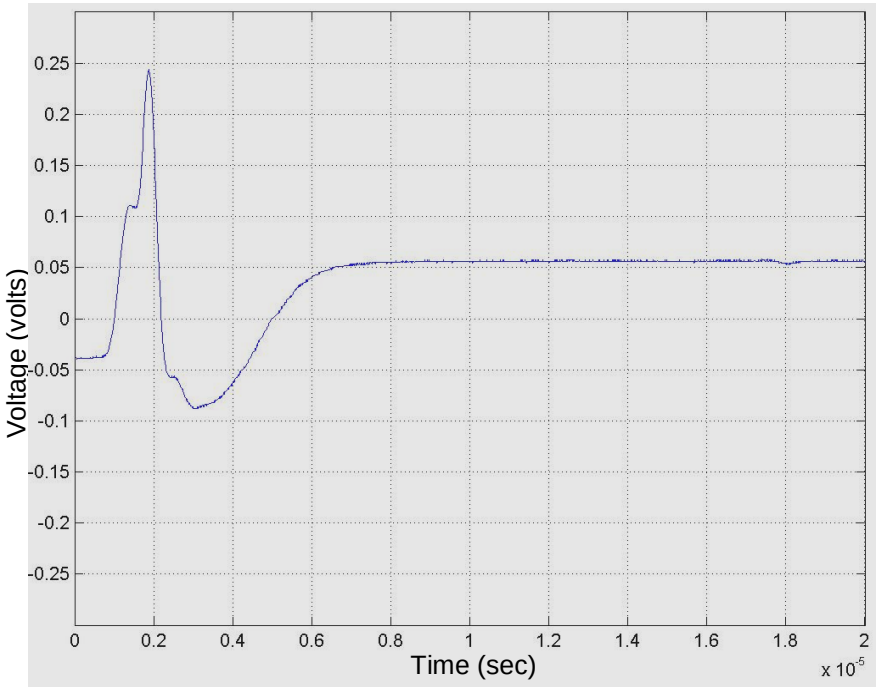

(b)

Figure 4.8: Signal obtained by detecting electric component using the EPS with (a) an empty glass tube and (b) with a sample test tube at 29.94 MHz

Having done one set of measurements by detecting the signal from the pickup coil, the high impedance EPS, discussed in chapter 2, was used to capacitively couple to the empty and sample test tubes. This was done in the same manner as shown diagrammatically in figure 3.12. Figure 4.8 shows a pair of results when the sensor was put in contact with the gold foil on an empty glass tube and the sample tube. Clear distinctions can be observed in the signal which has resulted due to the enhanced ring down of the tank circuit due to the presence of the sample tube.

These two set of results confirm the enhanced ring down of the tank circuit at 29.94 MHz in the presence of the sample when the signal was acquired both conventionally as well as by using the electric field detection using the high impedance EPS.

Since the intention is to study the signals acquired capacitively, a number of parameter combinations were attempted and the signals were acquired. There are a number of parameters that can be altered to see the effects which includes number of pulses, pulse width, repetition rate, gap between the pulses, input power and of course, the driving frequency and this is when the external factors are discounted. Clearly, the combinations of such parameters are an impractically big number of trials- If we have 10 choices for pulse widths to choose from, 10 driving frequencies and 10 power levels then that will lead to 1000 combinations. To make it more practical and yet still a comprehensive study, we have restricted to the use of only one pulse, the pulse width of which was experimentally determined and was one of the available choices. The driving frequency and the power levels were varied to collect the results so that they may be compared and contrasted vis-a-vis with an empty glass tube and with the sample tube to conclusively suggest that the signal change is occurring due to the sample and not due to spurious coupling of energy in to the tank circuit.

The following set of results will show, vis-a-vis, the signal detected by the capacitively coupled EPS when the empty glass tube was placed in the test rig and when replaced by the actual sodium chlorate sample.

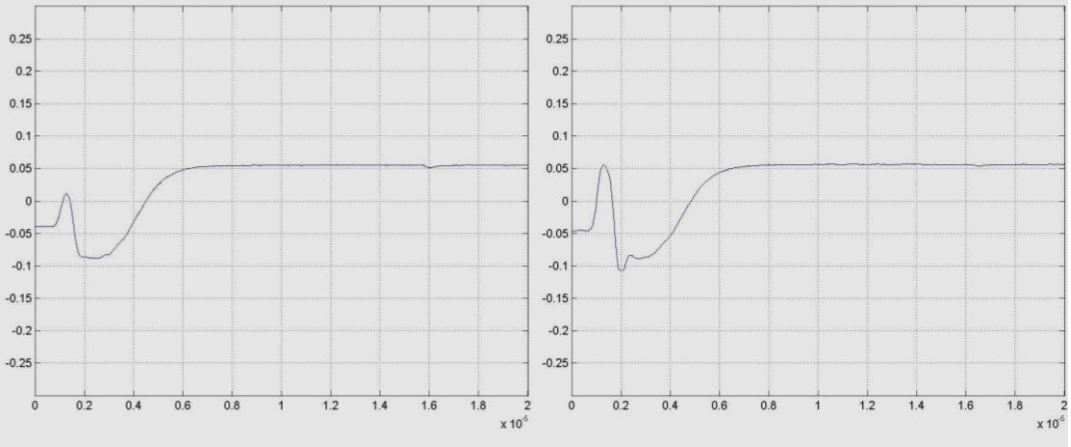

(a) (b)

Figure 4.9: Electric field signal at 29.90 MHz (a) with empty glass tube (b) with sample tube

X-Axis: Time (sec), Y-Axis: Voltage (volts)

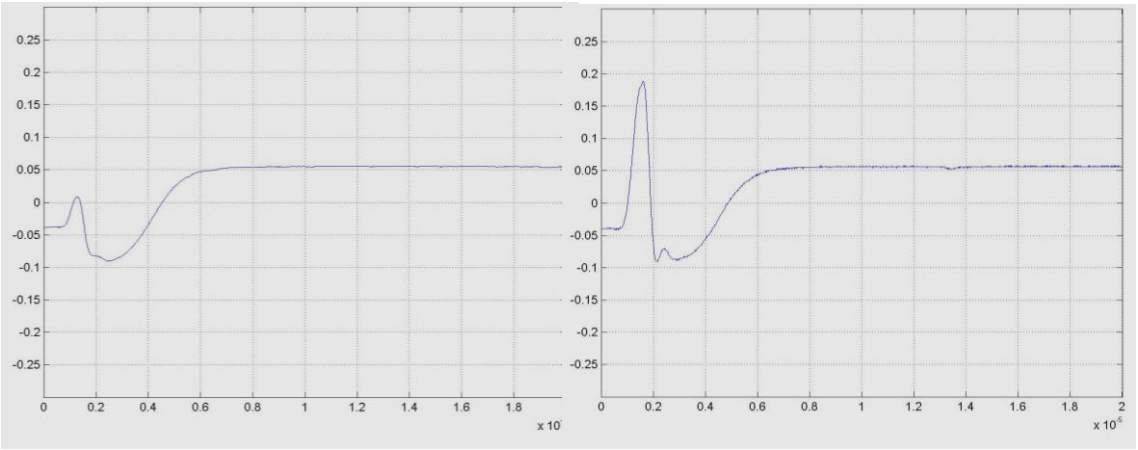

(a) (b)

Figure 4.10: Electric field signal at 29.91 MHz (a) with empty glass tube (b) with sample tube

X-Axis: Time (sec), Y-Axis: Voltage (volts)

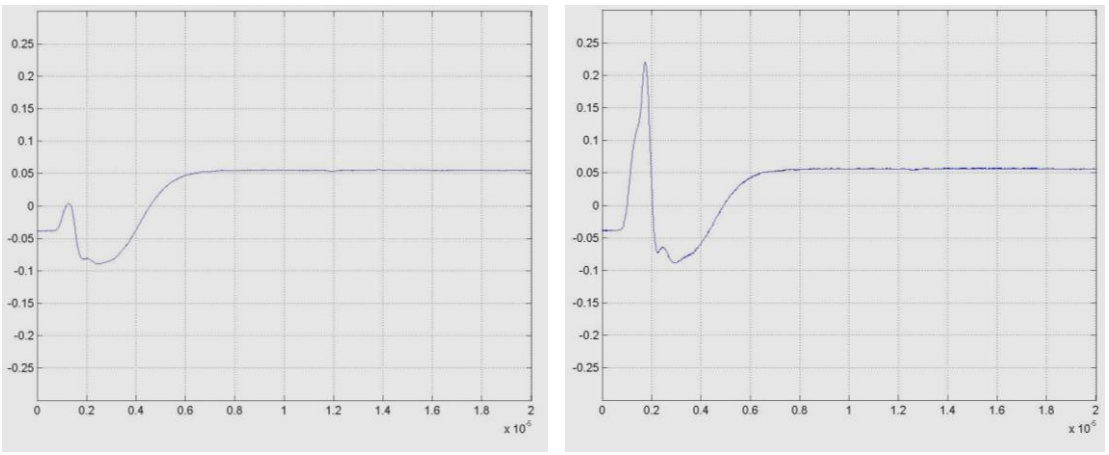

(a) (b)

Figure 4.11: Electric field signal at 29.92 MHz (a) with empty glass tube (b) with sample tube

X-Axis: Time (sec), Y-Axis: Voltage (volts)

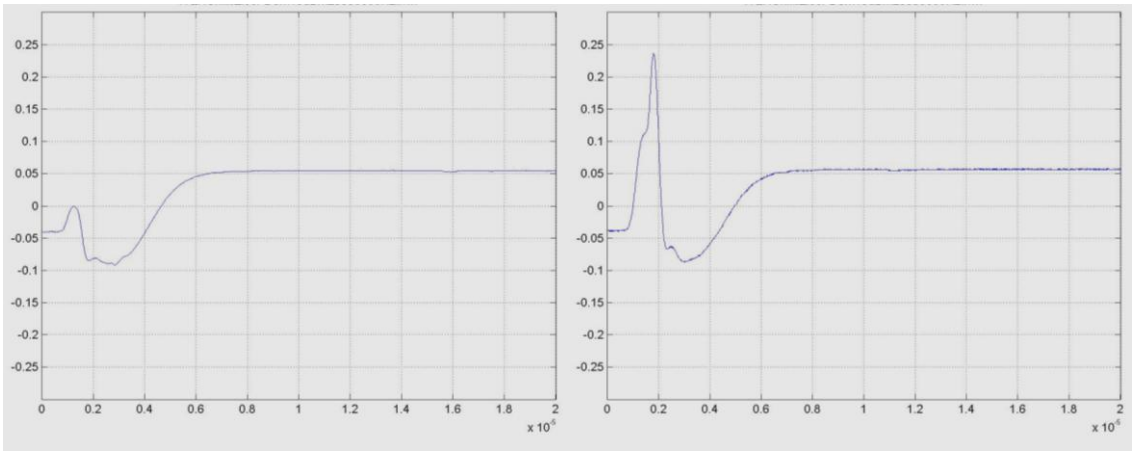

(a) (b)

Figure 4.12: Electric field signal at 29.93 MHz (a) with empty glass tube (b) with sample tube

X-Axis: Time (sec), Y-Axis: Voltage (volts)

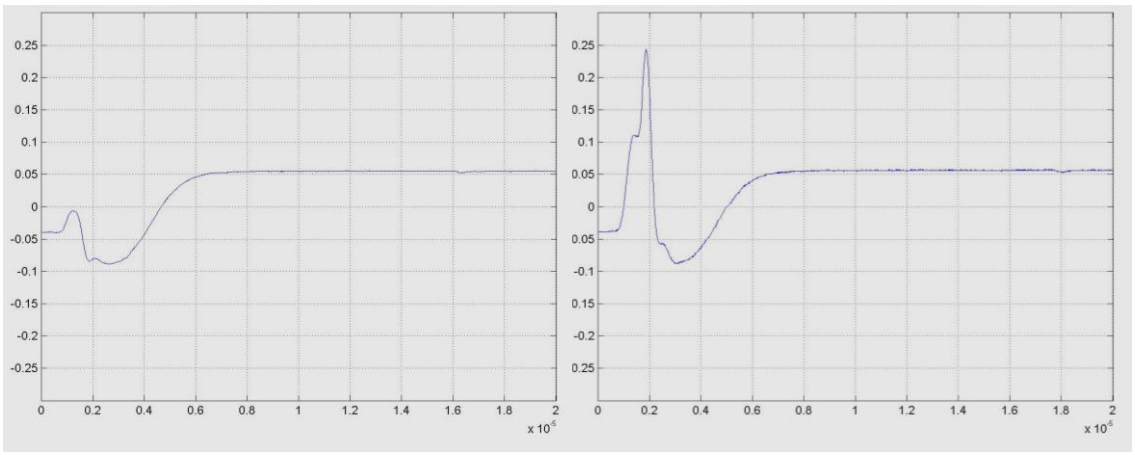

(a) (b)

Figure 4.13: Electric field signal at 29.94 MHz (a) with empty glass tube (b) with sample tube

X-Axis: Time (sec), Y-Axis: Voltage (volts)

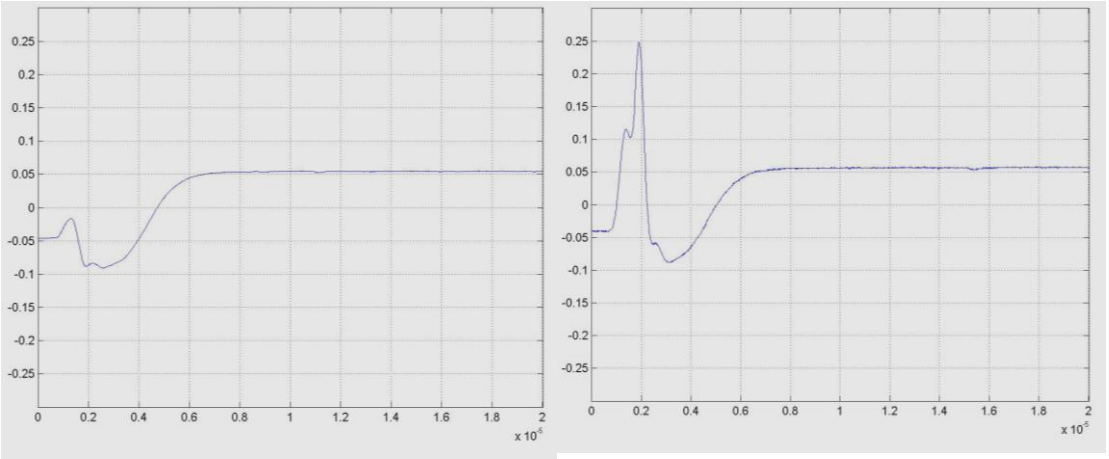

(a) (b)

Figure 4.14: Electric field signal at 29.95 MHz (a) with empty glass tube (b) with sample tube

X-Axis: Time (sec), Y-Axis: Voltage (volts)

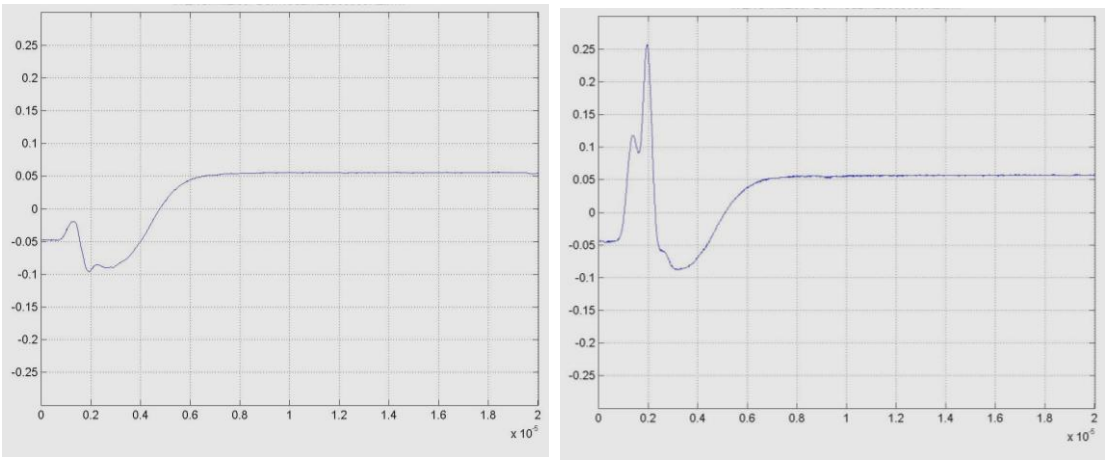

(a) (b)

Figure 4.15: Electric field signal at 29.96 MHz (a) with empty glass tube (b) with sample tube

X-Axis: Time (sec), Y-Axis: Voltage (volts)

Figure 4.9 shows this situation when the tank circuit is driven by a RF energy burst at 29.90 MHz, a frequency, not very but fairly distant from the frequency where we expect to observe NQR of Cl^{35} in $NaClO_3$. Evidently, the difference between the two signals, with and without the sample is not significant. However, the frequency was gradually increased at steps of 10 KHz, and as seen in figure 4.10 to 4.15, where the driving frequency is 29.92 MHz to 20.96 MHz, at 10 KHz steps, the effect of putting the sample tube in the tank circuit ring down is significant. The amplitude of the ring down signal envelop is two to three times bigger, a sign of the presence of the NQR signal. By continuing to do so, we reach a region the self resonance frequency of the tank circuit in which case the tank circuit resonance suppresses the effect of any other signal including the presence of sample as shown in figure 4.16 where the signal has been obtained by driving the experiment at 30.05 MHz.

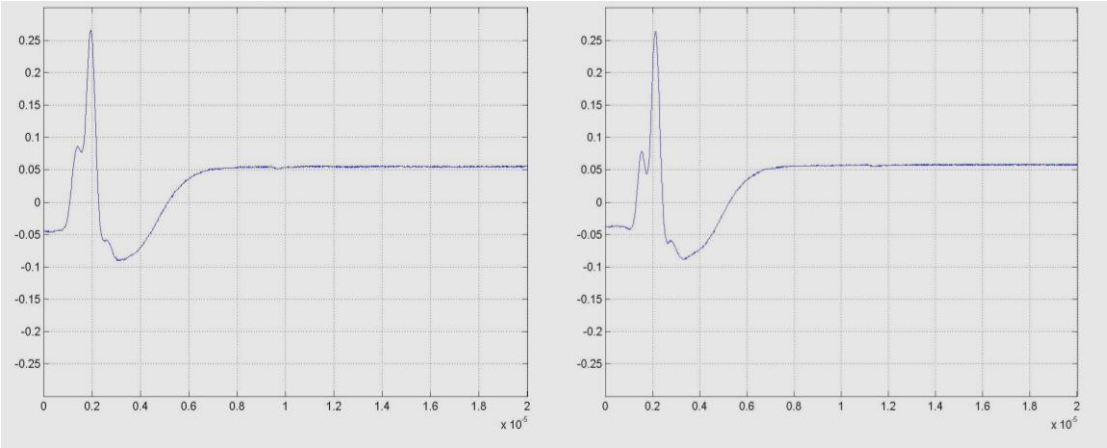

(a) (b)

Figure 4.16: Electric field signal at 30.05 MHz (a) with empty glass tube (b) with sample tube

X-Axis: Time (sec), Y-Axis: Voltage (volts)

It is clear that the characteristic NQR signal appears in the region where it is expected to be seen and goes away when the frequency is increased beyond and eventually the circuit shows its self resonance. All these signals have been recorded by experimenting with different lengths of pulse, frequency and power levels. The pulse width which results in maximum signal amplitude, otherwise known as 90^0 pulse has been chosen for the rest of the experiment. Obviously the NQR signal is also a function of the amount of energy being coupled into the tank circuit. Too much or too little energy will result in spurious ring down and no effect, respectively. The next set of result will show the effect for a fixed frequency of 29.93 MHz and varying the input power.

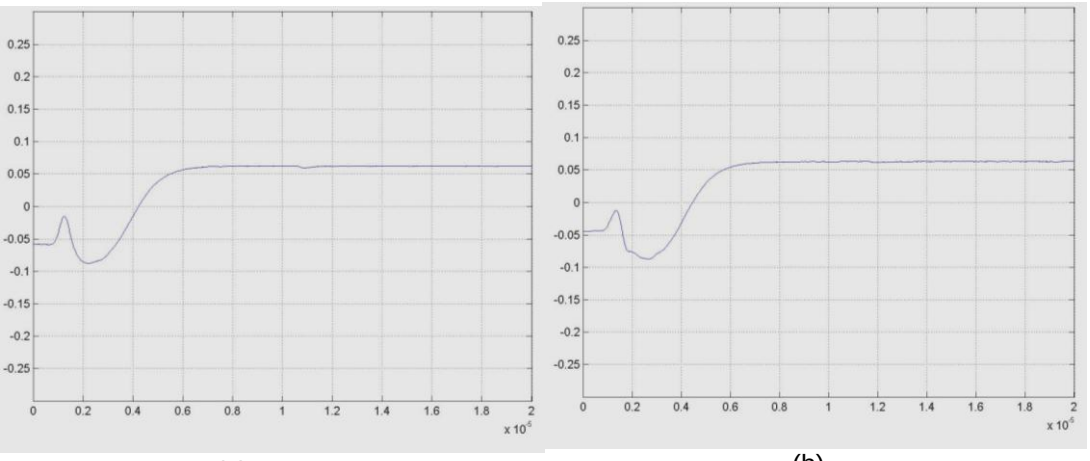

(a) (b)

Figure 4.17: Electric field signal with input power level of 14 dBm at 29.93 MHz (a) with empty glass tube (b) with sample tube

X-Axis: Time (sec), Y-Axis: Voltage (volts)

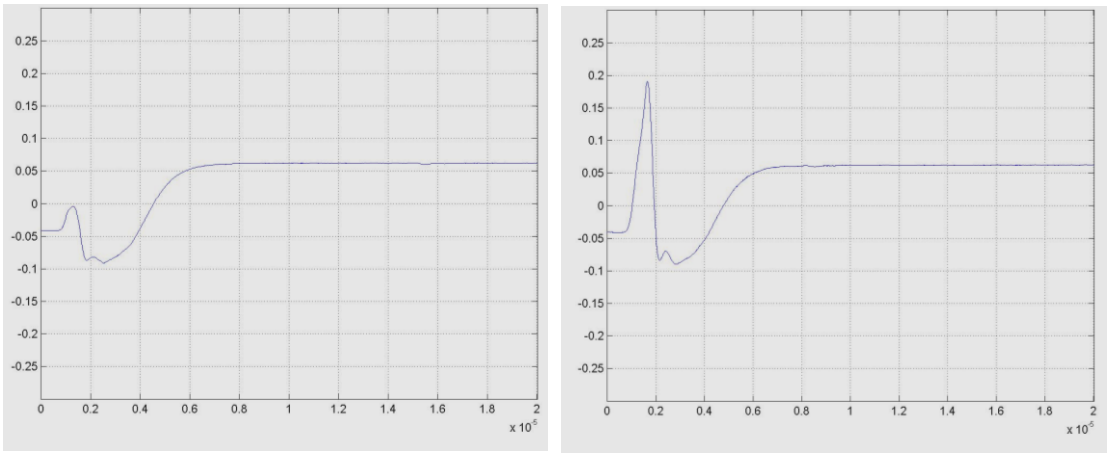

(a) (b)

Figure 4.18: Electric field signal with input power level of 15 dBm at 29.93 MHz (a) with empty glass tube (b) with sample tube

X-Axis: Time (sec), Y-Axis: Voltage (volts)

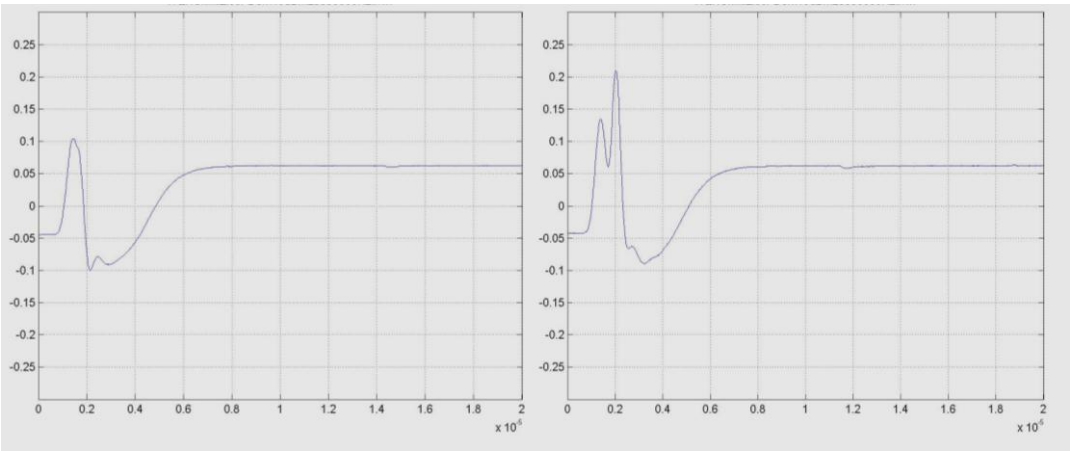

(a) (b)

Figure 4.19: Electric field signal with input power level of 16 dBm at 29.93 MHz (a) with empty glass tube (b) with sample tube

X-Axis: Time (sec), Y-Axis: Voltage (volts)

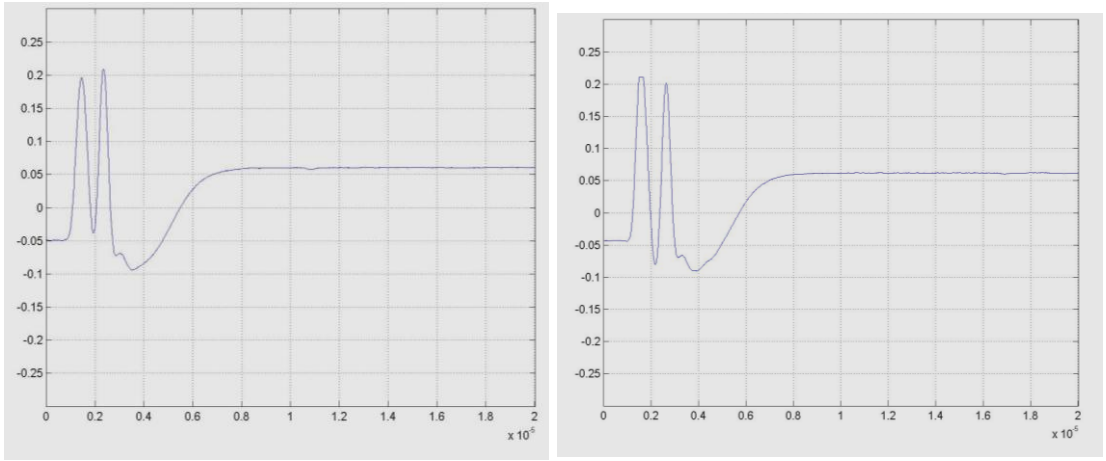

(a) (b)

Figure 4.20: Electric field signal with input power level of 18 dBm at 29.93 MHz (a) with empty glass tube (b) with sample tube

X-Axis: Time (sec), Y-Axis: Voltage (volts)

The amount of power being coupled to the tank circuit is clearly very important to observe the NQR signal. In this part of the experiment, we kept the frequency fixed and varied the power in logarithmic steps of 1 dBm. The R& S SMB 100A

signal source gives the option of changing the power in liner as well as log scales. Figure 4.17 shows the signals recorded for an input power of 14 dBm and it is clearly not enough to cause any appreciable difference in the magnetization vector and as seen in the result, no change in the tank circuit ring down has resulted by replacing the empty tube by the tube with sample. However, this situation changes rather significantly in figure 4.18, when the input power has been increased to 15 dBm and still discernable in figure 4.19 when the power is 17 dBm. With the optimum amount of energy coupled into the system, the noticeable change in the ring down signal envelop can be measured suggesting highly specific set of conditions in which the NQR signal results. In figure 4.20, clearly both the signals are alike, suggesting a heavily loaded tank circuit.

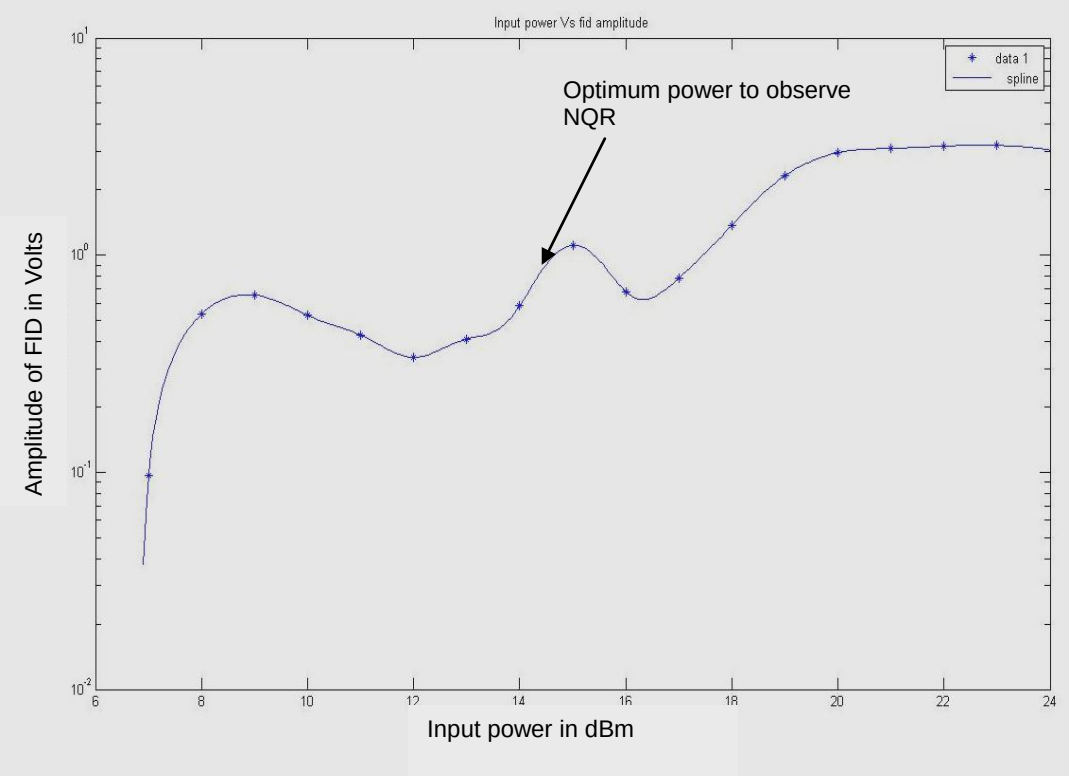

Figure 4.21: Amplitude of FID envelop versus input power

Figure 4.21 shows the amplitude of the free induction decay envelope when the sample was present in the experiment at the right frequency as a function of input power in logarithmic steps from 7 dBm to 23 dBm. Clearly there is a specific region for the given length of pulse being used to gate the RF, where the signal is most likely to be observable. This region of 15-16 dBm is where all the previous results have been obtained earlier in the chapter.

Chapter 5

Scanning Surface Microscopy

5.1 Introduction

In this chapter, an alternative technique of surface microscopy arrangement has been described using the broadband, ultra-high impedance EP Sensor. A capacitively coupled EP sensor is scanned across the sample in an XY raster manner in order to measure the local electric potential which is dependent on various parameters depending on the sample being scanned and the way in which it is excited. Depending on the type of sample and local features within the sample surface, the capacitance between the sample and sensor varies and so does the measured value of the electric potential. The data collected is then plotted to produce a two dimensional image of the sample properties.

The measurement instrumentation and arrangement described in this chapter set the stage for the next two chapters in which we describe the application of the broadband EPS for material characterisation and high resolution semiconductor IC scans. The strength of this type of measurement is that it is completely non contact, non-destructive and broadband. The inherently broadband version of the sensor allows us to, in theory, perform measurement over the entire range of frequency the sensor is operable which is up to 200 MHz. As discussed later the sensor data is required to be digitized for processing and acquisition which required higher sampling rate analogue to digital converter with reasonably good vertical resolution. In all the experiments reported in this and the following two chapters, a single two simultaneous channel, programmable gain digitizer, National Instruments USB 5133 has been used [**79**]. This is a 8-bit, 100 MSample digitizer with an USB interface which allows it to be programmed in LabVIEW. The data acquisition through the digitizer was integrated into the master VI which controls the movement of the

sensor head, allowing a single VI responsible for controlling the movement as well as the data acquisition.

The measurements described in this chapter and chapters six and seven can be divided into two major categories based on the test samples; Passive samples which require external excitation; and active samples where the signal of interest is intrinsic to the sample.

Surface topography imaging mentioned in this chapter, material characterisation of dielectric material and resistive carbon composite materials described in chapter six, fall into the category of passive sample measurements and hence require some form of external excitation. These measurements have been performed over a wide range of frequencies, from 10 KHz to 20MHz, and with relatively high spatial resolution of the order of 100 µm, demonstrating the high resolution as well as broadband capability of the measurement technique.

An active solid state CMOS integrated circuit (IC) sensor, described in chapter seven, is an active sample and the micro scale metal electrode array of pixels within the substrate was imaged. Sense electrodes of different physical dimensions were used to demonstrate varying degrees of spatial resolution of the technique, leading down to a resolution of 5µm, further adding to the microscopic resolution capability of the sensor.

The measurements described in this part of the thesis form a completely new set of non-contact electric potential measurement where the broadband operability as well as high spatial resolution has been demonstrated at the same time, with the single broadband, high impedance EP sensor.

5.2 The scanning system

Figure 5.1 shows a generic arrangement for the two dimensional scanning system that has been employed. The arrangement consists of an XY table with lead screws that are stepper motor controlled [**89**]. A carriage is built into the lead screw which is used to mount the EPS and the sense electrode. This provides very precise movement of the probe head over the sample. The

instrument is designed to be controlled by National Instruments LabVIEW software running on a PC. It is possible to set the dimension of the scan and the step size between each movement in software which is useful in dictating the dimension and resolution of the scan.

The EPS electronics, described in detail in chapter two, is housed in a guarded box. The sense electrode is a co-axial arrangement with the outer conductor being the guard and the inner conductor being the sense input. Different diameters of outer conductor provide different degrees of spatial resolution. Generally the fine structures of the electrodes were secured in a block of high resistance epoxy resin to provide mechanical strength. Different diameter probes have been used depending on the sample and type of investigation. The sensor-electrode is held orthogonally above the sample which was laid flat on the XY table bed. The probe head was moved in a raster fashion over software defined dimensions and with a step of micrometer resolution to collect sets of data using a LabVIEW programmable NI USB-5133 digitizer [**79**] that was plotted, in situ, to produce the two dimensional images of the material properties of the sample as a function of position.

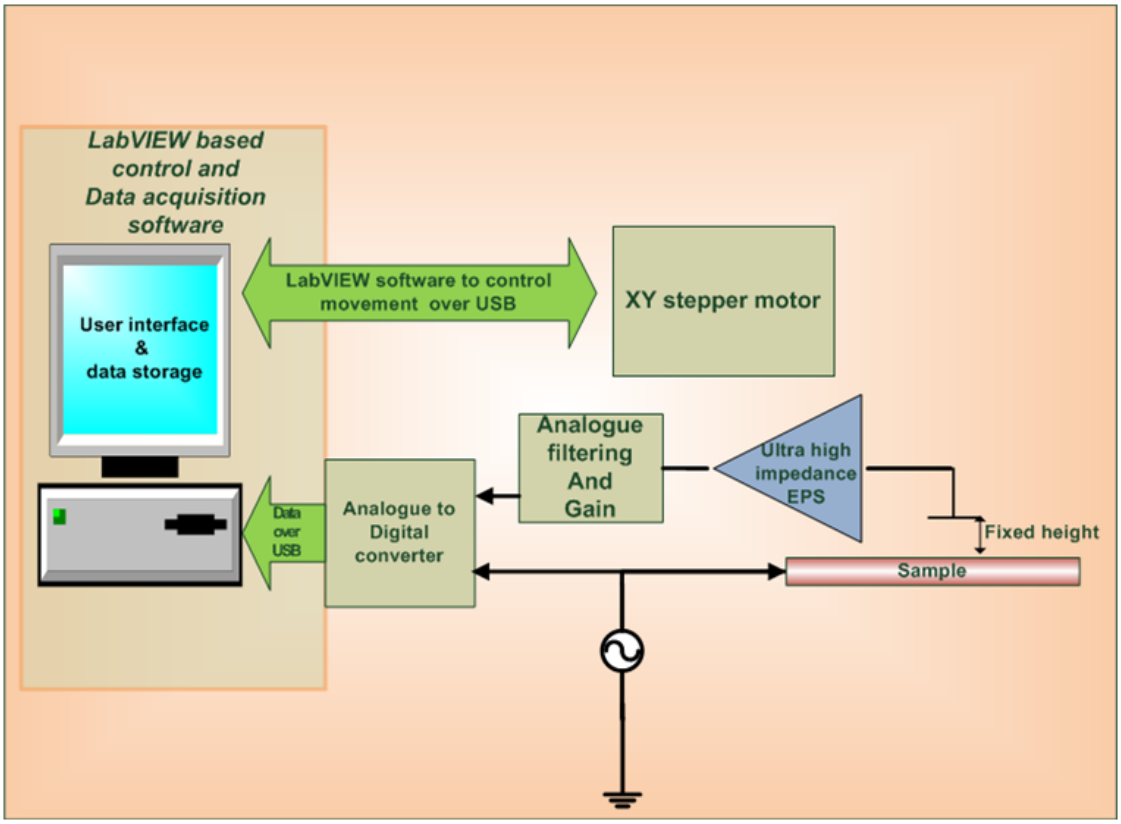

Figure 5.1: Overview of the scanning and data acquisition arrangement

5.3 Broadband imaging of surface topography

The first of the series of measurements performed was to employ the XY scanning system to measure the local variation of electric field due to surface topography. A standard printed circuit board (PCB) FR4 board with copper tracks milled onto it was used as a sample. The copper tracks were all connected at one point. An AC voltage of know frequency and amplitude was applied to it which then gets distributed across the entire plane of the board through the conducting copper tracks, making the conducting part of the sample equipotential. The high impedance EP sensor is then scanned across a section of the sample at a fixed height of 50 µm to obtain a two dimensional distribution of electric potential.

For this particular measurement, the variation of the AC potential due to the surface topography is measured by raster scanning a 12.6 mm x 12.6 mm

section of the sample. The process is repeated for signals of different frequencies within the sensor bandwidth. Because the EP sensor designed for this application has a broad frequency response, it was possible to use frequencies from 10 KHz to as high as 200 MHz. However, there are practical limitations that apply when using very high frequencies. In order to acquire the signal, the digitizer must be able to sample it fast enough and in practice, faster it can sample the better the quality of the digitized waveform. Also, to be able to detect small changes in the signal, a high bit count will result in improved vertical resolution. This USB digitizer with programmable gain allows the vertical bits to be divided across a smaller dynamic range. The maximum frequency of signal used was 20MHz. This ensures that the signal was sampled at least 5 times to achieve a faithful reproduction.

A reference signal of 20 V peak to peak and known frequencies is applied from a signal generator to the copper tracks on the PCB sample and the same signal has been used as a reference which was connected to one of the analogue channels of the digitizer. A LabVIEW virtual instrument was developed that integrates both control software for the stepper motors and the data acquisition through NI scope digitizer. Additional software filtering and a software lock-in was incorporated that gives the amplitude of the detected signal which is proportional to the surface feature of the sample at different points as the sensor is moved. All the data corresponding to each coordinate was saved in array format which was also used to visualise in two and three dimensions featuring the surface topography of the sample.

5.4 Results

Figure 5.2 shows the sample which was used to perform the scan. Copper tracks of parallel straight lines and curved nature have been milled using standard milling technique using a milling machine on a standard FR4 double sided PCB. The area defined by the square, as shown in the image, is the 12.6 mm x 12.6 mm section of the sample which was scanned.

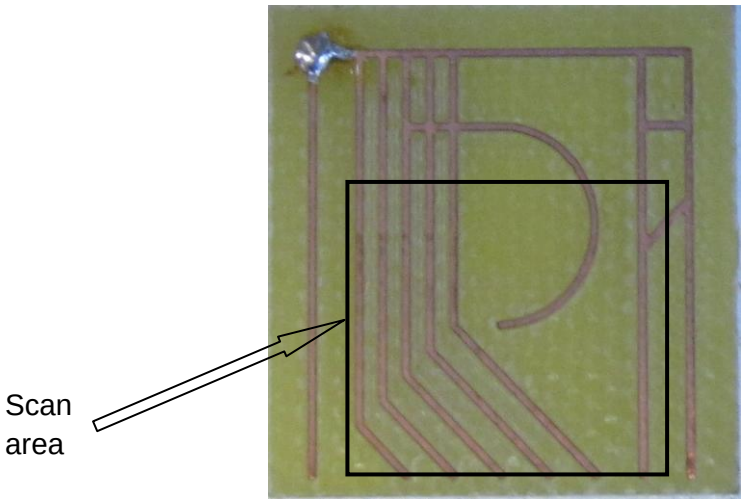

Figure 5.2: Optical image of the test PCB sample with large features in the form of conducting tracks on dielectric substrate, milled on one surface.

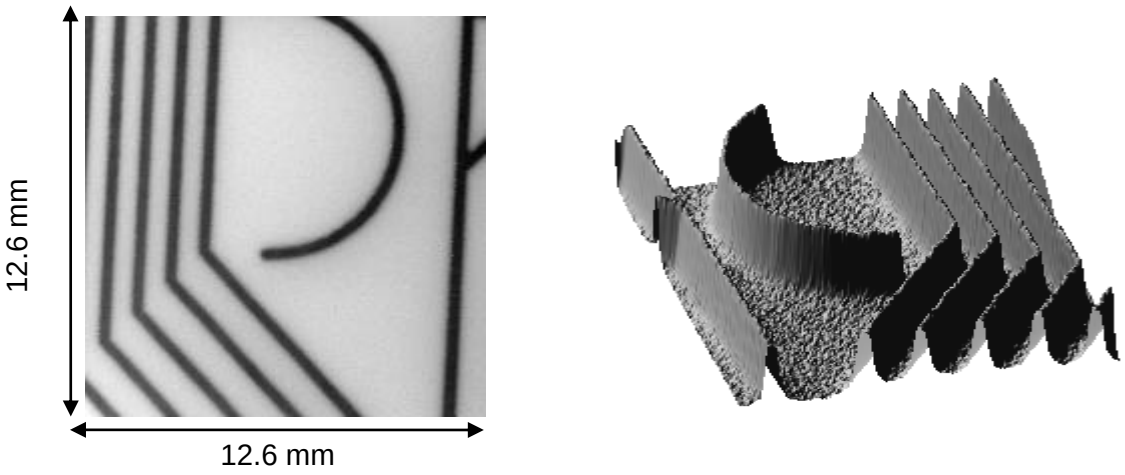

Figure 5.3: Surface topography obtained at 10 KHz frequency with a sense electrode diameter of 1mm. (a) 2-D image and (b) 3-D rendering

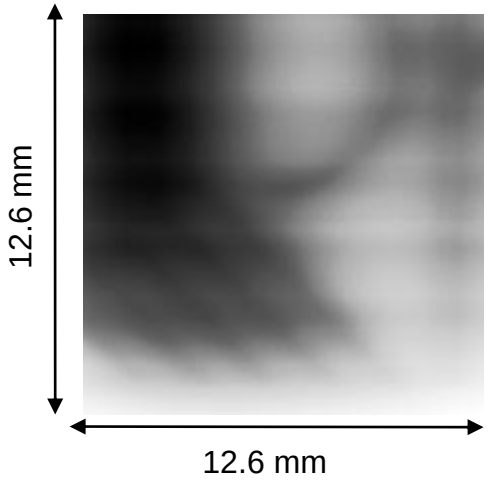

Figure 5.4: Surface topography obtained at 20 MHz frequency with a sense electrode diameter of 60 μm.

Figure 5.3 shows a two dimensional and three dimensional rendering of surface topography of the sample. To obtain this, an excitation signal of amplitude of 20V peak-to-peak and frequency of 10 KHz was applied to the sample. The sense electrode used in this case had an outer diameter of 60 µm. The height of the EPS above the sample was maintained at 50 µm throughout the scan and the EPS was stepped at 60 µm, to match the physical dimension of the electrode. The surface potential of 200 x 200 points on the sample was measured in the X and Y direction respectively, resulting in a total scan dimension of 12.6 mm x 12.6 mm. As can be seen from the results, the parallel and curved copper tracks on the surface of the PCB, are clearly visible. This is the first in the set of results that shows strong contrast in the output signal between conducting and non-conducting regions on the surface scanned at 10 KHz.

Figure 5.4 shows a two dimensional image of the same section on the sample as Figure 5.3 with an excitation signal frequency of 20MHz. This is the other end of the spectrum of the frequency that has been used to perform these measurements. As can be seen, the copper tracks are still discernable but they are very smeared out and the image has a very poor contrast. This indicates a fundamental trade-off between bandwidth and spatial resolution in this type of measurement. The sense electrode used in this case was also the same one as in figure 5.4. This particular sense electrode was originally designed to perform imaging at lower frequencies which was constructed by using single core micro wire with silver paint around it to give it a guard structure. This however proved to be ineffective as guard for RF frequencies in the region of tens of MHz. A reliable guarding is very important for this type of measurement which helps minimising the capacitance of the electrode.

To overcome this problem, a readily available sense electrode, constructed by using a semi-rigid co-axial cable of outer diameter of 1 mm was used. In this case, the outer of the co-axial electrode is made of copper which is a much better conductor at high frequencies in this realm. Figure 5.5 and figure 5.6 show the results of 12.6 mm x 12.6 mm section of the sample at 2 MHz and 20 MHz, respectively. By visual inspection, it can be easily seen that the conducting copper tracks on the dielectric substrate on the surface of the

sample are very clearly visible as compared to Figure 5.5. However, it should be, noted that the contrast does suffer as the frequency is increased. The images obtained in this manner, therefore have a coarser spatial resolution compared to the scan results presented in figure 5.3. Nevertheless, this is perfectly fine while imaging large surface features such as this.

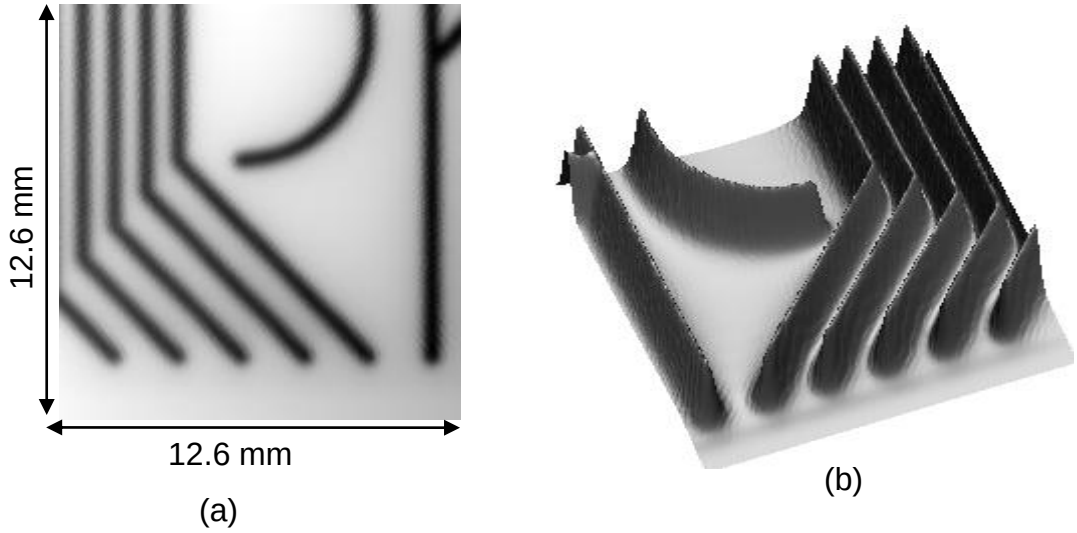

Figure 5.5: Surface topography obtained at 2 MHz frequency with a sense electrode diameter of 1mm. (a) 2-D image and (b) 3-D rendering

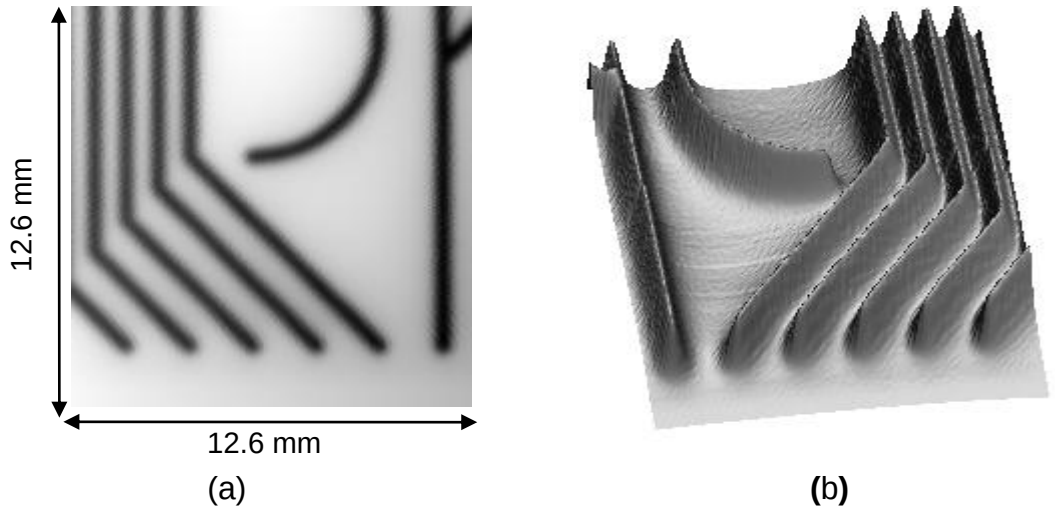

Figure 5.6: Surface topography obtained at 20 MHz frequency with a sense electrode diameter of 1mm. (a) 2-D image and (b) 3-D rendering

To further enhance the spatial resolution, a new sense electrode was constructed by using a semi rigid coaxial cable with outer and inner diameters of 200 µm and 50 µm. This fine coaxial structure was firmly potted with epoxy resin inside a PTFE outer. This gives a good compromise between the two different electrodes used.

Figure 5.7, 5.8 and 5.9 shows the results obtained by scanning the same section of the sample of 12.6 mm x 12.6 mm dimension using the new 200 µm electrode at 2 MHz, 10 MHz and 20 MHz respectively. All the three scans were performed at a fixed height of 50 µm above the flat sample surface.

As mentioned above, the contrast of the image gets poorer as the frequency of scan is increased. Among the various variable parameters in this type of scan, the height of the sense electrode above the sample is crucial. It is obvious that the coupling capacitance of the source to sensor is dependent on the air gap. A reduction in this height will result in a stronger coupling capacitance and, in

principle the signal that is coupled into the sensor will be less attenuated resulting in an improved sensitivity.

Figure 5.10 shows the result obtained by scanning the sample at 20MHz by lowering the sensor head to 20 µm above the sample. All the other parameters have been kept same as those in figure 5.9. By visual inspection, it can be seen that the contrast of the image obtained at a height of 20µm above the sample is better than that of 50µm.

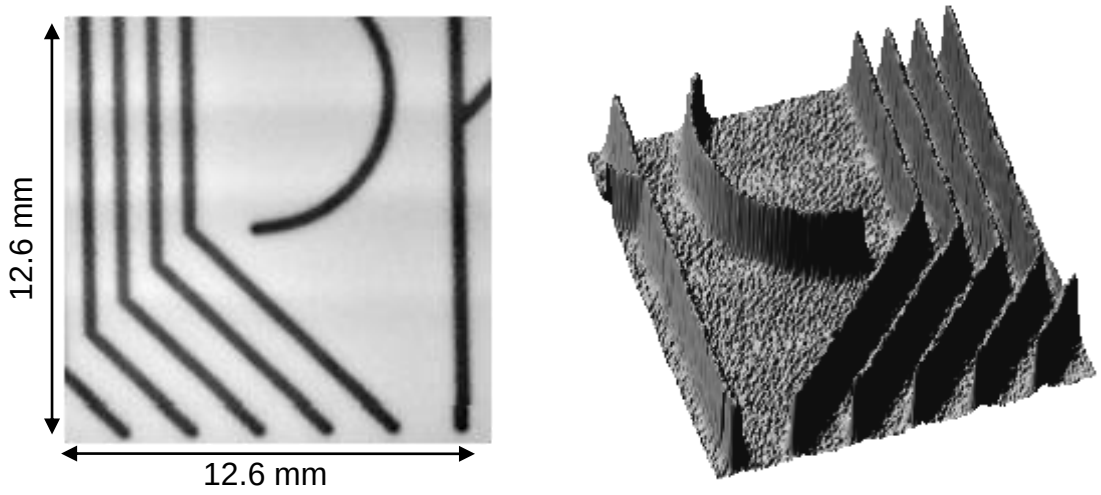

Figure 5.7: Surface topography obtained at 2 MHz frequency with a sense electrode diameter of 1mm. (a) 2-D image and (b) 3-D rendering

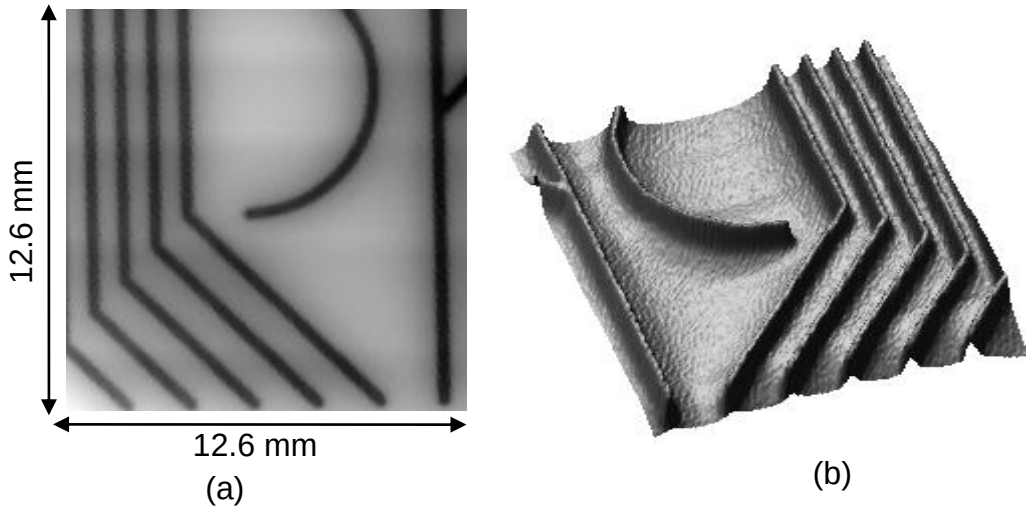

Figure 5.8: Surface topography obtained at 10 MHz frequency with a sense electrode diameter of 1mm. (a) 2-D image and (b) 3-D rendering

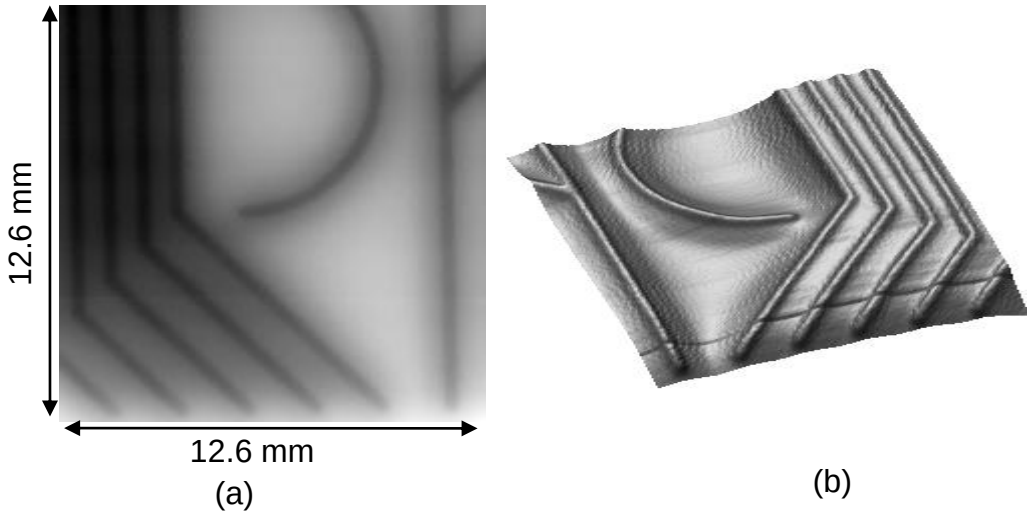

Figure 5.9: Surface topography obtained at 20 MHz frequency with a sense electrode diameter of 200µm; Scanned at 50 µm above the sample surface. (a) 2-D image and (b) 3-D rendering

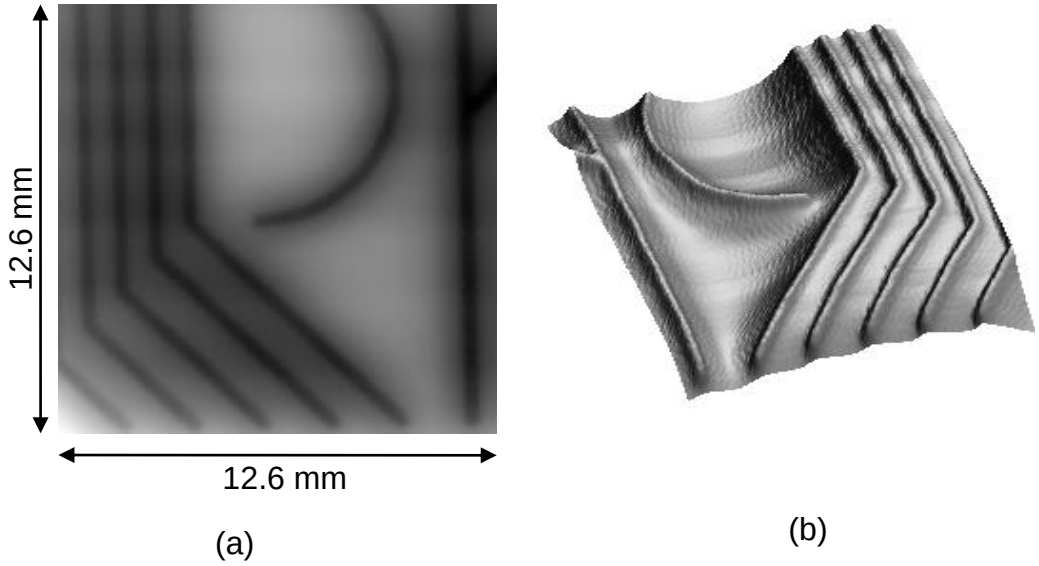

Figure 5.10: Surface topography obtained at 20 MHz frequency with a sense electrode diameter of 200µm; Scanned at 20 µm above the sample surface. (a) 2-D image and (b) 3-D rendering

Chapter 6

Material Characterisation

6.1 Introduction

The necessity to characterise different types of material is important. Critical information can be acquired on the basis of the various physical properties of materials. A significant portion of research community has taken seriously the problem of investigating different materials, for different properties at different scales. Chapter one details the literature review concerning this area.

The invention of EPS and its subsequent use in measuring electrical properties which are often frequency dependent supplements the techniques that are already available and addresses some of the limitations encountered by them. In this chapter two different material samples have been studied which are fundamentally different and therefore require different forms of excitations. The technique reported in this chapter uses the EPS technology, details of which are discussed in chapter two. The XY scanning system used here has been discussed in chapter 5. Results are presented which show the measurement of local dielectric properties and conductivity over a frequency range 10 KHz to 11 MHz, limited only by the electronics to digitize and signal processing. The spatial resolution of the order of 100 μm has been achieved which is also limited by the electrode design and may well be extended further with micro-fabrication techniques such as thermal metal deposition and lift-off. The method uses a single EPS to raster scan the sample under test.

6.2 Dielectric material

6.2.1 Method

The surface topography results of the sample discussed in chapter 5 produced images that were obtained by detecting changes in the local electric field in the conducting and non-conducting regions within the sample. The variation in the local electric field in the conducting and non-conducting region is large which makes the sensitivity of the system less of a critical parameter. This, nevertheless, demonstrate the efficacy of the technique over the broad frequency range of 10 KHz to 20MHz.

The subject of this section is a dielectric sample. The sample has been prepared by cutting a square section of 35mm x 35mm from a standard glass/epoxy FR4 circuit board. The copper on one side of the board was kept intact. On the opposite side of the board, all the copper was completely removed to expose the entire epoxy glass interweaved structure of the dielectric material. A number of linear defects, in the form of parallel straight lines, of varying widths have been machined on the dielectric surface. Figure 6.1 shows the optical image of the dielectric side of the sample.

The copper plane side of the sample was used to provide the excitation signal. Figure 6.2 illustrates an approximate situation of the test set up. The general experimental set up is similar to the one shown in figure 5.2 in chapter five. The high impedance EP Sensor was placed at a constant height above the surface of the exposed dielectric side of the sample and moved in a raster manner at predefined step size, consistent with the sense electrode dimension, measuring the electric potential at each co-ordinate. Each data point corresponds to the level of electric potential detected by the high impedance EPS which is a function of the excitation frequency, thickness of the material composition and local electric permittivity of the composite material. The detected RMS voltage was converted into a DC level in the LabVIEW VI used to acquire the data with the National Instrument NI-Scope 5133 USB digitizer. The data collected by the system are plotted using Gwyddion, open source data visualisation software [**90**].

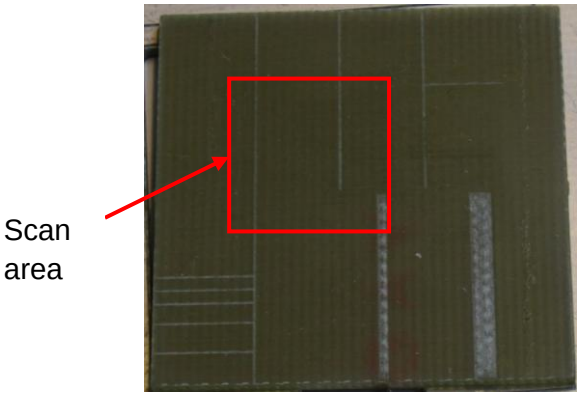

Figure 6.1: Optical image of the dielectric sample

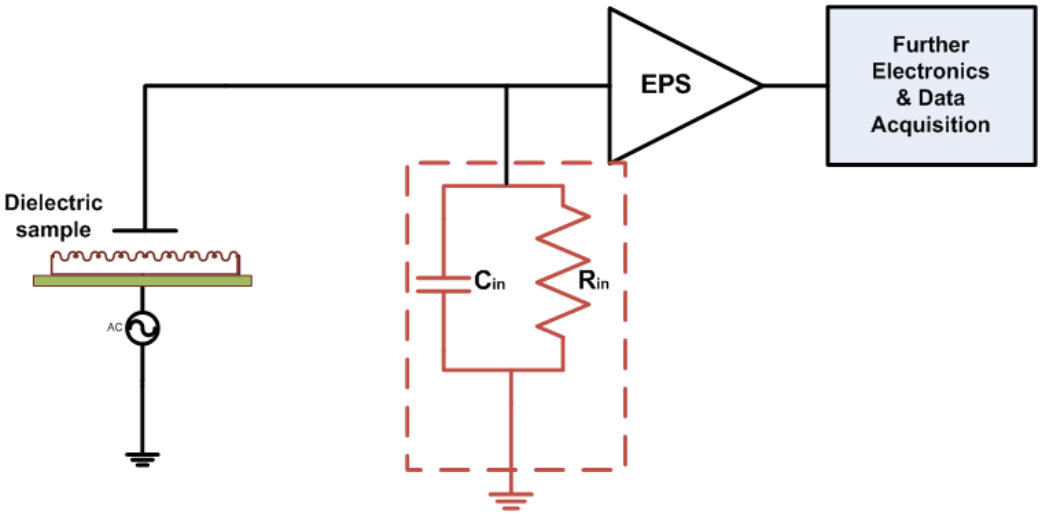

Figure 6. 2: Dielectric sample as set up for experiment

6.2.2 Results and Discussions

A number of scans were performed using a sense electrode of inner and outer dimension of 50 μm and 200 μm respectively. The excitation frequency was varied from 10 KHz to 11 MHz. The corresponding results were plotted as a two dimensional and three dimensional images which show the material structure of the sample that visually discriminates the machined faults and glass/ epoxy interweaved structure in both vertical and horizontal directions. The dielectric properties of material are frequency dependent and are often expressed by permittivity (ε_r).

The sample is a composite dielectric material with silica glass (ε_r~6.0) and epoxy resin (ε_r~3.4).The overall permittivity of the sample depends on various factors which include the ratio of glass to epoxy and the frequency of measurement [**91**]. Clearly, the difference between the dielectric constants of the two constituent materials is rather small which translates into very similar effect on the A.C electric field that is applied onto the sample. This small variation in the dielectric constant suggests that in order to detect the distribution of E-field over the sample area, the system needs to exercise high sensitivity. The results given below are the scans performed using the existing system.

Figure 6.3 to 6.7 show the results obtained by scanning 200 x 200 points at 63 μm step which translates into a scan area of 12.6 mm x 12.6 mm, scanned over duration of approximately 70 minutes. As can be seen in Figure 6.3, where the excitation frequency is 10 KHz, the linear defects and the interwoven structure of glass fibre in epoxy resin mat can be visibly distinguished. This is also true for results shown in figure 6.4 to figure 6.7, when the sample excitation frequency was progressively increased from 100 KHz, 1 MHz, 9 MHz and 11 MHz, respectively. Figure 6.8 shows result of a wider scan area which was performed initially just to have a general idea of the quality of scan at a low RF excitation frequency of 2 MHz. As the frequency was increased beyond 1 MHz, as shown in figure 6.6, 6.7 and 6.8, where the sample has been excited by frequencies of 9 MHz, 11 MHz and 2 MHz respectively, the contrast between

the glass and epoxy material is seen to be progressively deteriorating with increasing frequency. The contrast is rather poor for the data obtained by exciting at 11 MHz, as shown in figure 6.7 [**21**].

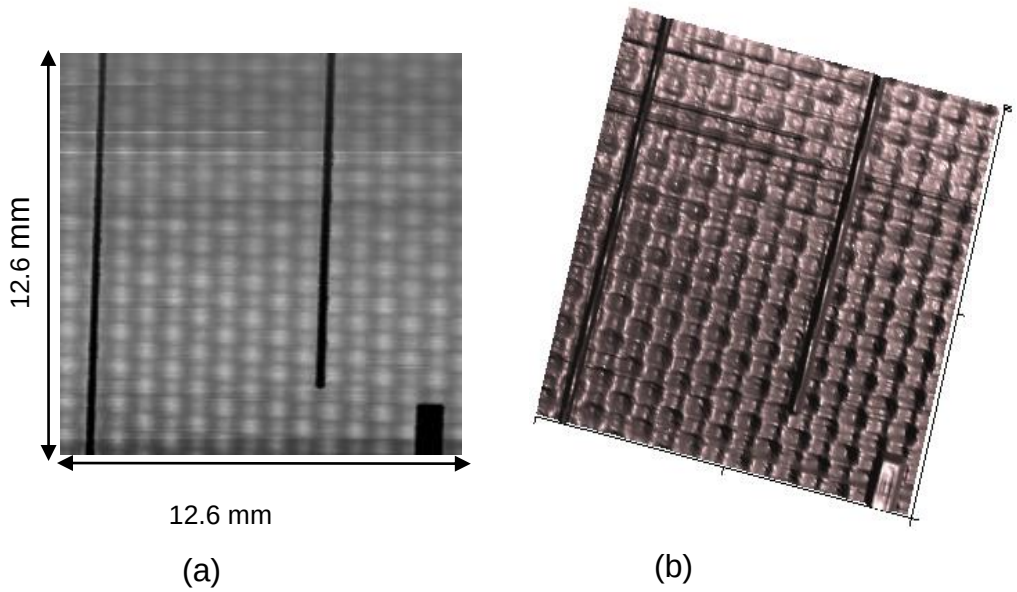

Figure 6.3: Local variation of dielectric properties of FR4 composite at 10 KHz (a) 2-dimensional and (b) 3-dimensional rendering

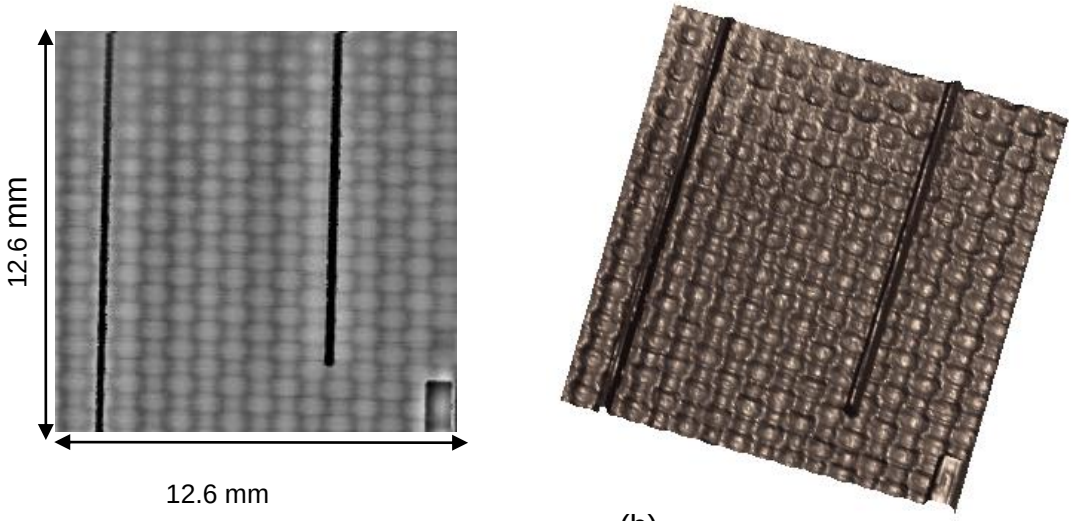

Figure 6.4: Local variation of dielectric properties of FR4 composite at 100 KHz (a) 2-dimensional and (b) 3-dimensional rendering

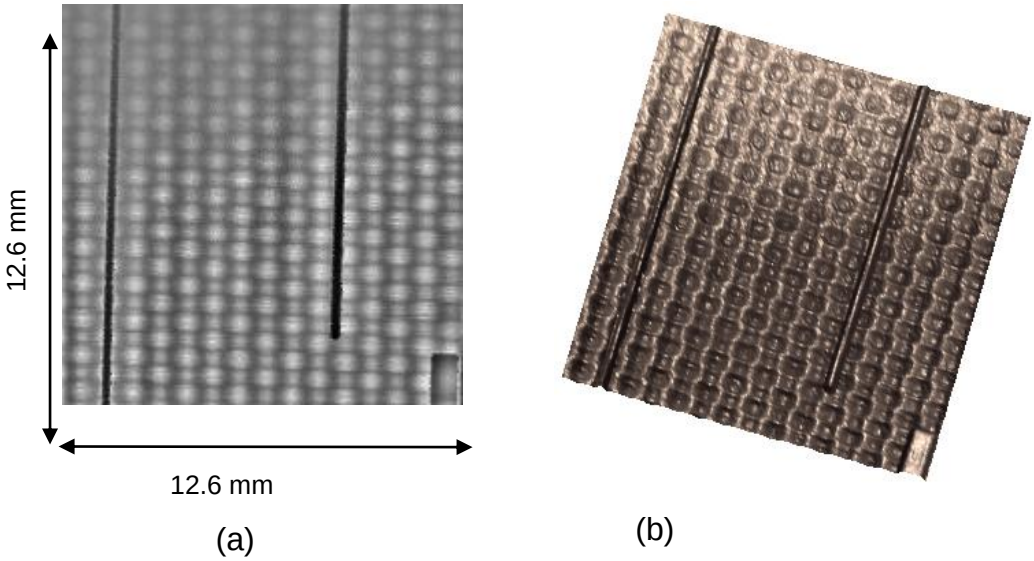

Figure 6.5: Local variation of dielectric properties of FR4 composite at 1 MHz (a) 2-dimensional and (b) 3-dimensional rendering

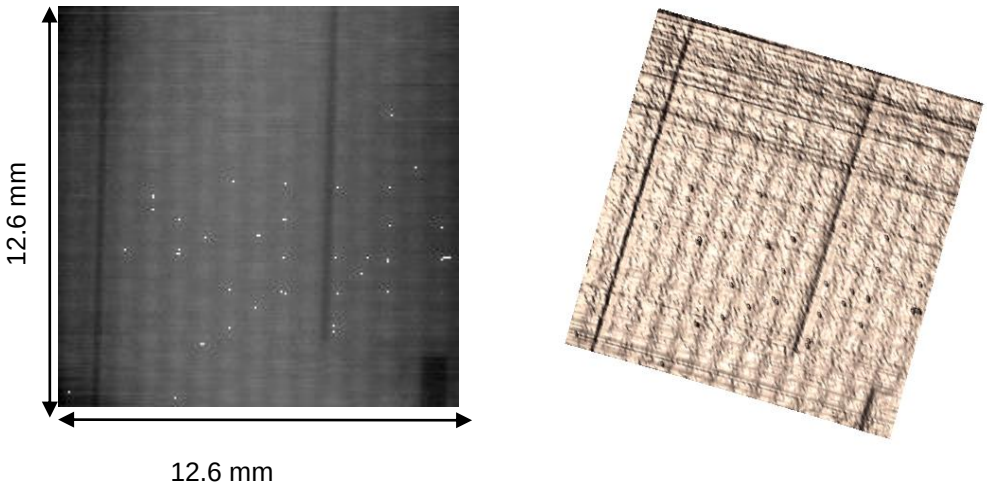

(a) (b)

Figure 6.6: Local variation of dielectric properties of FR4 composite at 9 MHz (a) 2-dimensional and (b) 3-dimensional rendering

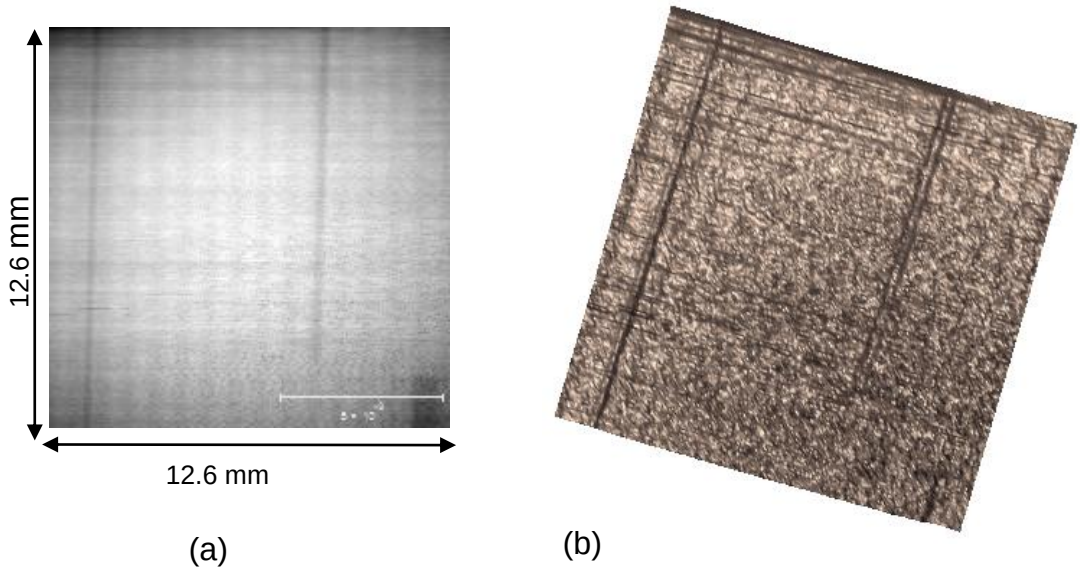

(a) (b)

Figure 6.7: Local variation of dielectric properties of FR4 composite at 11 MHz (a) 2-dimensional and (b) 3-dimensional rendering

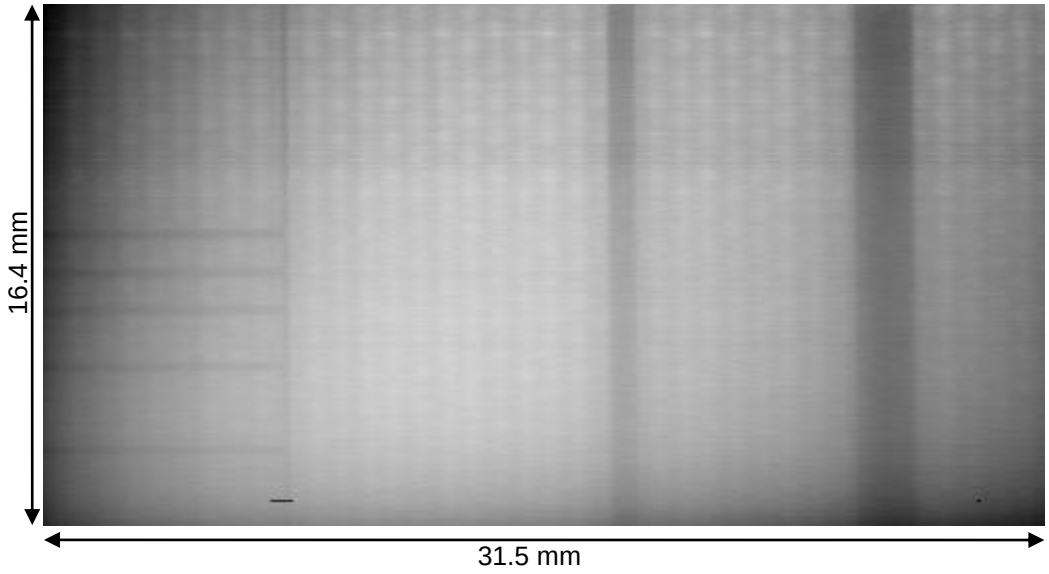

(a)

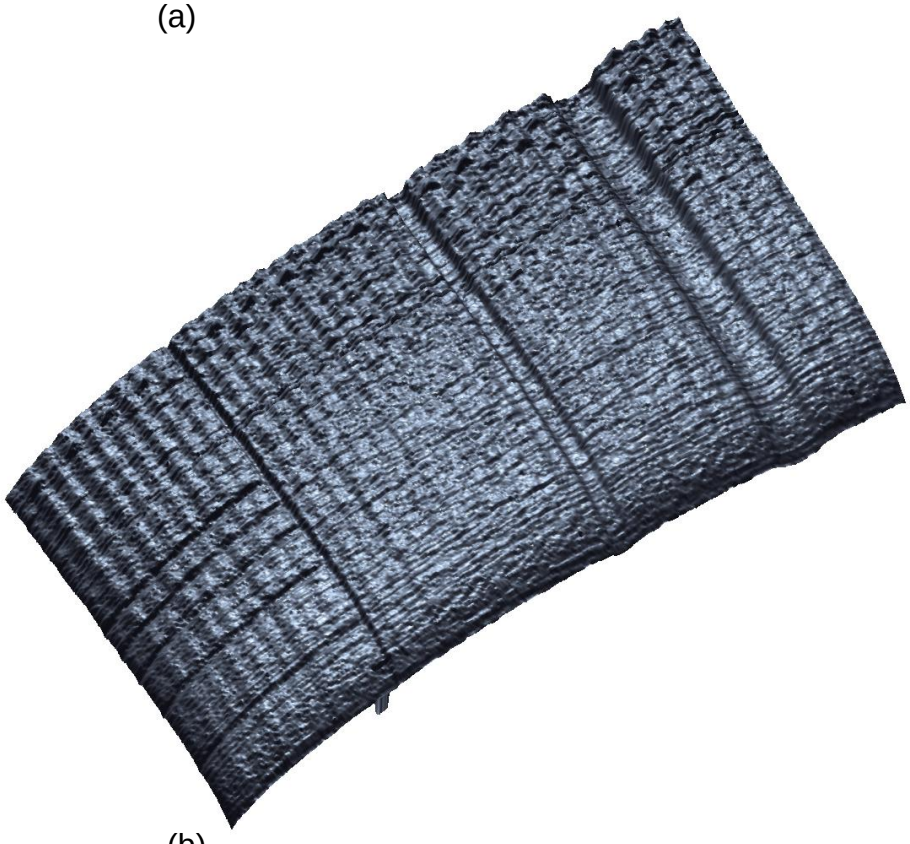

(b)

Figure 6.8: Local variation of dielectric properties of FR4 composite at 2 MHz (a) 2-dimensional and (b) 3-dimensional rendering

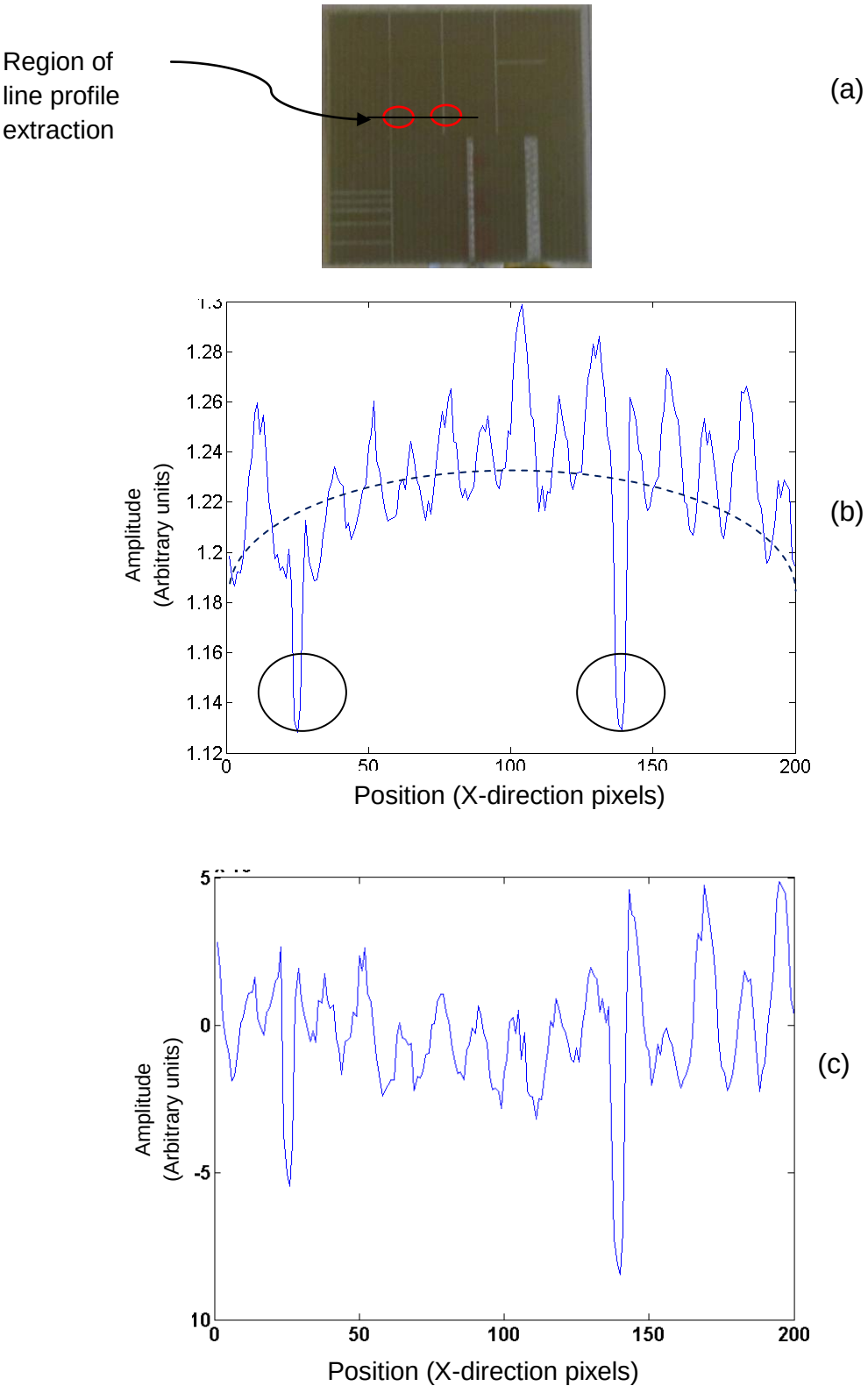

Figure 6.9: (a) Optical image of the sample showing the location where the line profile at 1 MHz has been extracted and shown in (b).(c) line profile after polynomial background curvature

A line profile extraction is shown in figure 6.9. The optical image of the sample shown in figure 6.9 (a) locates the section on the sample where a single line profile has been extracted and shown in figure 6.9 (b). A background curvature can be seen here which can be approximated to a polynomial fit by a curve fitting algorithm. This effect is caused by the sample curvature not sufficiently controlled at 50 µm level, which is the approximate height of the sensor above the sample. This polynomial background was subtracted from the raw data presented so far to allow one to see an improvement in the relative dielectric contrast between the two different materials in the composite sample. The image processed data can be seen in figure 6.10.

It may also be seen in Mumby et al. [**91**], that the dielectric property of the FR4 composite is frequency dependent and especially in the frequency range of 1 KHz to 1 GHz, the losses are highest around 10 MHz. This could account for the relatively poorer contrast at increasing frequencies and especially at 11 MHz, observed in figure 6.7.

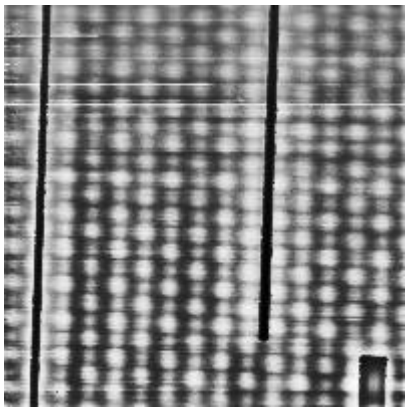

(a)

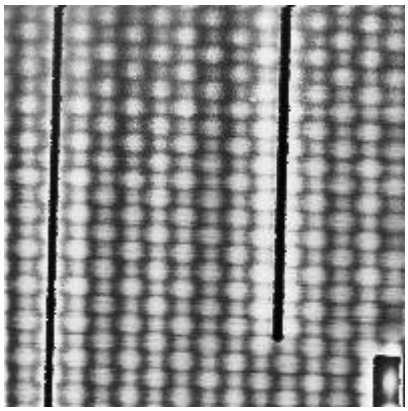

(b)

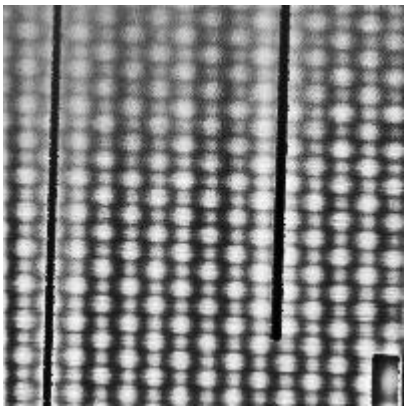

(c)

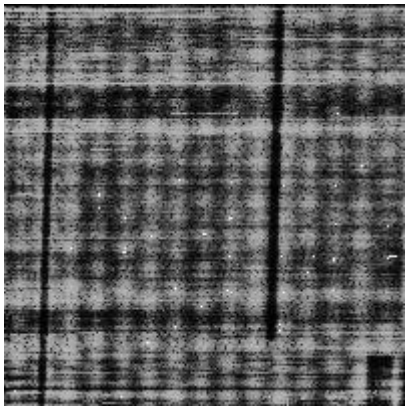

(d)

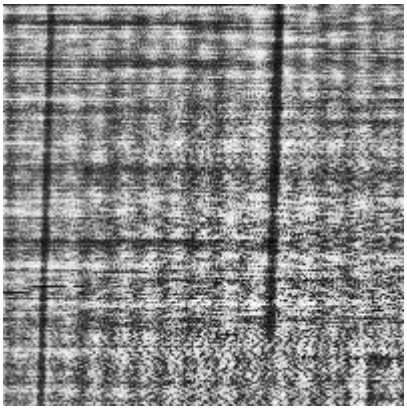

(e)

Figure 6.10: Image processed data (after subtracting the background curvature) (a) 10 KHz, (b) 100 KHz, (c) 1 MHz, (d) 9 MHz and (e) 11 MHz

6.3 Carbon composite based material

6.3.1 Electric potential and local conductivity

The following section provides a very simple mathematical treatment describing the dependence of local electric potential on the local conductivity of a material. Consider a linear element of conducting material in which the local electricity conductivity σ and resistivity ρ, is not homogeneous but is different at different position within the sample. It is assumed that the conductivity is purely resistive.

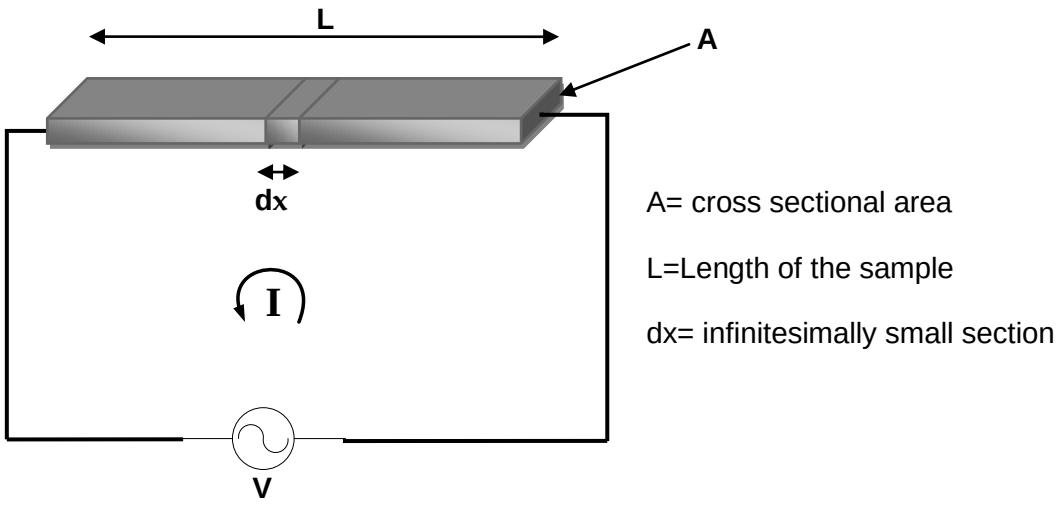

Figure 6. 11: schematic of the sample excitation

The material sample is connected with an A.C voltage source as shown in the diagram in figure 6.11. This results in a current **I** flowing in the circuit which relates to the source voltage **V** according to the Ohm's law. If we consider an infinitesimally small section **dx**, as shown in the diagram, in which the resistivity is assumed to be constant, then the resistance of this element **dR** can be expressed as below,

$$dR=\rho\frac{dx}{A}$$

According to Ohm's law, the voltage drop across dx can be expressed as

$$dV=I.dR$$

The current I is constant along the length branch.

$$dV=\rho\frac{dx}{A}I$$

$$dV=\frac{I}{A}\frac{1}{\sigma}dx \qquad \left(\because \rho=\frac{1}{\sigma}\right)$$

Hence, integrating the above equation over a small section x, with ΔV being the potential drop across x , we get the following expression:

$$\Delta V=\frac{I}{A\,\sigma}x \quad \text{, where } 0\le x\le L \text{ and } x\ll L \qquad (6.1)$$

Clearly equation 6.1 only holds for a very small section of the sample under test where the conductivity can be treated as constant. In actual practice, there are number of variables among which are the resistivity/conductivity is not constant as well as not purely resistive. It is a function of frequency as well as position because the sample is an inhomogeneous composite material.

6.3.2 Method

A block of carbon composite material, prepared by carefully compressing a number of carbon fibre sheets in epoxy resin potting compound, was used as a test sample. The potting compound was prepared by liquid epoxy resin and Araldite hardener [**92**]. An optical image of the actual material sample is shown in figure 6.12**.** Brass metal caps were bolted on the two ends, in order to establish a good uniform conductive block by aligning the conductive strands within the carbon reinforced material and making them in uniform contact with the metal cap. The area in red square shows the scanned section of the sample for which the results are presented further down the section.

Figure 6.13 represents the arrangement for exciting the carbon composite material by AC current of known magnitude and frequency. A known value of resistance was soldered with one end of the sample to maintain a non-zero potential at the rear end of the sample. In actual practice, the sample was mounted on a section of standard single sided FR4 PCB. The two metal cap ends were mounted on electrically isolated pad on the PCB. One end of the sample was connected to the signal generator input and the rest of the board was used as ground plane. The other end of the sample was joined by a resistor of approximately 50Ω down to ground.

The entire arrangement was placed on the XY table bed. The same XY table arrangement was used as described in section 5.2 in chapter five. The high impedance EPS was mounted directly above the carbon fibre sample and moved in a raster fashion at predefined steps, reading the level of RMS electric potential at each co-ordinate over the surface of sample. A LabVIEW VI was used to convert this RMS into corresponding DC level which was in turn used to plot a two-dimensional image of the detected electric potential with respect to X and Y position. The electric potential detected in this manner exhibit the material properties, predominantly due to the variation in the local conductivity.

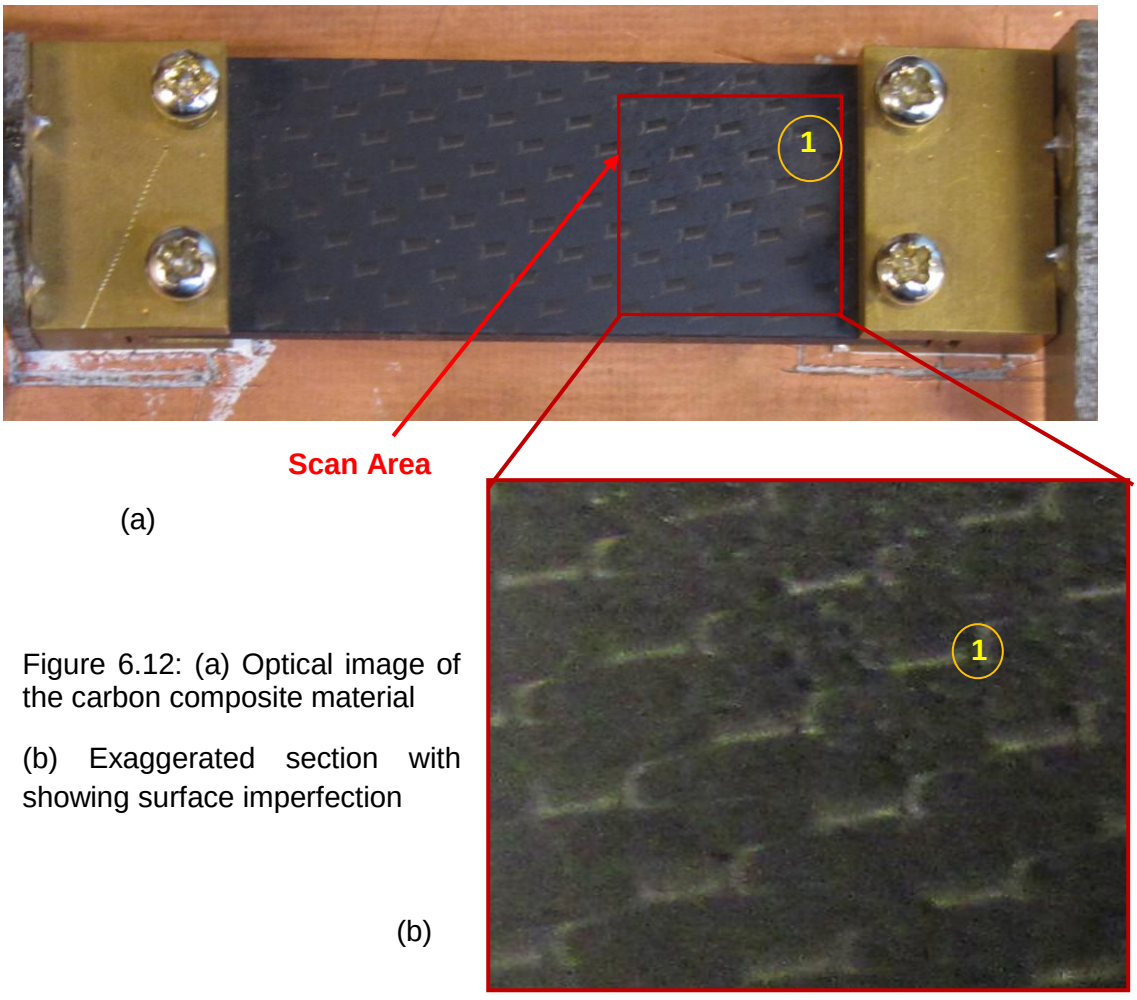

Figure 6.12: (a) Optical image of the carbon composite material

(b) Exaggerated section with showing surface imperfection

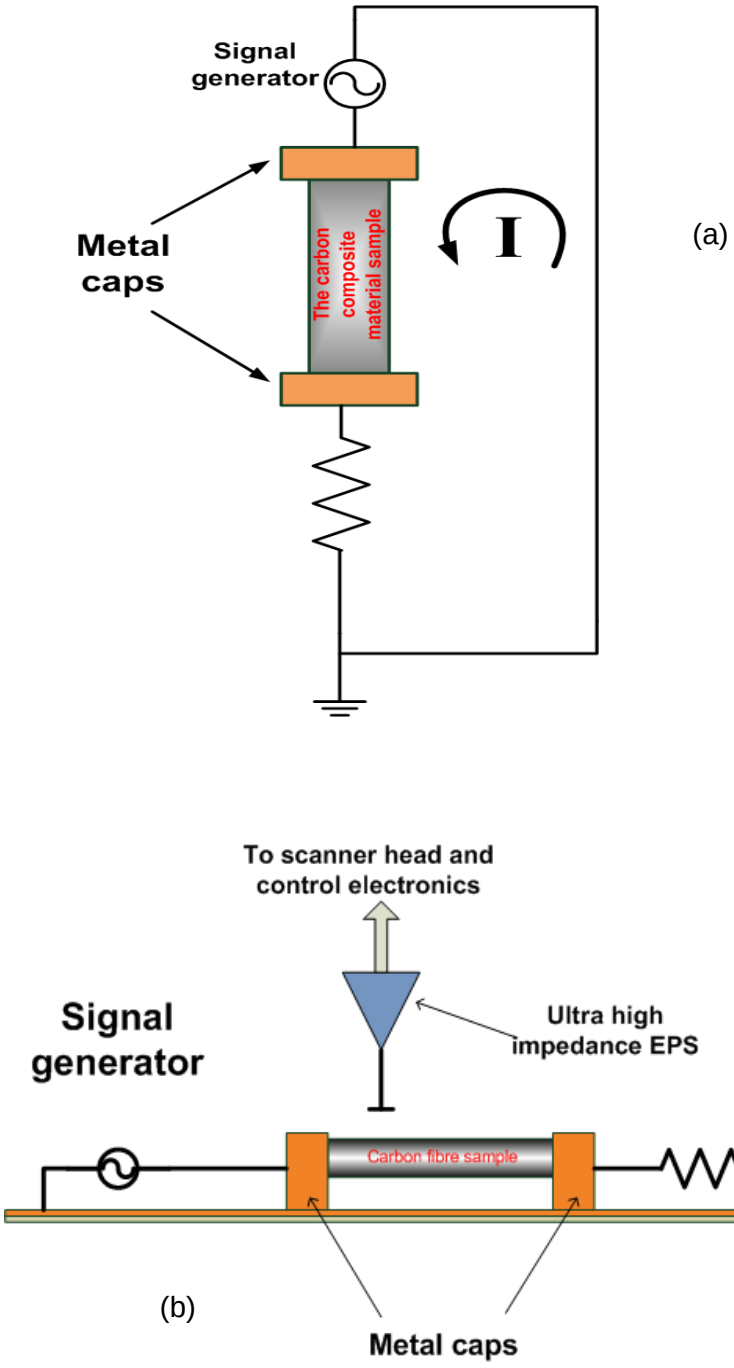

Figure 6. 13: Approximate experimental setup for sample excitation (a) as seen from the top (b) As seen in cross-section

6.3.3 Electrical characteristics of Carbon fibre sample

It is relevant to discuss the interaction of the current with the material since it was excited by A.C currents with a broad range of frequencies. The skin depth δ, measured from the surface towards the centre of the conductor, is defined as follows [**93**].

$$\delta = \frac{1}{\sqrt{\pi \, f \, \mu \, \sigma}} \tag{6.2}$$

This relationship describes the depth of penetration of an electromagnetic wave, in this case the injected current in a conductor as a function of frequency f, permeability μ and conductivity σ of the conductor. For a given conductor, the skin depth reduces with the increase in the frequency which means that the current density is higher near the surface of the conductor than it is in the centre. It is easy to calculate the skin depth for conductors for which the precise values of conductivity and permeability are known. In this case, the sample under test is a composite material of carbon mat and epoxy resin, with a number of such fabrics stuck together with liquid epoxy resin [**92**] hence the situation is not straight forward. The current that flows into the sample is faced by electrically dissimilar interfaces and goes through complex physical processes, in which the field lines and current vary according to the distribution of local electrical conductivities [**94**].

It will be seen in the discussions to follow, that the impedance of the material is a function of the frequency of the applied AC current, where the average impedance, over the entire sample area progressively become more and more inductive with frequency. Thus, the sample under test has the following characteristics:

(a) The electrical conductivity is anisotropic, where it is more conducting in the plane of fibres than between the layer [**14**]
(b) The impedance, measured over the entire sample, is strongly frequency dependent.

The frequency of the A.C currents used to excite the sample was varied from 10 KHz to 11 MHz. Figure 6.14 shows the variation of the complex impedance with respect to the frequency. The data points used for the plot were obtained by measuring the complex impedance of the carbon fibre sample using Hewlett Packard 4275A, a multi frequency L-C-R meter which was capable of measuring the same over discrete frequency values ranging from 10 KHz to 10 MHz [**95**]**.** As can be seen in the table 6.1, the variation in the impedance over this range of frequencies is rather broad, where the nature of the impedance goes from being almost purely resistive to almost purely inductive at the top end of the frequency. These vast variations in impedance affect the distribution of the electric potential within the sample at different excitation frequencies. For example, at 10 MHz, the magnitude of impedance in the system is 66.65 Ω which makes the RMS current in the circuit 106 mA. The nature of sample impedance being almost purely inductive means that it can be thought of as an inductor in series with a resistor of 48 Ω down to ground. At f = 10 MHz, the value of inductance of will be 297 nH ($\because L=\frac{X_L}{2\pi f}$), which makes it a low pass filter with a cut-off frequency of 25.7 MHz ($\because f=\frac{R}{2\pi L}$).

Frequency (in Hz)	Magnitude $\lvert Z \rvert$ (in Ohm)	Argument $\angle Z$ (in degree)	$\mathbf{I_{rms}}$ in the sample considering the 48 Ω resistor in series $\left(I_{rms} = \frac{V_{rms}}{\lvert Z \rvert} \right)$ (in mA)
10 K	234.5×10^{-3}	5.22	146.5
20 K	238.2×10^{-3}	10.07	146.5
40 K	250×10^{-3}	18.97	146.5
100 K	311.5×10^{-3}	39.38	143.3
200 K	461×10^{-3}	57.38	146
400 K	806.3×10^{-3}	70.98	144.8
1 M	1.884	80.92	141.7
2 M	3.686	84.73	136.7
4 M	7.272	86.83	128
10 M	18.65	88.10	106

Table 6.1: Complex impedance of the carbon fibre sample as measured by L-C-R meter

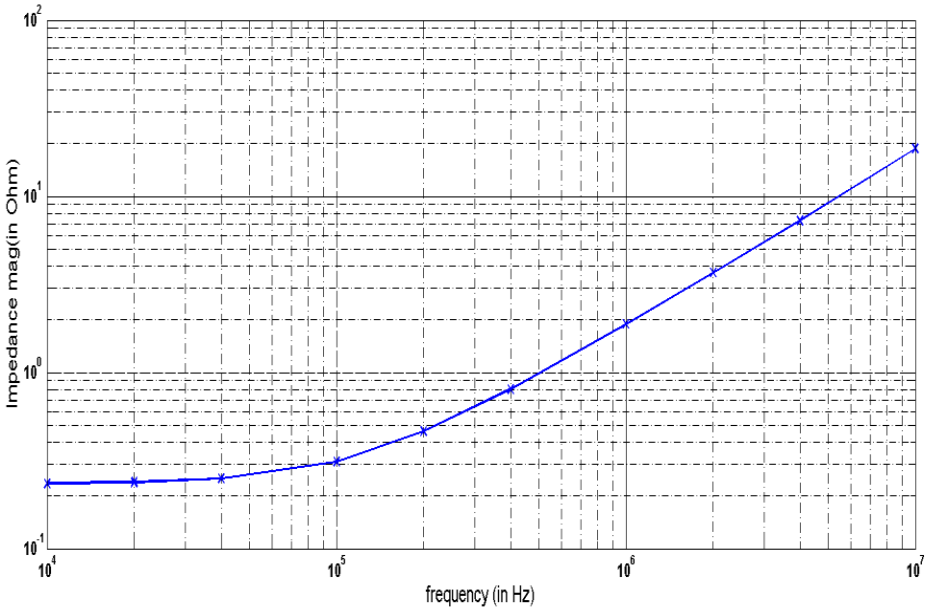

(a)

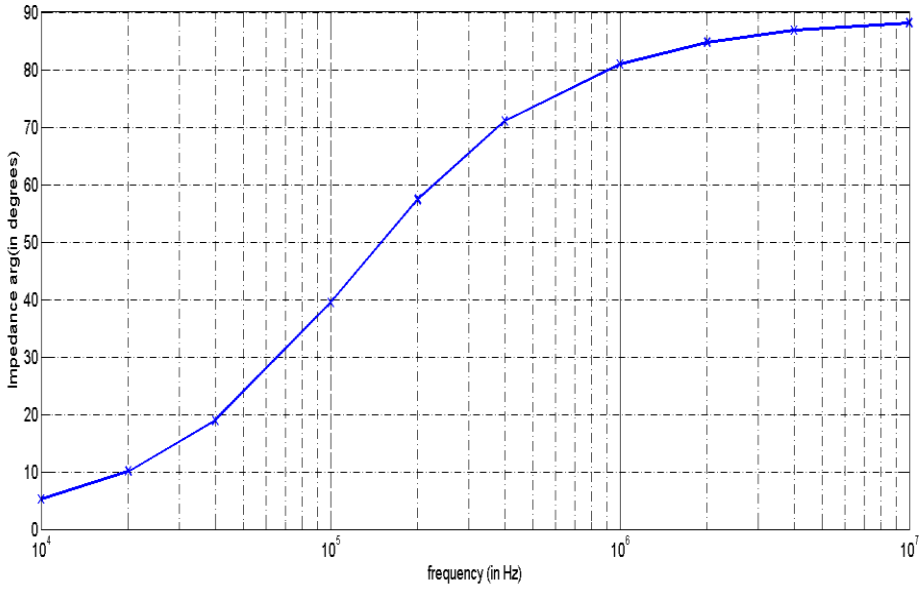

(b)

Figure 6.14 : (a) Magnitude and (b) Argument of the impedance of the carbon fibre sample as measured by using a standard L-C-R meter over a frequency range of 10 KHz to 10 MHz**.**

A more accurate analysis of the situation, in which a better estimation of the electrical components in the series R-L approximation of the sample test set up has been done, is plotted in figure 6.15. The complex impedance characteristic of the sample, presented in Table 6.1, in polar form ($Z = |Z| \angle \theta$) has been converted in rectangular form ($Z=R+jX_L$). The inductance has been calculated by only taking the reactive part at each frequency, using MATLAB. Figure 6.15 shows the resistive and inductive parts of the impedance as functions of frequency. At 4 MHz, the inductance is shows a dip in its value which is reflected on its cut-off frequency, as it depends on the resistive as well as the inductive components. An extrapolation of this situation suggest that the cut-off frequency of the system will progressively drop beyond 4 MHz, unless there is another inflexion in the value of the electrical component , the measurement of which is beyond the capability of the current impedance measuring instrument.

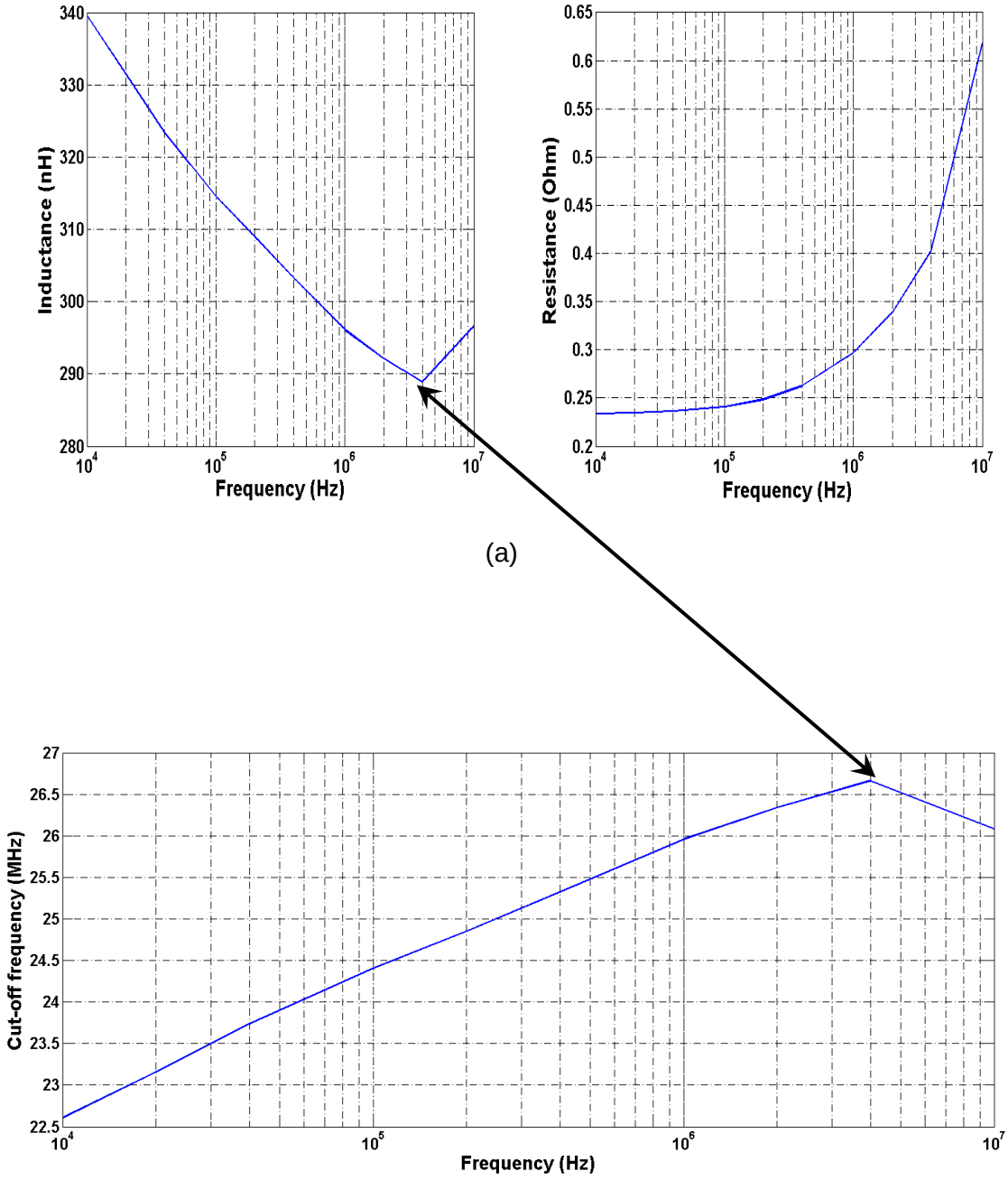

Figure 6.15: (a) R-L behaviour of the sample as function of frequency (b) Variation of cut-off frequency of the R-L circuit with excitation frequency

6.3.4 Results and Discussions

This section will discuss the results obtained from this measurement technique [**22**]. All the results show the distribution of amplitude of the A.C signal detected by the high impedance sensor as a function position. The dimension of the sense electrode at the EPS input was a semi rigid coaxial cable with inner and outer diameter of 200 µm and 50 µm, respectively. The sensor head was stepped at 63 µm step size over the sample, maintaining a constant working distance of 50 µm between the sample and the sensor.

It is important to note that the magnitude of RMS A.C current, injected into the sample, depends on the impedance of the sample, which in turn, is frequency dependent. The total impedance in all cases is the sum of the frequency dependent impedance of the sample and the 48 Ω resistor in series. Hence, the system is not a constant current source for all excitation frequencies. Table 6.1 shows the exact magnitude of RMS current corresponding to different frequencies of excitation.

A qualitative discussion of the data obtained in current injection mode is important before presenting the results. The measurement of local electric potential in the case of a sample that is excited by a current will incorporate a gradient in the background. In the case of a linear resistive element the background will have a straight line of fixed gradient which will depend on the magnitude of the source voltage. However, in the case of the sample under test, the situation is much more complex. The electrical properties have reactive components and their distribution is rather complicated. Figure 6.16 shows a possible simplified network of inductors and resistors which in the actual situation can be even more complex. The entire sample can be thought of as having multiple layers of such complex networks of electrical elements. As can be seen in the figure 6.16, there will be a potential drop between A and B (vertical) as well as A’ and A (Horizontal) when the source is connected between A and Z. This will introduce polynomial backgrounds of certain order depending on the nature of the impedances of the local elements in both X and Y directions.

The results include scans of different dimensions at different frequencies. The data collected by the system are plotted using open source data visualisation software, Gwyddion [**90**]. The polynomial background extraction feature within the software provides tools to subtract interactively, the background by approximating to the nearest best fit polynomial and removing it from the actual data. This dynamic control allows us to experimentally select the degree of polynomial background and subtract it from the data that gives the best visual improvement. Removing the background allows us to see small changes in the local conductivity within the sample. We present both images with and without the background extraction for the purpose of comparison.

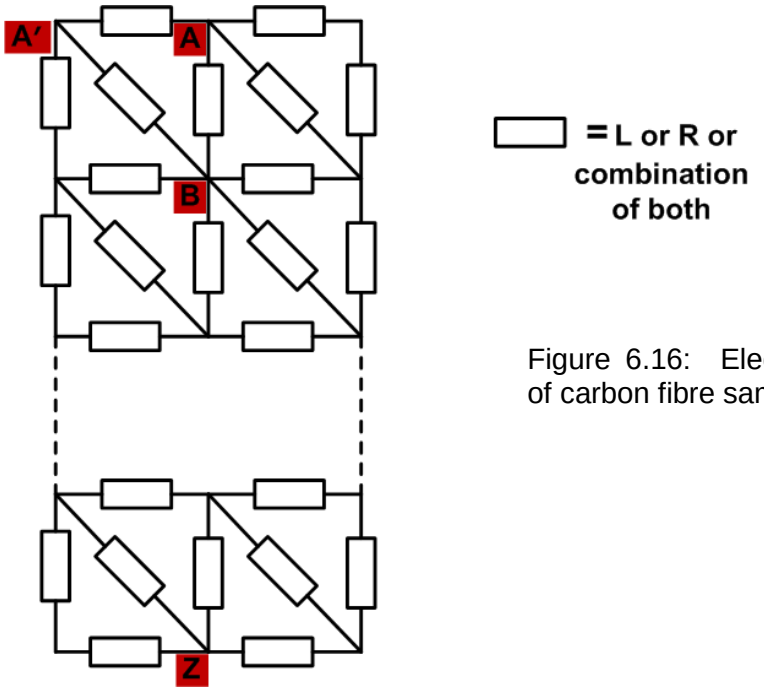

Figure 6.16: Electrical equivalent of carbon fibre sample

The sample was tested for excitation currents with frequencies at every decade, from 10 KHz to 11 MHz. By stepping the sensor head at 63 μm, 200 x200 data points of surface potentials were collected which corresponds to a total scan area of 12.6 mm x 12.6 mm over duration of 70 minutes. In figure 6.17(a), a scan result has been presented which was obtained by exciting the sample by

an A.C current of 10 KHz. The RMS amplitude of the current in the sample, as discussed before, depends on its frequency dependent impedance, which in this case is 146.5 mA (Table 6.1). Figure 6.17 (c) and (d) shows a line profile extracted from the data set along X and Y direction respectively. This has been done by selecting a row and column of the data in MATLAB and plotting them against X and Y positions. Incorporated in the plot are the polynomial fits which were selected by observing the best fit that closely approximates the data without distorting it significantly. Having known the degree of the polynomials in both directions, which in this case, are 8^{th} order in X direction and 10^{th} order in Y direction, they have been subtracted from the original data using the tool available in Gwyddion.

Figure 6.17(b) shows the background extracted image which exhibits a much improved contrast in the local conductivity variation of the scanned region of the sample. This sets up the procedure that has been used to improve the quality of data that have been obtained at other excitation frequencies.

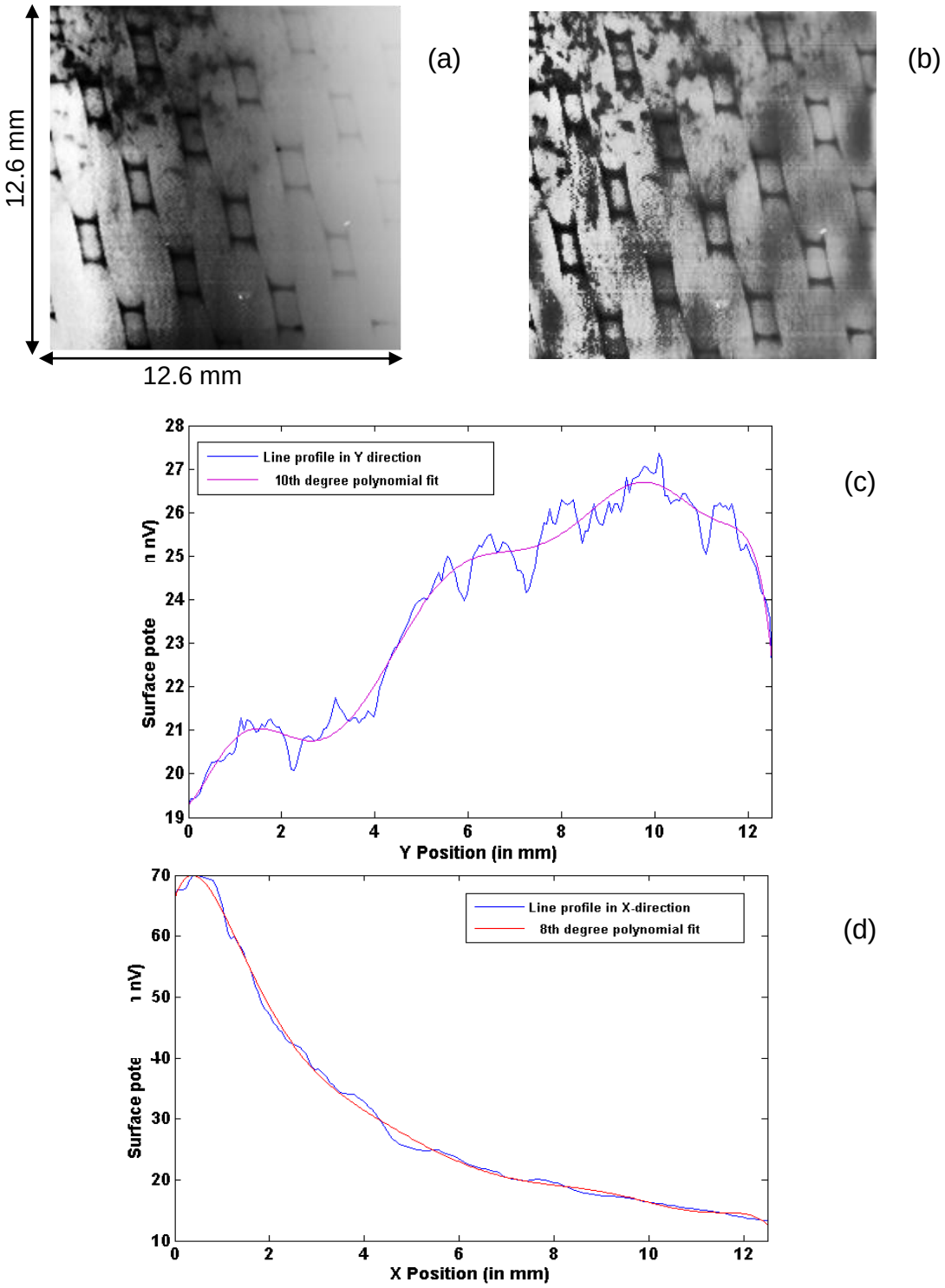

Figure 6.17: Electrical conductivity variation with position obtained at an excitation frequency of 10 KHz. (a) Original data from the sensor (b) Background subtracted version (c) Horizontal line profile and a polynomial fit (d) vertical line profile with a polynomial fit

Figure 6.18, 6.19 and 6.20 show scans of 12.6 mm x 12.6 mm section of the carbon fibre sample when the sample was excited by A.C current of frequencies 100 KHz, 1 MHz and 11 MHz, respectively. Each of them shows two images which correspond to the actual data set and background subtracted version of the same dataset. Similar inspections were carried out in deciding the order of polynomial backgrounds to be subtracted and it was established by the same method as discussed for the dataset obtained for 10 KHz, that the best fit was obtained for an 8^{th} order polynomial in X-direction and a 10^{th} order polynomial in the Y-direction. With the tool available in the data representation software, these backgrounds were removed and the clean data images are presented together with the original data obtained for each excitation frequencies.

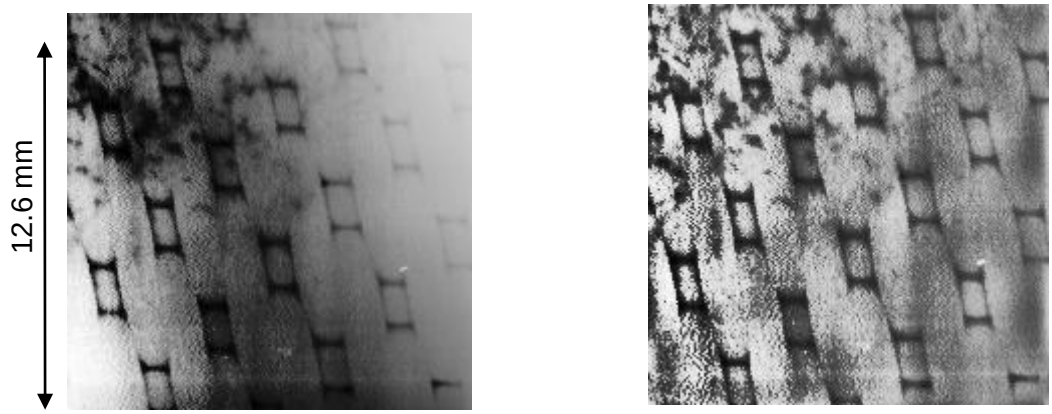

Figure 6.18: Electrical conductivity variation with position obtained at an excitation frequency of 100 KHz. (a) Original data from the sensor (b) Background subtracted version

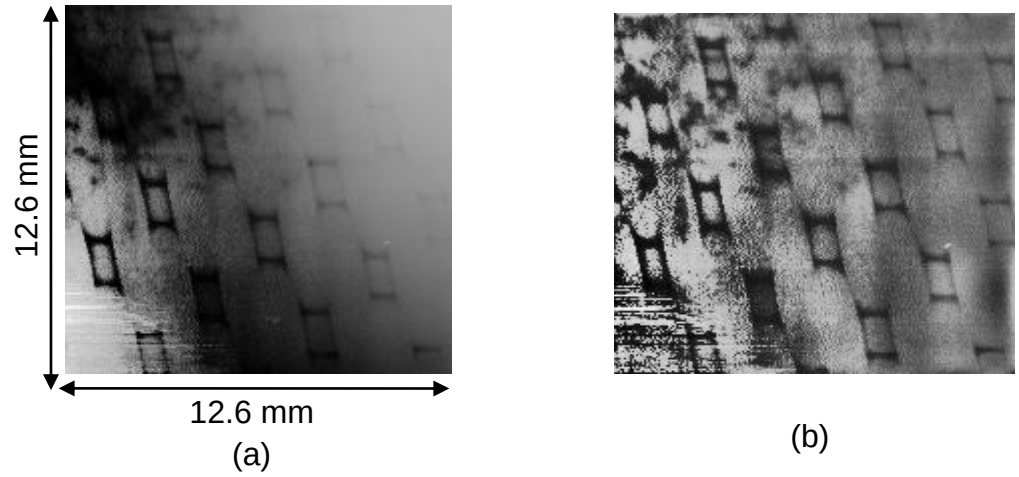

Figure 6.19: Electrical conductivity variation with position obtained at an excitation frequency of 1 MHz.(a) Original data from the sensor (b) Background subtracted version

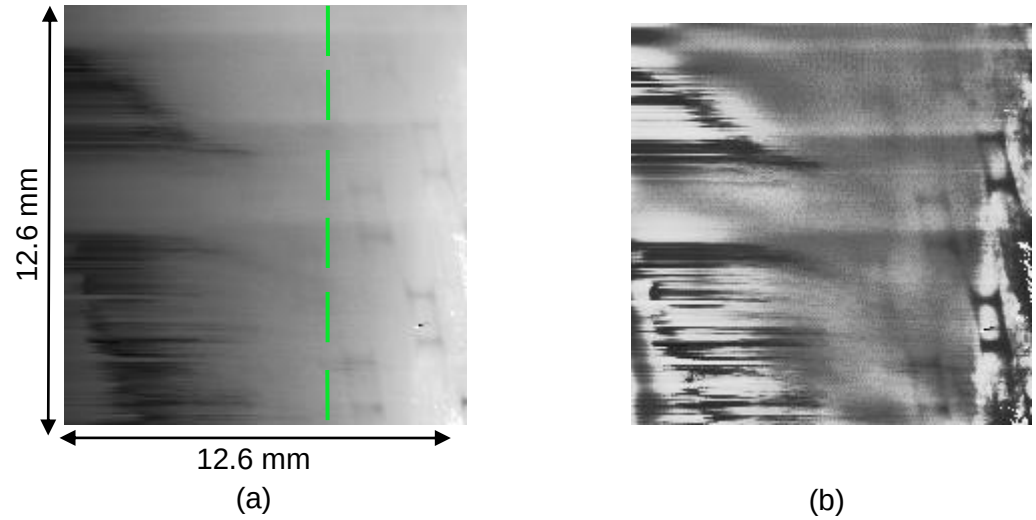

Figure 6.20: Electrical conductivity variation with position obtained at an excitation frequency of 11 MHz.(a) Original data from the sensor (b) Background subtracted version

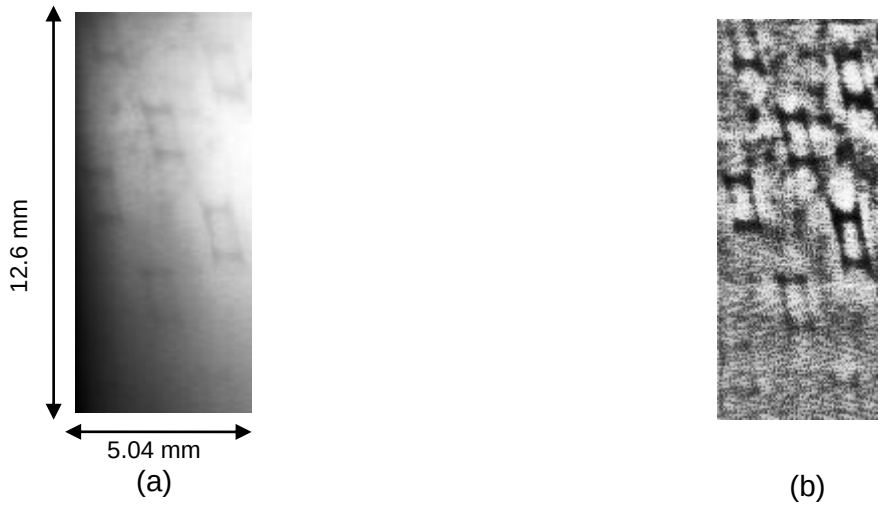

Figure 6.21: Electrical conductivity variation with respect to position obtained for a smaller section on a different region of the sample at an excitation frequency of 11 MHz (a) Original data from the sensor (b) Background subtracted version.

The effect of having processed the images is clear, with the contrast between the most and least conducting regions noticeably better. All the images show the material structure of the sample where the cross-ply structure of the carbon fibre, in the form of squares, is clearly visible. At the top left corner of the images, in figures 6.18, 6.19 and 6.20 a number of patches are also visible which refer to the magnified section shown in the optical image of the sample in figure 6.12. These random imperfections remained on the material surface which may have been due to two reasons. Inadvertent manual handling during the process of preparation, where a number of thin sheets of carbon fibres were compressed together, despite extreme care taken and possibility of physical contact between rigid sensor head and the material surface during the scan, although attempt had been made to keep the sensor to sample distance constant at about 50 μm. Nevertheless, from the measurement point of view it is good to be able to pick up these small imperfections which are greatly magnified in the electric potential images.

The left half of the image obtained by exciting the sample by 11 MHz AC current, presented in figure 6.20, is very noisy. However, to the right of the

green hatched line, the regular square cross ply structure is clearly visible even at 11 MHz. This attenuation in the signal detected by the high impedance EPS is due to the distribution of surface conductivity, which is dependent on frequency as well as the material composition within the sample. According to the measurement from the L-C-R meter, the average impedance across the sample is $18.65 \angle 88.1^\circ \Omega$ at 10 MHz. This also corresponds to a decrease of the value of current injected in the sample by about 30%, compared to the previous three cases. This is because the rate of increase of impedance is much faster for f > 1 MHz compared to low frequencies according to the Table 6.1. Clearly this is almost purely inductive at 10 MHz and it is certainly more so at 11 MHz, looking at the monotonically increasing nature of the dependence of impedance on the frequency from figure 6.14. This argument can be corroborated by the brief calculation presented earlier in this section where the system was shown to behave as a low pass filter at 10 MHz, with a frequency centred around 25 MHz. It should also be noted from the plot in figure 6.15 (b), the cut-off frequency of the L-R approximation of the system tend to drop beyond 4 MHz of excitation and at 11 MHz, it is likely to be around 25 MHz or lower which is only an octave away in frequency, hence it will attenuate the signal to a certain degree, depending on the type of roll-off.

However, because of the non-uniformity of the electrical properties within the sample, it is incorrect to conclude that the sample is a pure inductor at this frequency. The distribution of local conductivity is totally unknown and strictly depends on the composition of the material in the sample, which in this case is very complex. Figure 6.21 (a) shows another scan of a 5.04 mm x 12.6 mm section of the sample at 11 MHz in a different region and as can be seen the entire scan is free from noise and the regular square like feature of the material is easily visible. A background subtracted version of the same data is shown in figure 6.21(b), where the small variations are more visible. In this case, polynomials of 9th order in X-direction and 10th order in Y-direction have been subtracted as they closely approximated the original data.

Chapter 7

High Resolution CMOS Integrated Circuit Imaging

7.1 Introduction

EPS technology has been used to image digital circuits with a single sensor and micron level spatial resolution [**17**] [**18**]. Non-invasive imaging of digital circuits can reveal important information about the operation of the digital IC as it can indicate possible faults such as those related to signal integrity within the IC.

This section describes a passive, in situ, high resolution, imaging technique for investigating the internal structure of solid state CMOS chips while they are in operation using the broadband, ultra high impedance EPS. It is important to mention that this is the same broadband sensor which has been used to perform measurements described in chapter 5 and 6. Results show the detailed structure of the micro array structure on the silicon substrate within the solid state sensor. This technique can be used for the purpose of testing semiconductor ICs, possibly without disturbing their normal operation.

The sample used in this experiment is a Fujitsu MBF 200 solid state fingerprint sensor. The sensor is a standard CMOS chip with an active area of 12.8 mm x 15 mm. It is a 2-dimensional array of 256 x 300 metal electrode pixels with a passivation layer on top which acts as a dielectric. When placed in contact with a subject's finger, the metal electrodes pixels act as one plate of a capacitor and the finger, the other. In use, the capacitance of each pixel is measured and the data is then converted into a grey scale image in the form of a finger print [**96**]. The IC requires a microcontroller/ FPGA interface to make it operate under various applications.

A very important consideration in this experiment is the input capacitance of the EPS that is being used for the purpose of scanning. As we attempt to demonstrate a higher spatial resolution of the broadband sensor, we use smaller dimension of the sense electrode which is connected to the input of the EPS which couples the signal of interest. A smaller dimension of the probe also corresponds to weaker capacitive coupling and hence more signal attenuation. To ensure a measurable signal to noise, it is highly important to have an extremely low value of input capacitance of the EPS. This often requires careful design of the positive feedback, especially the guard feedback within the sensor electronics. Different dimensions of sense electrode tips were employed to probe the sample. The probe diameter was progressively reduced to achieve greater spatial resolution of scan.

7.2 Method

As shown in the diagram in figure 7.1, the EPS is mounted on the XY scanner which is interfaced to a PC over USB and its movement is programmed in LabVIEW. It is possible to set various parameters of the movement in both X and Y directions, such as scan step and dimension of the intended scan.

In this experiment, a standard Xilinx Spartan 3E development board has been interfaced with this chip. This is because one such board was available; any standard PIC microcontroller could have been used. For simplicity, the FPGA was programmed to switch on only one row of pixels, following a trigger pulse. The idea is to use the high input impedance EPS to scan across a small section of the chip and produce a 2-dimensional image of the micro structure of the metal electrode pixels inside the IC. In this case, this involves following a trigger pulse which is observable on a scope, one row of pixels are illuminated which means they are at a higher electric potential than the rest of the pixel array.

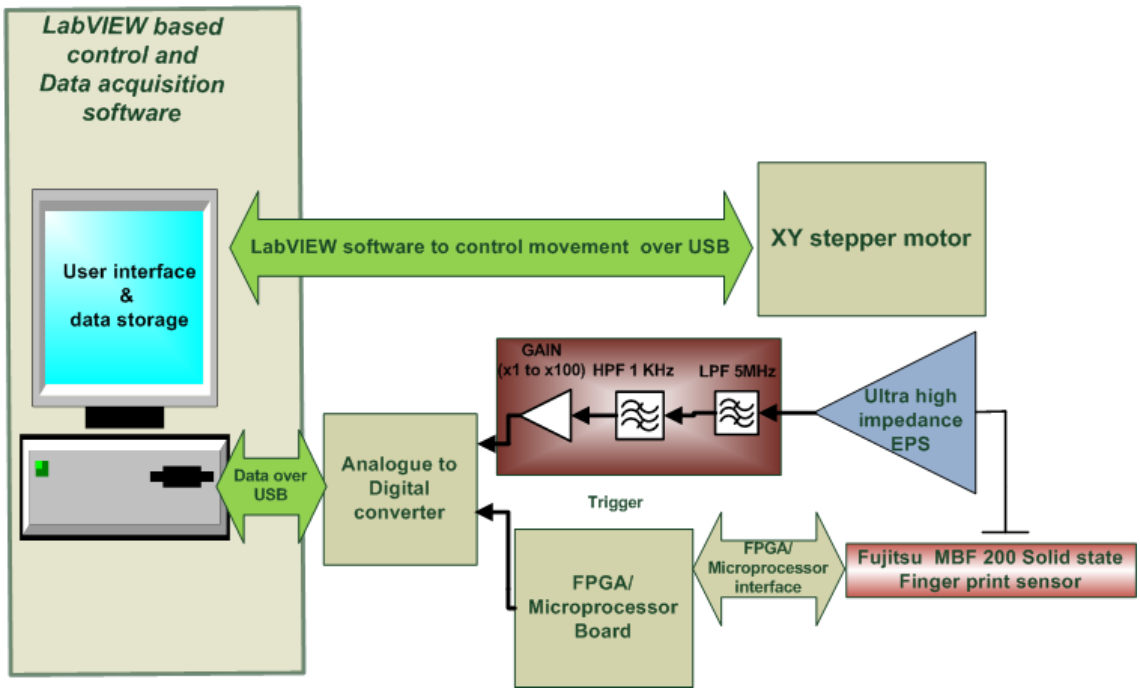

Figure 7.1: Overview of active sample scanning system

The EPS has a wideband response so it is important to introduce some electronic filtering down the chain to improve the signal to noise of the signal. A commercial Mini circuits inline coaxial low pass filter with a pass-band from DC to 5 MHz was used at the EPS output which was then fed to an 8^{th} order high pass filter centred at 1KHz and a variable gain BJT preamp before feeding to one channel of a 2-channel National Instruments USB digitizer (NI-5133). The other analogue input of the digitizer is used to trigger the acquisition. Figure 7.2 shows the signals that are fed to the two analogue channels of the digitizer. The yellow trace is the trigger pulse that is used to trigger the acquisition and the bottom blue trace the signal obtained by the electrometer after the signal processing steps described above when positioned directly over the pixels that are switched on.

The frequency band in the signal chain (1 KHz to 5 MHz) was chosen somewhat experimentally to ensure the signal is correctly measurable. The

datasheet of the fingerprint sensor describes the operation as follows. The metal electrode sensors connect to a fixed voltage to charge up to a certain value and then discharge through a current source after a certain discharge time. The voltages on each sensor plate at pre-charged and discharged are the measures of the capacitance of the sensor plate. The values such as discharge current and discharge time are not clearly documented.

A LabVIEW VI was developed to (a) set predefined scan areas depending on the probe dimensions and (b) acquire the amplitude of electric potential following the trigger pulse. As the scan was performed, data were acquired using the acquisition card. The data is simultaneously plotted to produce a two dimensional image of the amplitudes of the electric potentials with respect to the position.

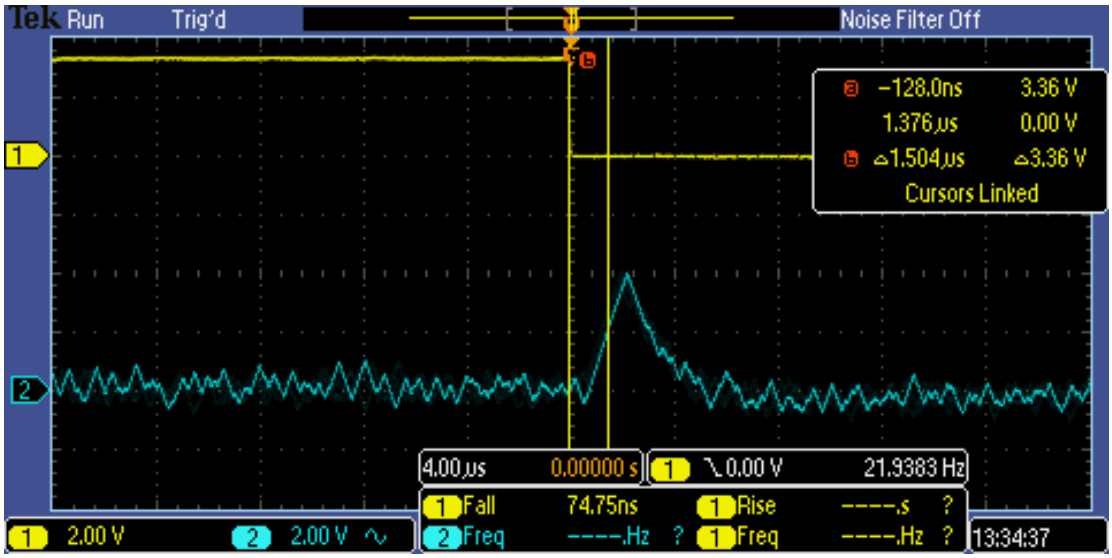

Figure 7.2: A screen shot of the traces as observed on Tektronix MSO 2024 digital oscilloscope. The yellow trace is the trigger pulse and the blue trace is the signal obtained directly from the EPS when positioned orthogonally above the active row of metal electrode pixels inside the IC.

7.3 Results

Several scans were performed using different probes to obtain images of different spatial resolutions. Figure 7.3 is obtained with an electrode with outer diameter of 1mm. It is a scan of a 3 mm x 3 mm area of the fingerprint sensor. This is an oversampled image with a rather coarse probe of 1 mm outer diameter stepped at 60µm. It is, however, a good starting point as the result quite clearly distinguishes the active row of pixels from the inactive ones.

Figure 7.4 is a 1.25 mm x 1.25 mm area over the fingerprint sensor with a finer electrode of outer diameter of 120µm. This image was produced by stepping the sensor head at 25 µm. This gives a better spatial resolution which is clear from the visual inspection as the illuminated pixels are more localised, suggesting greater detail in the position of the row of pixels within the chip.

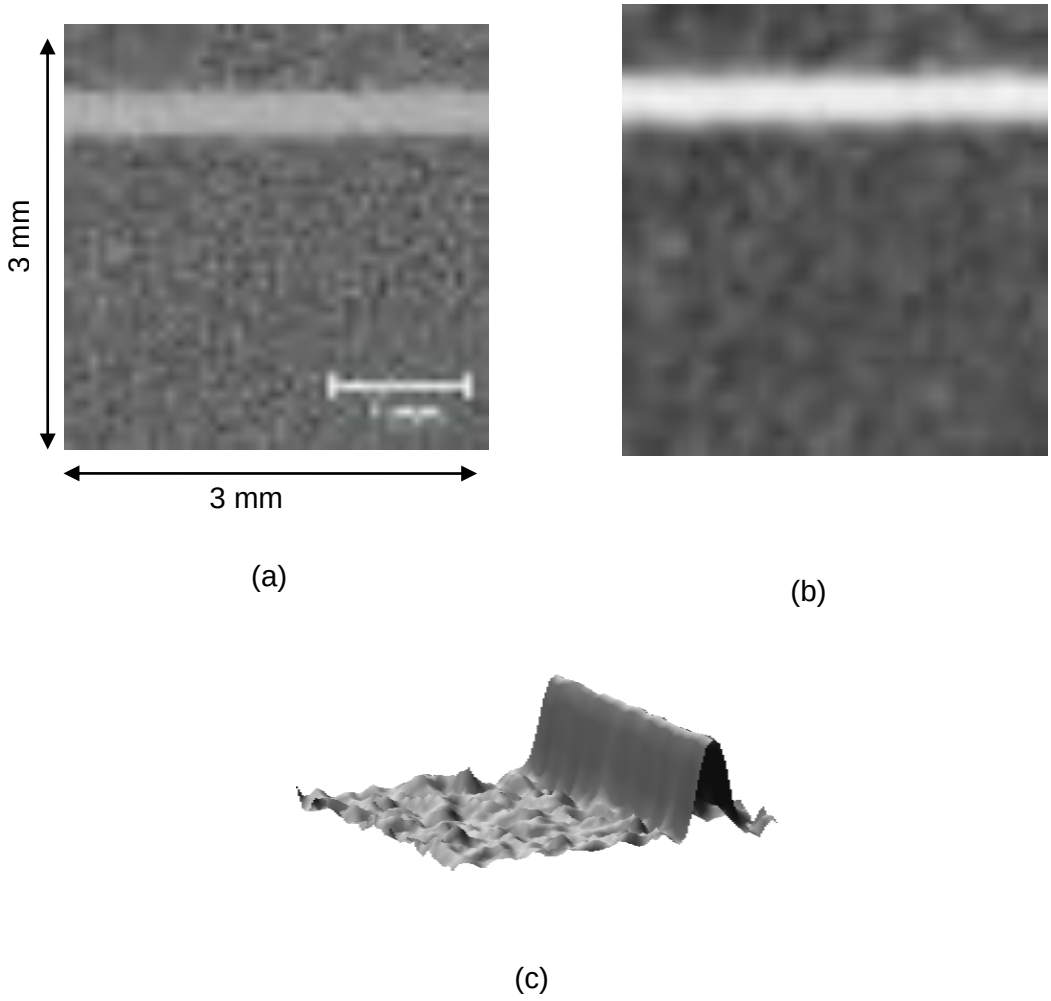

Figure 7.3: Image of the row of active metal electrode pixels inside the Fujitsu MBF 200 fingerprint IC. 50 x 50 data points measured at 60µm steps, measured with 1mm sense electrode, giving a total scan area of 3mm x 3mm. (a) 2D image of the data points as obtained from EPS (b) Image after software Gaussian blurring (c) 3D rendering of the data

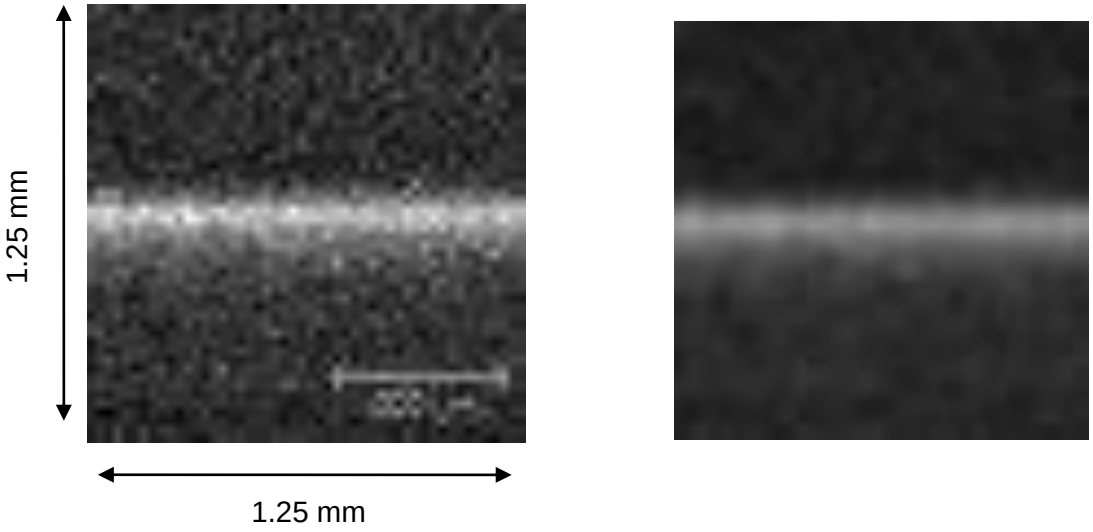

(a) (b)

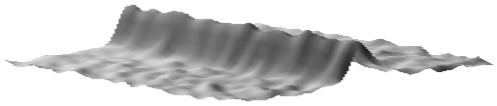

(c)

Figure 7.4: Image of the row of active metal electrode pixels inside the Fujitsu MBF 200 fingerprint IC. 50 x 50 data points measured at 25µm steps, measured with 60µm sense electrode, giving a total scan area of 1.25 mm x 1.25 mm. (a) 2D image of the data points as obtained from EPS (b) Image after software Gaussian blurring (c) 3D rendering of the data

To further enhance the resolution, an electrode of 5 µm diameter was used. This significantly weakens the source to sensor coupling capacitance. Therefore, suitable adjustment was made within the EP sensor feedback system to achieve a further reduction in the input capacitance. Figure 7.5 (a) and (b) show the actual sensor output and a filtered version of the same data in two dimensions respectively. To obtain this image, the step size of the sensor head was set to 6.3 µm, the smallest possible size on the XY system. Individual metal electrode pixels inside the fingerprint sensor IC are now becoming clearer with distinct, regular intervals between them. Figure 7.6 shows the 3D rendering of the same data which provides further detail about the data. The peaks correspond to individual metal electrode pixel in the microstructure array within the CMOS substrate of the solid state capacitive sensor IC.

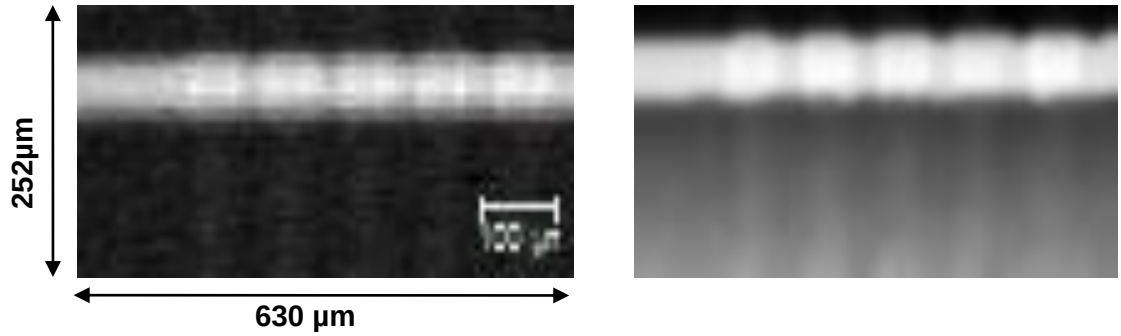

Figure 7.5: Image of the row of active metal electrode pixels inside the Fujitsu MBF 200 fingerprint IC. 100 x 40 data points measured at 6µm steps, measured with 5µm sense electrode, giving a total scan area of 630 µm x 252 µm. (a) 2D image of the data points as obtained from EPS (b) Image after software Gaussian blurring

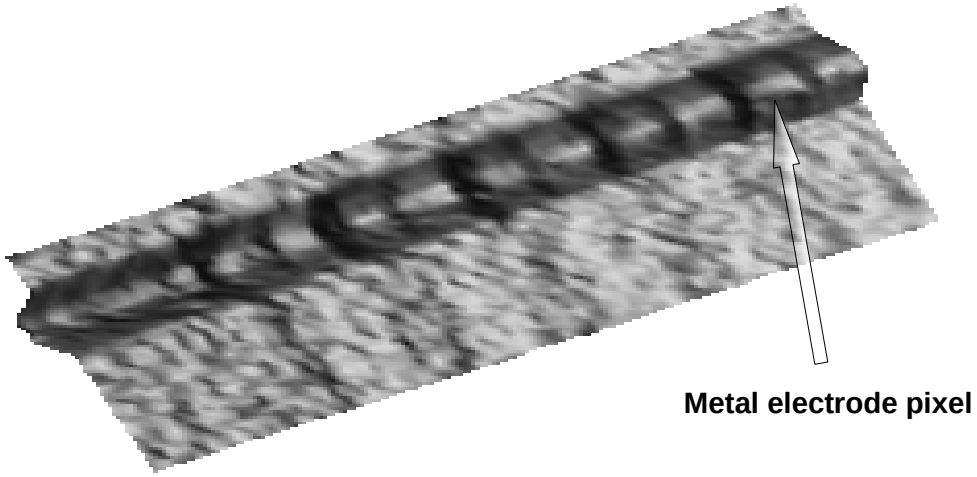

Figure 7.6: 3-D rendering of the data represented in figure 7.5. Individual metal electrode pixels are clearly visible

To further analyze the data presented in figure 7.5, a section of 80 x 22 dataset was extracted in MATLAB. A 2-Dimensional adaptive noise removal low-pass filtering was applied on the dataset. Wiener2 function, in MATLAB, uses pixel wise adaptive Wiener filtering, using predefined size of neighbourhoods to estimate local image mean and standard deviation. Following is the MATLAB command used to obtain the image presented in figure 7.7.

j=wiener2 (newdata, [25 2]); imagesc(j)

Here *j* is a local variable and *newdata* is the 80 x 22 extracted dataset from the original dataset with a size of 100 x 40. The numbers inside the brackets, [25 2] is the neighbourhood size, that the function uses to obtain local statistical information while applying Wiener method to the dataset. Imagesc is a MATLAB function that can be used to display the image data by scaling the data to use full colormap.

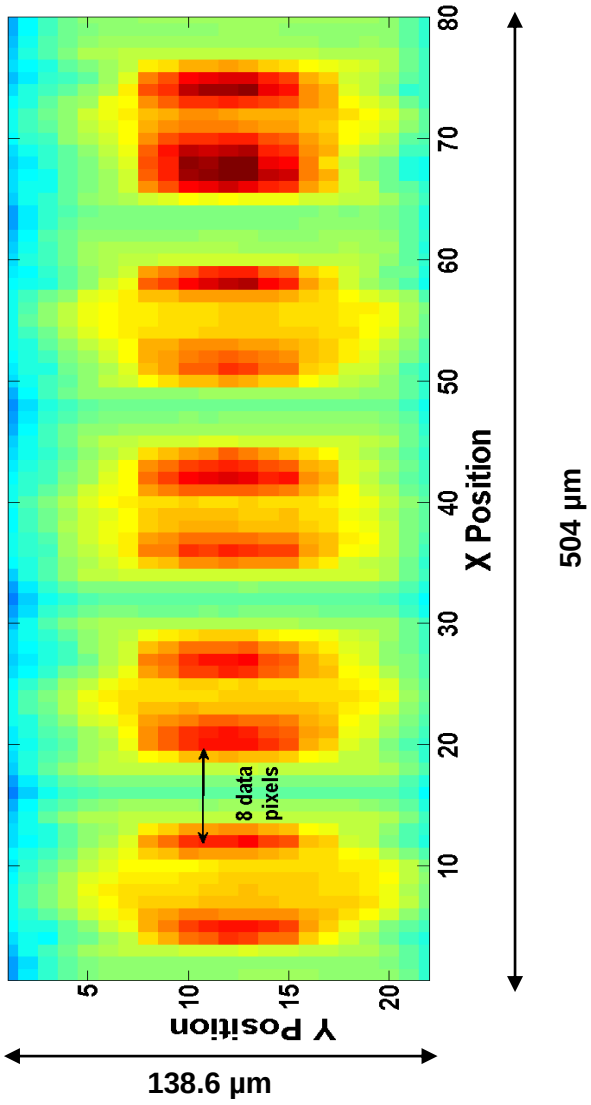

Figure 7. 7: Image of 80 x 22 data points extracted from the 100 x 40 data image presented in figure 7.5 after Wiener filtering and plotting in MATLAB using full colour map.

The X and Y positions are represented in terms of data pixels, not to be confused with metal electrode pixels within the IC sample. The image plot presented in figure 7.7 has 80 data pixels in the X direction and 22 data pixels in Y direction. Individual data pixels are 6.3µm apart which gives the physical dimensions of 504 µm x 138.6 µm for the image plot.

The red patches appear at regular intervals, correspond to individual metal electrode pixel in the microstructure array inside the IC. Two consecutive red patches are approximately 8 data pixels apart which translate into a physical separation of 50.4µm. This is in very good agreement with the datasheet of Fujitsu MBF 200 which suggests a pixel pitch of 50 µm for the micro structure array of metal electrode pixels.

Chapter 8

Conclusions

The aim of this thesis was to extend the operational frequency of the EPS towards the RF region. Having done so, it was applied to various broadband applications. Two major areas have been investigated; the electric field acquisition of the Nuclear Quadrupole Resonance (NQR) signal; and high resolution, broadband scanning microscopy for material characterisation and integrated circuit imaging.

The NQR experiment is a proof of principle study which demonstrates that the electric field component associated with the precessing magnetisation vector can be measured. Previous work on EPS has shown this effect for a Glycerin sample in an NMR experiment conducted at 2 MHz. In this thesis, the aim was to demonstrate detection of the electric field component at a higher RF frequency and for a different form of a magnetic resonance system i.e. NQR. The advantages of this method is that the cross coupling between the sense electrode of the sensor and the inductive coil is much less compared with the traditional method, which utilises coils to both excite and receive the signal. Another useful advantage of using EPS in magnetic resonance systems is that the same sensor can be used for multi nuclei detection due to the inherent broadband response of such a sensor.

EPS technology has also been used as the probe head of a scanning microscopy system, for imaging integrated circuits and characterising electrical properties of various materials. In all previous such applications of EPS, the scan has been either with micron level resolution but at a single audio frequency or broadband but with coarser resolution. In this thesis, a single sensor, capable of working at spatial resolution of 5 μm and also broadband over a frequency up to 200 MHz, has been described.

Chapter two described the principle of operation of the EPS and the various design stages which led to the development of the broadband EPS. The circuitry mainly includes FET input op-amps with very high gain bandwidth products, high input resistance, relatively low input capacitance and low voltage noise. Using positive feedback techniques like bootstrapping and guarding, the input resistance and input capacitance values were further improved over the intrinsic values. It is now possible to have a single sensor with an operable bandwidth of less than 10 KHz to more than 200 MHz. Various tests and characterisations have been carried out which are also described in the same chapter. The final version of the sensor designed in this manner was characterised for an input resistance of 15 GΩ, input capacitance of 0.5 pF, voltage noise of 16 nV/√Hz and working bandwidth of 10 KHz to 200 MHz.

An understanding of the principles of NQR was essential and therefore discussed in chapter three with reference to a continuous wave NQR experiment for sodium chlorate. The continuous wave method incorporates a marginal oscillator and a mechanism for varying the frequency of excitation in the region of NQR frequency .The characteristic RF absorption by the sample, placed in a tank circuit which forms part of the marginal oscillator, is picked up by the sensitive oscillator. This conventional system was set up, followed by the introduction of the capacitively coupled EPS. The results obtained in this section show simultaneously, the magnetic component of the signal detected by the pickup coil as well as the electric component, detected by the EPS.

A more sophisticated, pulsed NQR experiment has been described in chapter four. This system incorporates a pulse generator which can gate the RF at the correct frequency and amplify the pulse by using a power amplifier. This RF burst is used to perturb the sample placed in a tank circuit. After the pulse, a relatively weak free induction decay signal results which is traditionally measured by reading the magnetic component. The EPS has been used to acquire the electric field component of the same signal for sodium chlorate at 30 MHz. A superheterodyne receiver system has been used here for narrow band reception. A number of tests were performed to establish that the signal was due to the sample and was not spurious. The frequency of excitation and the power levels were varied by using a LabVIEW VI which did so automatically

through a remotely interfaced signal generator. This process was repeated with the tube containing the dry sodium chlorate sample in the test rig and also when replaced by an empty glass tube. The results shown demonstrate the substantial change in the signal at the NQR frequency and corresponding to a particular power level when the test rig contained the sample.

For the second major application of the broadband EPS, a surface scanning microscope with the broadband sensor as probe head has been employed to perform a surface topography scan. Chapter five described involved an XYZ scanning system with stepper motor controlled stages, which allowed variable scanning parameters such as the step size and scan area. A conducting sample was used which was excited by an AC voltage of known amplitude and frequency. Scans were performed with the sensor tip at a fixed height over the sample in a raster fashion to measure the electric potential above the sample surface. Data was collected at fixed steps over a two dimensional area. This data was used to provide the surface topography information which mainly distinguished the equipotential regions on the raised parts of the surface, due to the conductors being at the same AC potential from the rest. This preliminary experiment demonstrated that the system could operate over a frequency range of 10 KHz to 20 MHz and with spatial resolution of 100 μm.

In chapter six, two different composite material samples; an FR4 dielectric and a carbon fibre based material, were used to measure the local variation in their electrical properties. Scans were performed with a 100 μm tip, over a frequency range of 10 KHz to 11 MHz. The results show the variation of dielectric constant and conductivity as a function of position as well as frequency. The ability to measure small variations in the local electrical properties can be utilised in the material testing applications in which water/ air ingress in composite dielectrics and buried defects within carbon fibre composites are among the immediate ones. Both of these applications are non-contact and non-destructive, extending their potential application as in-situ testing with the relevant control mechanism.

A CMOS Integrated Circuit (IC) was chosen as the sample to demonstrate an even higher resolution scan described for active sample in chapter seven. The sample is a CMOS solid state finger print scanner IC which encapsulates a high

density array of metal electrode pixels with a 50 μm pitch. One row of pixels within the IC was programmatically activated and a 5 μm probe was used to scan a small section on the surface. A scan of the area around the row of active pixels reveals the internal structure of the IC in which individual pixels can be clearly seen.

The flexibility in the spatial resolution is an attractive property of this type of scanning microscopy system. For example, a larger physical size of the sample may be initially tested with a relatively coarse spatial resolution for a quick scan, followed by a finer resolution scan around the affected area. This process may be reiterated to the minimum allowable scan resolution giving maximum knowledge of the defect within the test sample.

A broadband design of the sensor has many applications, especially now that operation at the RF frequencies has been demonstrated. Op-amps have been traditionally used to build these sensors and this has been extended in this thesis to higher frequencies. The op-amps with very high gain bandwidth product, high common mode resistance, low input capacitance, low noise and relatively low input bias current are commercially available. However, having these parameters optimised for all frequencies is challenging. The design presented in this thesis already pushes these limits with the commercially available options. Nevertheless, certain aspects can be improved in future designs. The ADA 4817 has been found to have a lower value of input capacitance and voltage noise compared to OPA 656 which was primarily used in this thesis because of availability. This comparison actually suggests a better high frequency design with the former because a lower input capacitance takes priority for input parameters at higher frequencies (capacitive reactance being inversely proportional to frequency).

A lower input capacitance is also the key to high spatial resolution. Discrete FET circuits can often give better low capacitance designs, especially when configured in a cascode configuration, for example with a dual gate MOSFET.

Potentially these designs can be produced in one or two dimensional, high density arrays on silicon which would significantly improve the sensor

performance in various applications. It may be possible to apply the sensor array for real time NMR and NQR imagining. The material testing and characterisation applications will require much less time with a two-dimensional sensor array as compared to the single sensor scan described in this thesis.

Overall, this thesis explores sensor design in the broadband RF region and applies this to proof of principle study of electric field NQR and non-destructive, high resolution, broadband material characterisation. Clearly, these sensors can be used in a number of other applications including NMR and other forms of magnetic resonance such as Electron Spin Resonance (ESR) which generally requires a higher operating frequency but still within the EPS bandwidth. Material characterisation applications can be performed at even higher frequencies than those described in this thesis, with access to faster digitizers, and at higher spatial resolution, with electrodes produced using micro-fabrication techniques. Imaging digital circuits with fast pulses, of the order of hundreds of megahertz and with short rise times and with higher spatial resolution is also now a feasible application.

APPENDIX A

A.1 Positive feedback network in a standard EPS

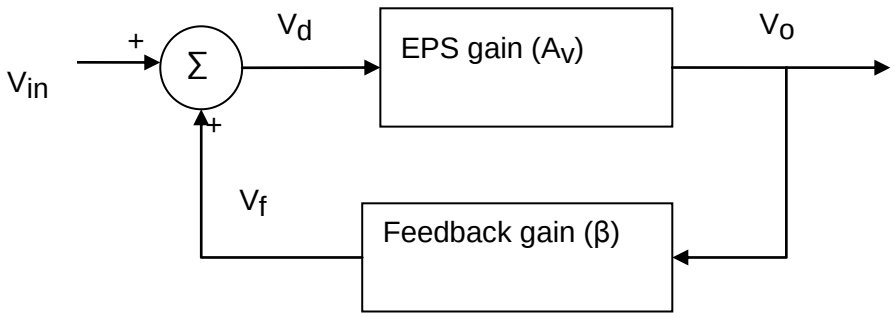

Figure A.1 : Block diagram of a positive feedback network in a standard EPS

Figure A.1 shows a block diagram of a standard EPS with positive feedback network which is a combination of different types of positive feedback discussed in detail in chapter 2. A_v denotes gain of the EPS and β denotes the gain of the feedback network which depends on the amount of signal being fed back. The more the value of feedback signal V_f the less the β.

It is clear from the block diagram in figure A.1 that

$$v_d = v_{in} + v_f \tag{A.1}$$

$$v_o = A_v\ v_d \tag{A.2a}$$

$$v_f = \beta\, v_o \tag{A.2b}$$

Using equations (A.2a) and (A.2b) in (A.1), we get

`

$$\frac{v_o}{A_v} = v_{in} + \beta v_o$$

Hence,

$$\frac{v_o}{v_{in}} = \frac{A_v}{1 - A_v\, \beta} \tag{A.3}$$

Equation (A.3) suggests that if $A_v \beta = 1$, the gain of the circuit becomes infinite. Expressing the same in the polar form we get,

$$A_v \beta = 1 \angle 0^o \text{ or } 360^o \tag{A.4}$$

This suggests that if the feedback gain becomes reciprocal to the EPS gain and is in phase with the input signal it results in a sustained oscillation.

APPENDIX B

LabVIEW VIs

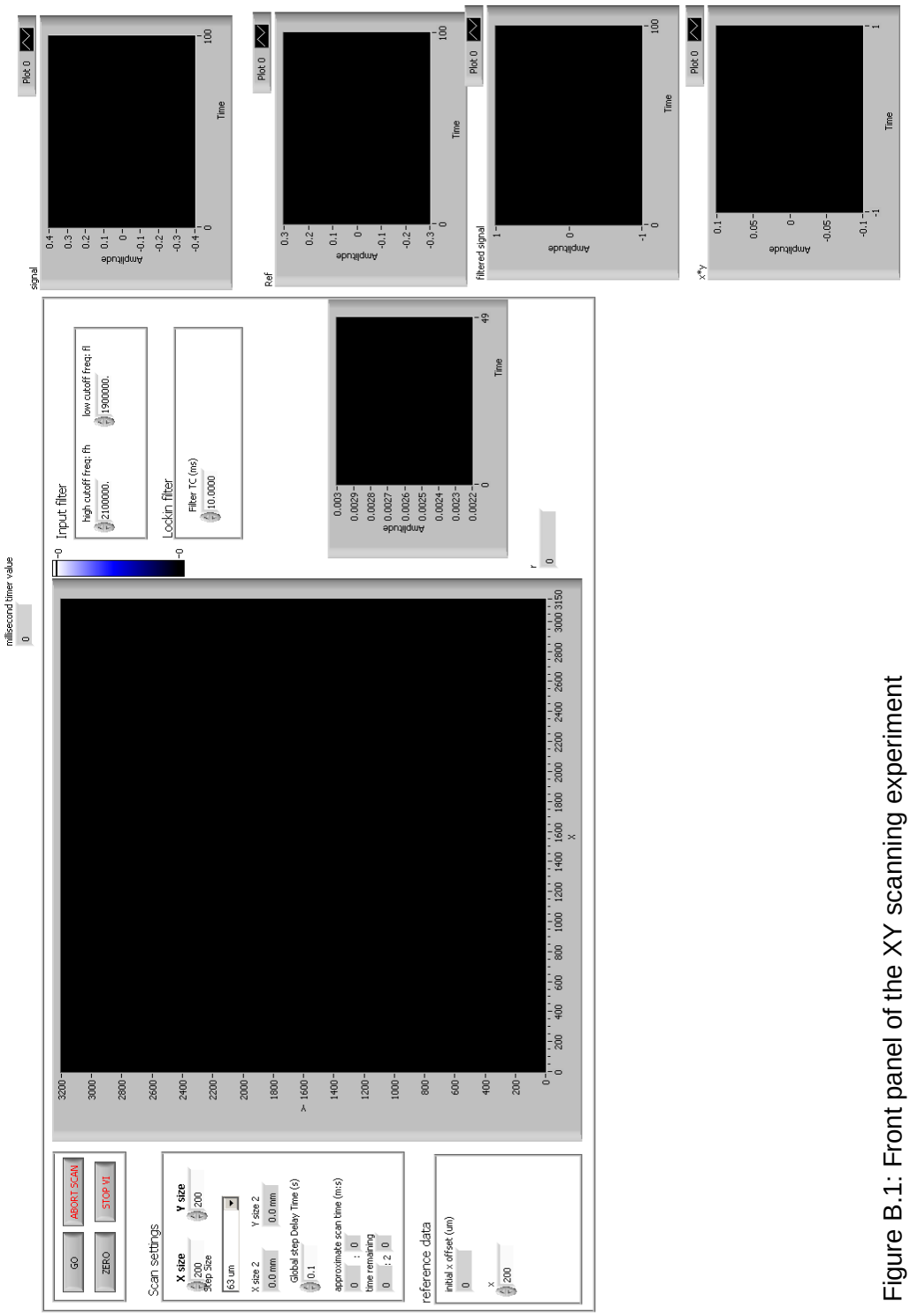

Figure B.1: Front panel of the XY scanning experiment

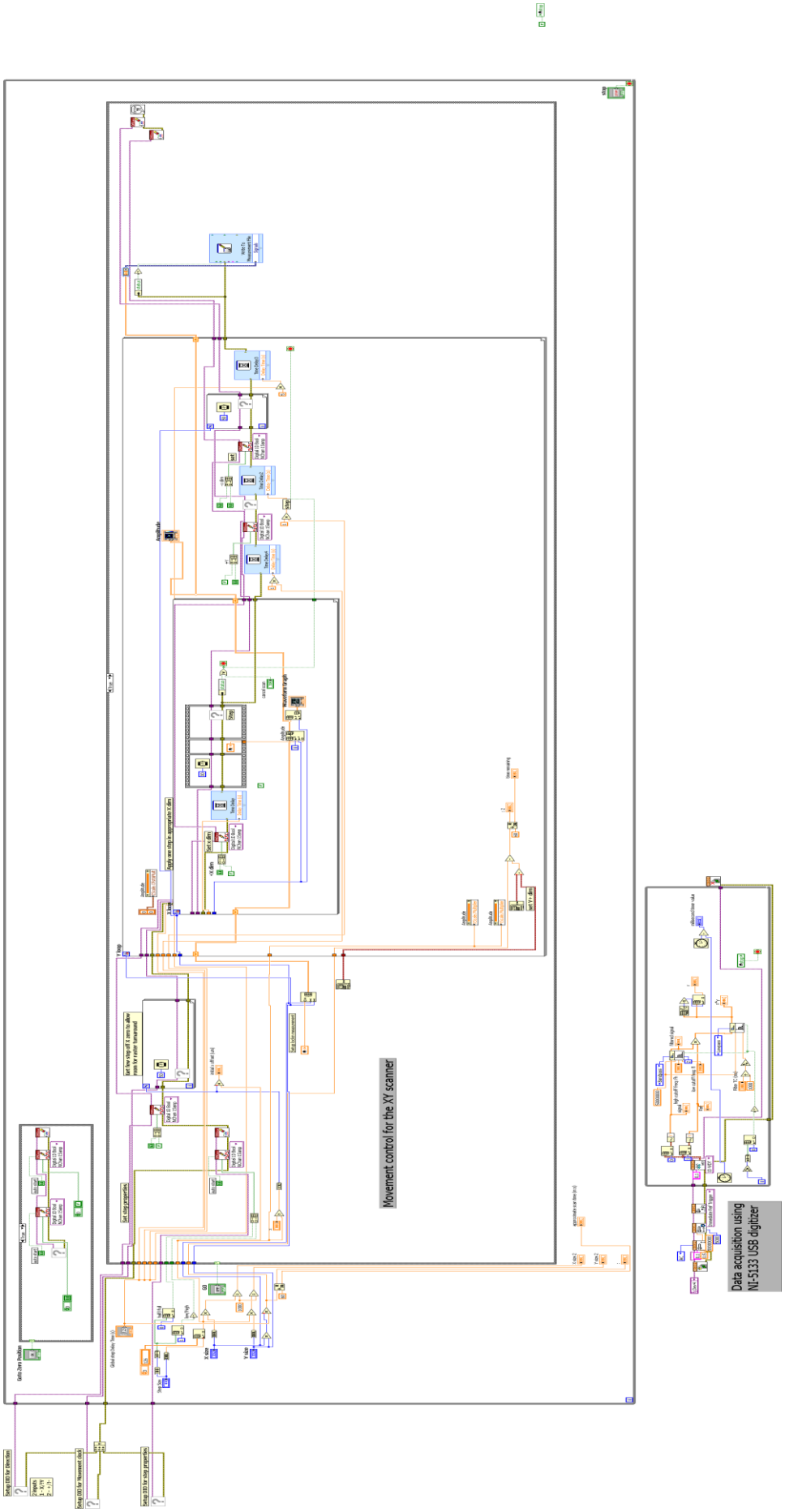

Figure B.2: Block diagram of the XY scanning experiment

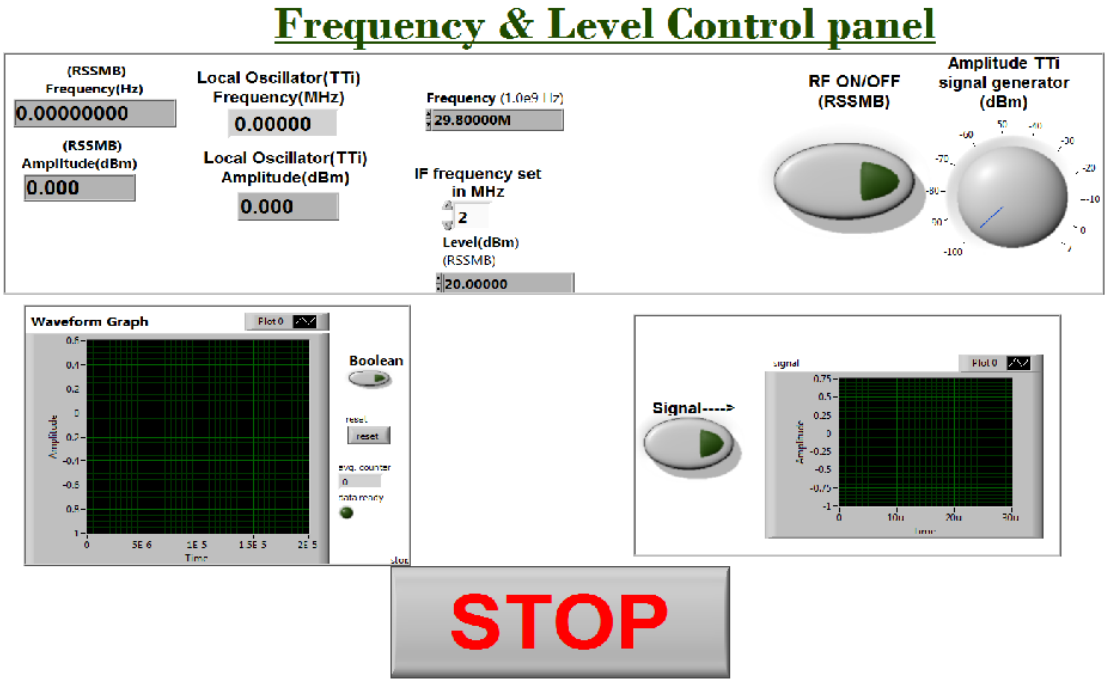

Figure B.3: Front panel of the Pulsed NQR data acquisition system

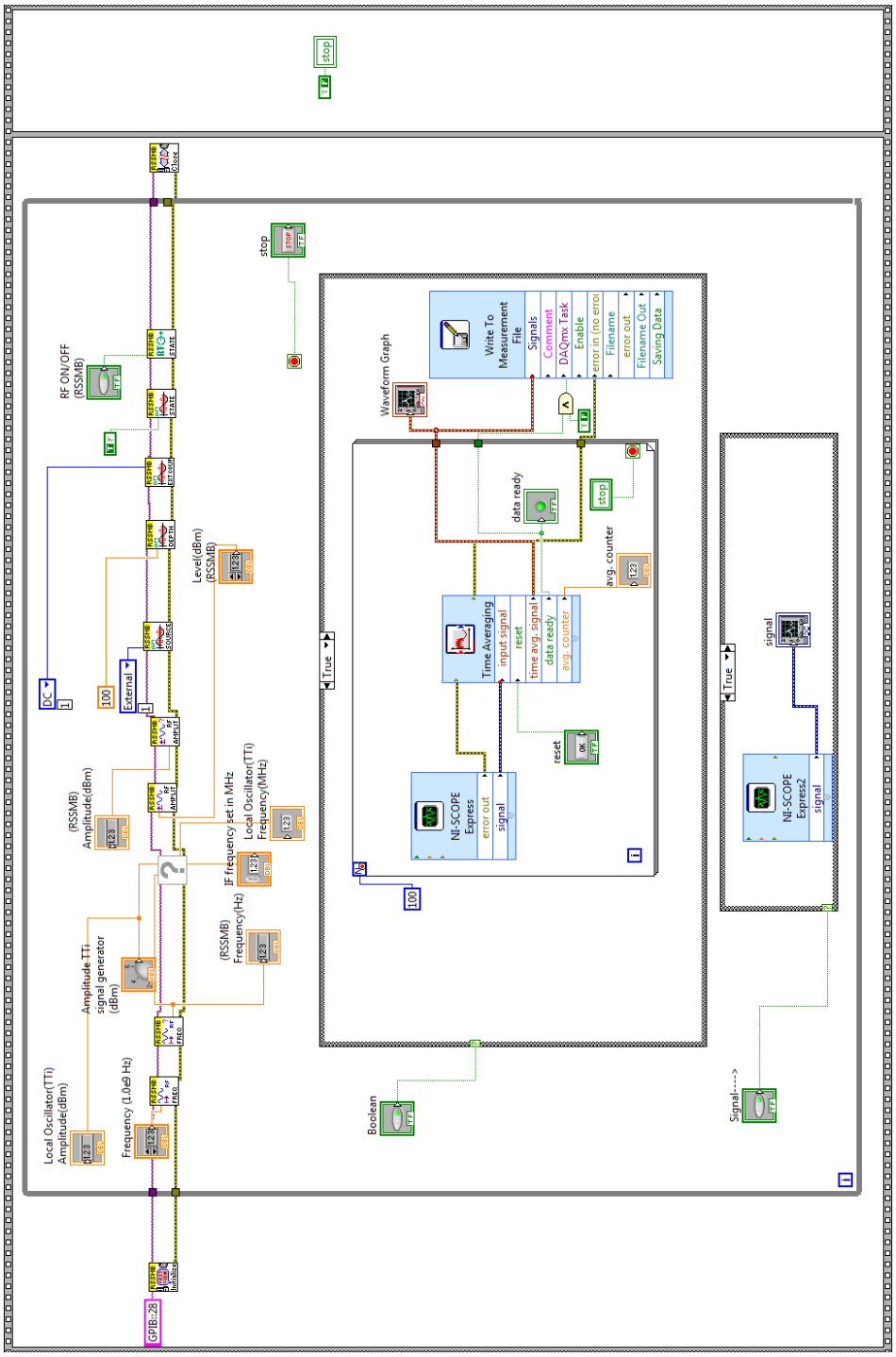

Figure B.4: Block diagram of Pulsed NQR data acquisition system

APPENDIX C

Pulsed NQR transmitter

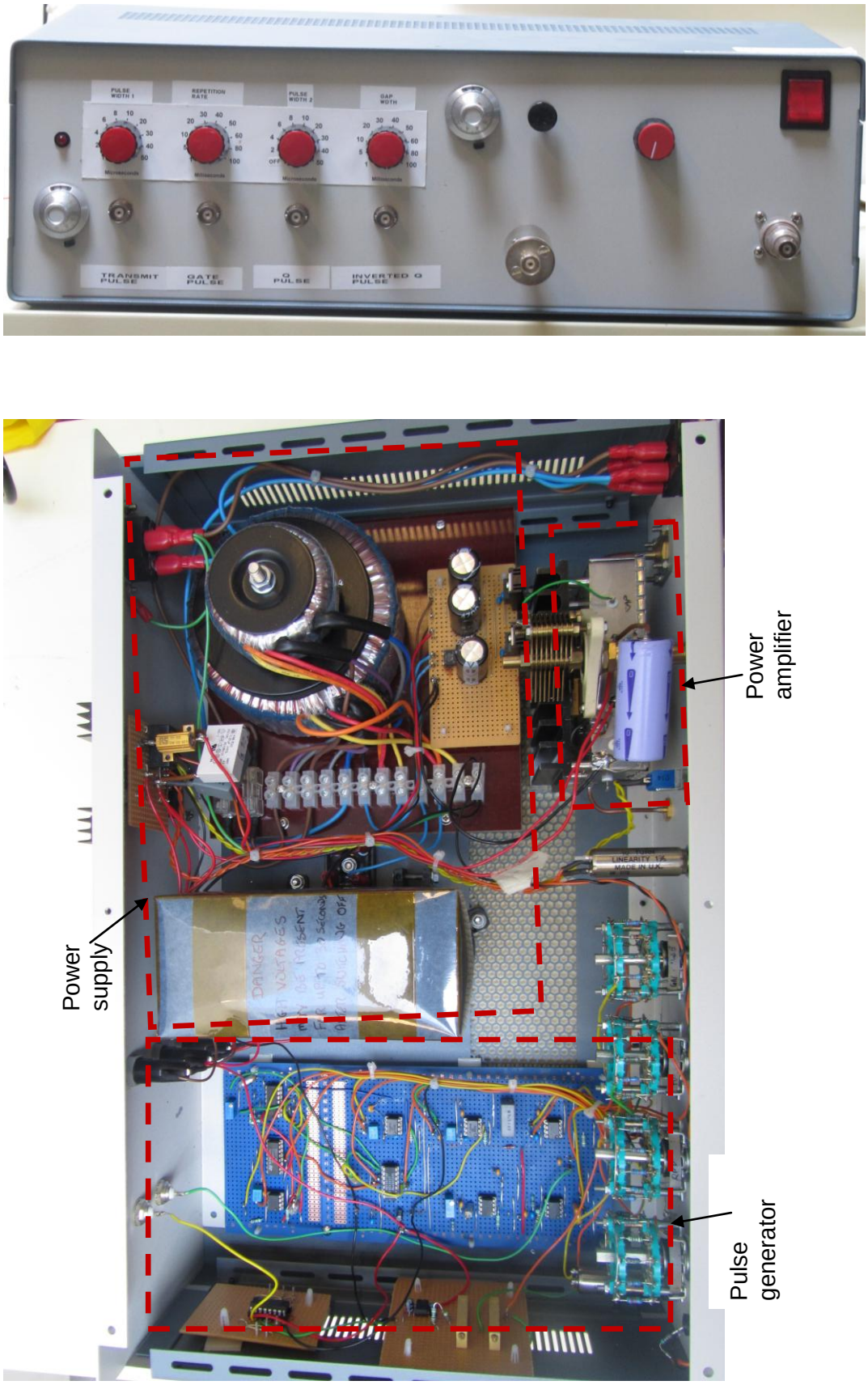

Figure C.1: The physical arrangement in which the pulse generator, RF power amplifier and the power supply were placed

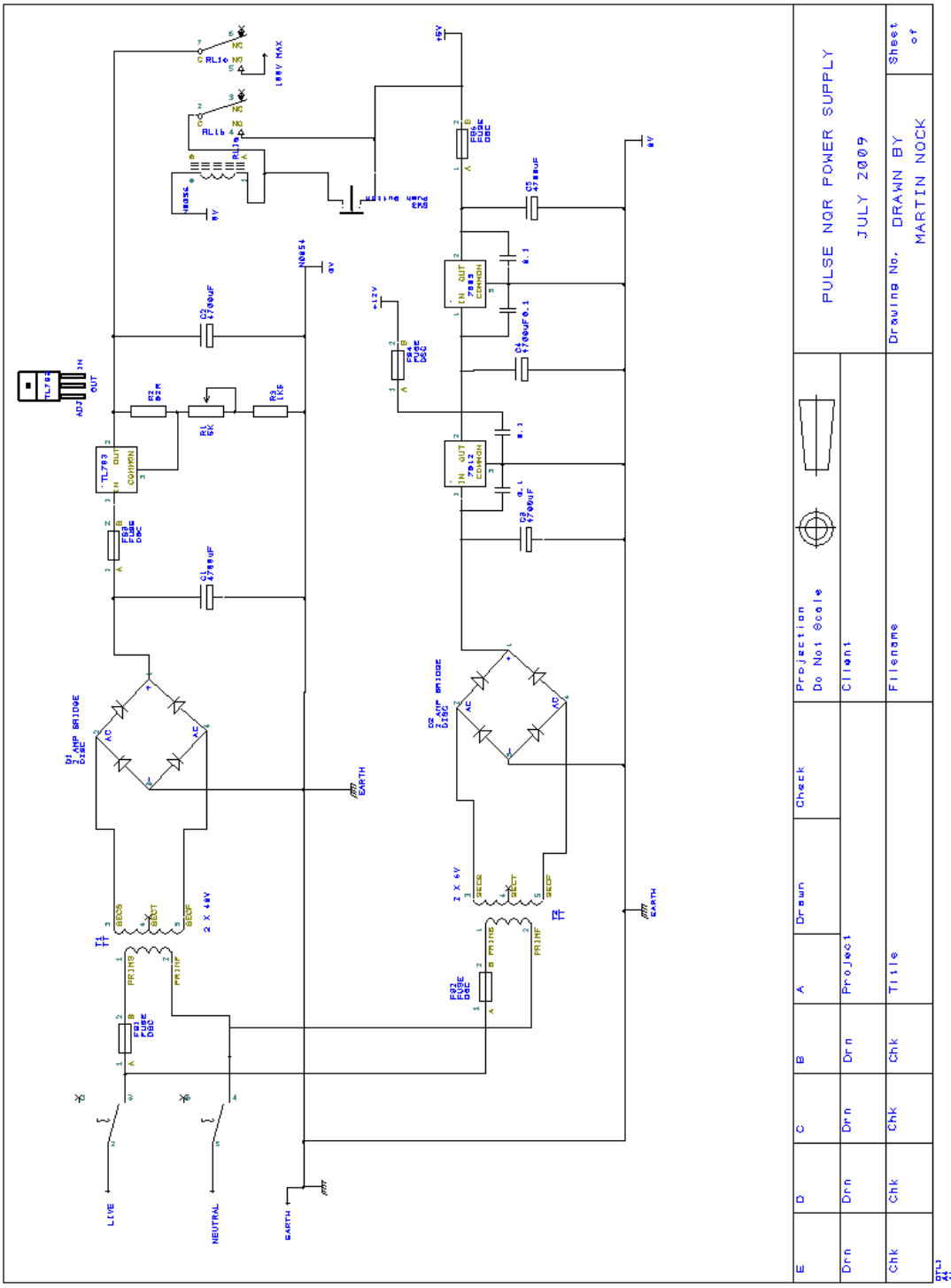

Figure C.2: The schematic diagram of the power supply. Designed and built by Martin Nock.

REFERENCES

[1] Terence, D. Clark, Robert, J. Prance, and Christopher, J. Harland, "Electrodynamic sensors and applications thereof," WO/2003/048789, June 12, 2003.

[2] C J Harland, T D Clark, and R J Prance, "Electric potential probes - new directions in the remote sensing of the human body," *Measurement Science and Technology*, vol. 13, no. 2, pp. 163-169, 2002.

[3] R J Prance et al., "An ultra-low-noise electrical-potential probe for human-body scanning," *Measurement Science and Technology*, vol. 11, no. 3, pp. 291-297, 2000.

[4] C J Harland, T D Clark, and R J Prance, "High resolution ambulatory electrocardiographic monitoring using wrist-mounted electric potential sensors," *Measurement Science and Technology*, vol. 14, no. 7, pp. 923-928, 2003.

[5] R. J. Prance, S. T. Beardsmore-Rust, P. Watson, C. J. Harland, and H. Prance, "Remote detection of human electrophysiological signals using electric potential sensors," *Applied Physics Letters*, vol. 93, no. 3, p. 033906, 2008.

[6] S. Beardsmore-Rust et al., "Detecting electric field disturbances for passive through-wall movement and proximity sensing," *Smart Biomedical and Physiological Sensor Technology VI*, vol. 7313, no. 1, p. 73130P, 2009.

[7] S T Beardsmore-Rust, P Watson, R J Prance, C J Harland, and H Prance, "Imaging of charge spatial density on insulating materials," *Measurement Science and Technology*, vol. 20, no. 9, p. 095711 (6pp), 2009.

[8] S T Beardsmore-Rust, P Watson, R J Prance, C J Harland, and H Prance, "Quantitative measurement of tribo-electric charging phenomena of dielectric materials," *Proc. ESA Annual Meeting on Electrostatics 2009*, vol. Session 5, p. 1, 2009.

[9] P. Watson, R. J. Prance, H. Prance, and S. T. Beardsmore-Rust, "Imaging the time sequence of latent electrostatic fingerprints," in *Proc. SPIE 7838; doi:10.1117/12.864446*, vol. 7838, Toulouse, France, 2010, p. 783803.

[10] Robert J. Prance , Sam T. Beardsmore-Rust, HelenPrance Philip Watson, "Imaging electrostatic fingerprints with implications for a forensic timeline," *Forensic Science International*, vol. 209, no. 1-3, pp. e41-e45, April 2011.

[11] A J Clippingdale, R J Prance, T D Clark, and F Brouers, "Non-invasive dielectric measurements with scanning potential microscope," *Journal of Physics D*, vol. 27,

pp. 2426-2430, 1994.

[12] W Gebrial, C Antrobus, and R J Prance, "Non destructive testing of materials using a novel electric potential sensor," in *Sensors Applications Symposium, 2006. Proceedings of the 2006 IEEE*, Huston, 2006, pp. 115 - 118.

[13] W Gebrial et al., "Non-contact imaging of carbon composite structures using electric potential (displacement current) sensors," *Measurement Science and Technology*, vol. 17, no. 6, pp. 1470-1476, 2006.

[14] P Stiffell, R J Prance, Gebrial W, Harland C J, and H Prance, "Defect detection using a non-contact electric potential drop method for multilayer carbon composite materials," in *Emerging Technologies in NDT conference*, Stuttgart, 2007, p. 4.

[15] W. Gebrial, R. J. Prance, C. J. Harland, and T. D. Clark, "Noninvasive imaging using an array of electric potential sensors," *Review of Scientific Instruments*, vol. 77, no. 6, p. 063708, 2006.

[16] W Gebrial, R J Prance, C J Harland, C Antrobus, and T D Clark, "The propagation delay of electrical signals in saline using electric potential sensors," *Journal of Physics D: Applied Physics*, vol. 40, no. 1, pp. 31-35, 2007.

[17] R J Prance, T D Clark, H Prance, and A Clippingdale, "Non-contact VLSI imaging using a scanning electric potential microscope," *Measurement Science and Technology*, vol. 9, no. 8, p. 1229, 1998.

[18] W. Gebrial et al., "Noninvasive imaging of signals in digital circuits," *Review of Scientific Instruments*, vol. 73, no. 3, pp. 1293-1298, 2002.

[19] R. J. Prance and A. Aydin, "Acquisition of a nuclear magnetic resonance signal using an electric field detection technique," *Applied Physics Letters*, vol. 91, no. 4, p. 044103, 2007.

[20] Robert J. Prance, Ahmet Aydin, Christopher J. Harland, and Helen Prance, "Development of Electric Field Nmr Signal Acquisition System," in *Explosives Detection Using Magnetic and Nuclear Resonance Techniques*, Jacques Fraissard and Olga Lapina, Eds.: Springer Netherlands, 2009, pp. 245-252, 10.1007/978-90-481-3062-7_15.

[21] S Mukherjee, P Watson, and R J Prance, "Microscopic resolution broadband dielectric spectroscopy," *Journal of Physics: Conference Series*, vol. 310, no. 1, p. 012003, 2011.

[22] S Mukherjee, P Watson, and R J Prance, "Non-contact measurement of local conductivity variations in carbon fibre based composite materials," *Journal of Physics: Conference Series*, vol. 307, no. 1, p. 012034, 2011.

[23] E. M. Purcell, H. C. Torrey, and R. V. Pound, "Resonance Absorption by Nuclear

Magnetic Moments in a Solid," *Phys. Rev.*, vol. 69, pp. 37-38, 1946.

[24] F. Bloch, "Nuclear Induction," *Phys. Rev.*, vol. 70, pp. 460-474, 1946.

[25] J.A.S. Smith, "Nitrogen-14 quadrupole resonance detection of RDX and HMX based explosives," in *European Convention on Security and Detection*, 1995, pp. 288-292.

[26] A.N. Garroway et al., "Remote sensing by nuclear quadrupole resonance," *Geoscience and Remote Sensing, IEEE Transactions on*, vol. 39, no. 6, pp. 1108-1118, 2001.

[27] S.D. Somasundaram, A. Jakobsson, J.A.S. Smith, and K. Althoefer, "Exploiting Spin Echo Decay in the Detection of Nuclear Quadrupole Resonance Signals," *Geoscience and Remote Sensing, IEEE Transactions on*, vol. 45, no. 4, pp. 925-933, 2007.

[28] T. N. Rudakov, V. T. Mikhaltsevitch, and J. H. Flexman, "Modified steady-state free precession pulse sequences for the detection of pure nuclear quadrupole resonance," *Solid State Nuclear Magnetic Resonance*, vol. 25, no. 1-3, pp. 94-98, 2004, 31st Congress Ampere, Magnetic Resonance and Related Phenomena.

[29] T. Rudakov, V. Mikhaltsevitch, J. Flexman, P. Hayes, and W. Chisholm, "Modified multipulse technique for the effective detection of pure nuclear quadrupole resonance," *Applied Magnetic Resonance*, vol. 25, pp. 467-474, 2004, 10.1007/BF03166541.

[30] T.N. Rudakov, P.A. Hayes, and J.H. Flexman, "Optimised NQR pulse technique for the effective detection of Heroin Base," *Solid State Nuclear Magnetic Resonance*, vol. 33, no. 3, pp. 31-35, 2008.

[31] T.N. Rudakov and P.A. Hayes, "Cross-polarisation method for improvement of 14N NQR signal detectability," *Journal of Magnetic Resonance*, vol. 183, no. 1, pp. 96-101, 2006.

[32] Alan Gregorovic et al., "Capacitor-based detection of nuclear magnetization: Nuclear quadrupole resonance of surfaces," *Journal of Magnetic Resonance*, vol. 209, no. 1, pp. 79-82, 2011.

[33] Gregory Fisher, Ernesto MacNamara, Robert E. Santini, and Daniel Raftery, "A versatile computer-controlled pulsed nuclear quadrupole resonance spectrometer," *Review of Scientific Instruments*, vol. 70, no. 12, pp. 4676-4681, 1999.

[34] Z.L. Wang and Z.C. Kang. (1998) http://www.gatech.edu/. [Online]. http://www.nanoscience.gatech.edu/zlwang/book/book3.htm

[35] R.J.Collier and A.D.Skinner, *Microwave Measurements*, 3rd ed. Stevenage, UK: The Institute of Engineering & Technology, 2007.

[36] R.G. Geyer, J. Baker-Jarvis, and J. Ceremuga J. Krupka, "Measurements of the complex permittivity of microwavecircuit board substrates using split dielectric resonator and reentrant cavity techniques," in *DMMA Conference*, Bath, U.K., 1996, pp. 21-24.

[37] Krzysztof Derzakowskiz, Bill Riddlex and James Baker-Jarvis Jerzy Krupkay, "A dielectric resonator for measurements of complex permittivity of low loss dielectric materials as a function of temperature," *Meas. Sci. Technology*, vol. 9, pp. 1751–1756, July 1998.

[38] A S Chen, D P Almond, and B Harris, "Acoustography as a means of monitoring damage in composites during static or fatigue loading," *Measurement Science and Tchnology*, vol. 12, pp. 151-156, 2000.

[39] Y. Tavrin et al., "Eddy current technique with high temperature SQUID for non-destructive evaluation of non-magnetic metallic structures," *Cryogenics*, vol. 36, no. 2, pp. 83-86, 1996. [Online]. http://www.sciencedirect.com/science/article/pii/0011227596838070

[40] P E Irving and C Thiagarajan, "Fatigue damage characterization in carbon fibre composite materials using an electrical potential technique," *Smart Mater. Struct*, vol. 7, pp. 456-466, 1998.

[41] H. Rohrer, Ch. Gerber, and E. Weibel G. Binning, "Surface Studies by Scanning Tunneling Microscopy," *Physical Review Letters*, vol. 49, no. 1, pp. 57-61, July 1982.

[42] G. Binnig and C. F. Quate AND Ch.Gerber, "Atomic Force Microscope," *Physical Review Letters*, vol. 56, no. 9, pp. 930-934, March 1986.

[43] A. Pasquini, G.B. Picotto, and M. Pisani, "STM carbon nanotube tips fabrication for critical dimension measurements," *Sensors and Actuators A: Physical*, vol. 123-124, pp. 655-659, 2005, Eurosensors XVIII 2004 - The 18th European conference on Solid-State Transducers.

[44] Nuno C. Santos and Miguel A. R., "An overview of the biophysical applications of atomic force microscopy," *Biophysical Chemistry*, vol. 107, no. 2, pp. 133-149, 2004.

[45] R. Möller, C. Baur, A. Esslinger, and P. Kürz, "Scanning noise potentiometry," *Journal of Vacuum Science & Technology B: Microelectronics and Nanometer Structures* , vol. 9, no. 2, pp. 609-611, 1991. [Online]. http://dx.doi.org/doi/10.1116/1.585468

[46] D. Hoffmann, A. Haas, T. Kunstmann, J. Seifritz, and R. Möller, "Thermovoltage in scanning tunneling microscopy," *Journal of Vacuum Science & Technology A: Vacuum, Surfaces, and Films* , vol. 15, no. 3, pp. 1418-1422, 1997. [Online]. http://dx.doi.org/doi/10.1116/1.580553

[47] J. R. Matey and J. Blanc, "Scanning capacitance microscopy," *Journal of Applied Physics*, vol. 57, no. 5, pp. 1437-1444, 1985. [Online]. http://link.aip.org/link/?JAP/57/1437/1

[48] Gabi Neubauer et al., "Two-dimensional scanning capacitance microscopy measurements of cross-sectioned very large scale integration test structures," vol. 14, no. 1, pp. 426-432, 1996. [Online]. http://dx.doi.org/doi/10.1116/1.588487

[49] A.Aydin, "Application of Electric potential sensors in nuclear magnetic resonance signal acquisition," University of Sussex, Brighton, DPhil Thesis 2006.

[50] Ramakant A. Gayakwad, *Op-Amps and linear integrated circuits*, 4th ed.: Prentice Hall, 2000.

[51] G B Clayton, *Operational Amplifiers*, 2nd ed.: Newnes-Butterworths, 1979.

[52] Jerald G. Graeme, *Applications of operational amplifiers : third-generation techniques*.: McGraw-Hill, 1973., Includes index.

[53] Alan Rich, Shielding and guarding How to exclude interference-Type Noise What to do do and why to do it- A rational approach Analog Devices application note AN-347, Analog devices, One technology way, P.O.Box 9106, Norwood, Massachusetts 02062-9106, Tel- 617/329-4700, 1983.

[54] Texas Instruments OPA, OPA 656 Wideband, unity-gain stable, FET input Operational amplifier,Texas Instruments, Post Office Box 655303, Dallas, Texas 75265, 2008.

[55] Electronic Workbench. [Online]. http://www.electronicsworkbench.com/

[56] Number One Systems, Easy PC, Number One Systems, Oak Lane, Bredon, Tewkesbury, Glos. GL20 7LR, UK. web:http://www.numberone.com/easypc.asp, 2011.

[57] Perancea ltd. products and services,36, Silicon business centre,28 Wadsworth road,Piervale,Greenford, UB6 7JZ, England,tel:+44 20 8365 2520,http://perancea.com/prod-metal03.htm, CFL series: Can and fingered Lid.

[58] BI Technologies Corporation, Application note- Trimming potentiometers, 4200 Bonita Place Fullerton, CA 92835-1053.

[59] Properties of Low Dielectric Constant Laminates, 2010.

[60] Rhode & Schwarz, GmbH & Co.KG,Mühldorfstraße 1581671 Munich, Germany,Tel: 089 4129-0, Spectrum analyzer FSEA 30, Operating maual 1065.6061.12-13, , 2000.

[61] Texas Instruments, OPA847 -Wideband, Ultra-Low Noise, Voltage-Feedback OPERATIONAL AMPLIFIER with Shutdown Texas Instruments, Post Office Box

655303, Dallas, Texas 75265, 2008.

[62] Pulse multi-analyzer system Type 3560 B/C/D/E, B &K , DK-2850 NÊrum · Denmark · Telephone: +45 4580 0500, www.bksv.com, 2009.

[63] Henry W. Ott, *Noise reduction techniques in electronic systems*, 2nd ed.: Wiley Interscience, 1988.

[64] J. A.S Smith, "Nuclear quadrupole resonance spectroscopy. General principles," *Journal of Chemical Education*, vol. 48, no. 1, p. 39, 1971.

[65] C.P.Slichter, *Principles of magnetic resonance*.: Springer-Verlag, 1989.

[66] M.H.Levitt, *Spin Dynamics- basics of nuclear magnetic resonance*.: Wiley, 2008.

[67] O.S.Sotican, NQR detection setup, 2004, INFLPR Bucharest, ostoican@k.ro Paper presented at the 5th international Balkan workshop on Applied Physics. 5-7 July 2004,Constanta, Romania.

[68] Yasuhide Kikuchi Ryokan, "Construction of Apparatus for NQR Experiment," *Bull College of Science, University of the Ryukyus*, vol. 36, pp. 27-51, 1983.

[69] Suresh K. S. and J. Ramakrishna, "Pressure and temperature dependence of the chlorine NQR in caesium and sodium chlorates. Magnetic Resonance in Chemistry," vol. 46, 2008.

[70] Sigma-Aldrich Company Ltd.,The Old Brickyard,New Road,Gillingham,Dorset,SP8 4XT,Freephone: 0800 717181,.

[71] Reagents. (2010) [Online]. http://www.reagents.com/products/reagents/grades.html

[72] Philips semiconductor,NXP Semiconductors,Millbrook Technology Campus,Southampton, SO15 0DJ,Tel:+44 (0) 161 408 0792, BB809 VHF variable capacitance diode, May 3, 1996.

[73] R J Offen and N R Thomson, "A simple marginal oscillator suitable for undergraduate NMR experiments," 1969.

[74] John D. Idoine and J. R. Brandenberger, "FET Marginal Oscillator Circuit," vol. 42, no. 5, pp. 715-717, 1971.

[75] LD Didactic GmbH,Leyboldstrasse, 1D-50354 Hürth, Telefon: (02233) 604-0, Fax: (02233) 604-222 ,email:info@ld-didactic.de, NMR supply unit part number: 514 602.

[76] Micro-coax Inc.,206 Jones Blvd. Pottstown, PA 19464 USA,Phone: 610-495-0110 : 800-223-2629,www.micro-coax.com , UT-034 semi rigid cable.

[77] Philips Semiconductors,811 East Arques Avenue,P.O. Box 3409,Sunnyvale, California 94088–3409,Telephone 800-234-7381, SA602A Double-balanced mixer and oscillator, April 17, 1990.

[78] Rohde&Schwarz GmbH& Co. KG,81671 München, Germany,Tel: +49 89 4129 123 45,Web: http://www.rohde-schwarz.co.uk, R&S®SMB100A Signal Generator Specifications, November 2010.

[79] National Instruments Corporation (U.K.) Ltd.,Measurement House, Newbury Business Park,London Road,Newbury, Berkshire RG14 2PS,Tel: 01635 523545, Bus-Powered USB Digitizers NI USB-5132, NI USB-5133, 2010.

[80] Jordan Kirsch and Robert Newman. (2005) http://web.mit.edu/8.13/www/12.shtml.

[81] National Semiconductors, LM555 Timer datasheet, National Semiconductors, 2900 Semiconductor Dr., Santa Clara, CA 95051,USA, Tel: (408) 721-5000, 2006.

[82] Philips Semiconductors, 74F06, 74F06A, 74F07, 74F07A Inverter/buffer drivers, Philips Semiconductors, 811 East Arques Avenue, P.O. Box 3409 Sunnyvale, California 94088–3409, Telephone 800-234-7381, 1992.

[83] Texas Instruments, CD4071B, CD4072B, CD4075B TYPES (Rev. D) datasheet, Texas Instruments, Incorporated,Texas Instruments, Post Office Box 655303, Dallas, Texas 75265,USA, 2003.

[84] Vishay Electronic GmbH, IRF 830/ SiHF 830 datasheet, Vishay Electronic GmbH, Geheimrat-Rosenthal-Str. 100 Selb D-95100 ,Germany, Phone: 49-9287-71-0 Fax: 49-9287-70435, 2011.

[85] I J Lowe and C E Tarr, "A fast recovery probe and receiver for pulsed nuclear magnetic resonance spectroscopy," *Journal of Physics E: Scientific Instruments*, vol. 1, no. 3, p. 320, 1968.

[86] D D Griffin, R L Kleinberg, and M Fukuhara, "Low-frequency NMR spectrometer," *Measurement Science and Technology*, vol. 4, no. 9, p. 968, 1993.

[87] Thurlby Thandar Instruments Ltd. , TGR1040 1 GHz Synthesised RF Signal Generator,Thurlby Thandar Instruments Ltd. ,Glebe Road, Huntingdon, Cambridgeshire PE29 7DR England (United Kingdom) ,Telephone: +44 1480 412451 , Fax: +44 1480 450409, Issue 7.

[88] Ohio Microwave LLC, High-Level Double-Balanced Mixer 5-4000 MHz, Ohio Microwave LLC,848-A E. Franklin St.,Dayton, OH, USA 45459,Phone 937-434-5078,Fax 937-434-5079.

[89] Sam Thomas Beardsmore-Rust, "Remote applications of electric potential sensors in electrically unshielded environments," Engineering & Design, University of Sussex, Brighton, DPhil thesis 2010.

[90] Klapetek, Petr,Czech Metrology Institute,Okružní 31, 638 00, Brno,Czech Republic,klapetek@gwyddion.net, gwyddion , 2011, http://gwyddion.net/.

[91] Stephen Mumby and Jih Yuan, "Dielectric properties of FR-4 laminates as a function of thickness and the electrical frequency of the measurement," *Journal of Electronic Materials*, vol. 18, pp. 287-292, 1989, 10.1007/BF02657420.

[92] Wifgi Rafig Wifgi, "Non-invasive circuit and material imaging using the electric potential sensor," School of Engineering & Design, DPhil thesis 2002.

[93] Reinhold Ludwig and Pavel Bretchko, *RF Circuit Design: Theory & Applications*, Marcia Horton, Ed. NJ, USA: Prentice Hall, 2000.

[94] John D Kraus and Daniel A Fleich, *Electrmagnetics with Applications*, 5th ed. Singapore, Singapore: Mc Graw Hills, 1999.

[95] Agilent Technologies, 4275A Multi-Frequency LCR Meter, 1990, (Former HP product taken over by Agilent),Agilent Technologies,5301 Stevens Creek Blvd,Santa Clara CA 95051, USA,Tel:+1 800 829-4444.

[96] Fujitsu Microelectronics Inc., MBF 200 Solid state fingerprint sensor datasheet, Fujitsu Microelectronics America Inc., Corporate Headquarters,1250 E. Arques Ave. Sunnyvale, CA 94088-3470,Tel: (800) 866-8608 Fax: (408) 737-5999,E-mail: inquiry@fma.fujitsu.com Web Site: http://www.fma.f, 2008.